Author:
Cen, Hanyu

Title:
Solar Thermal Characterisation of Micro-Patterned High Temperature Selective Surfaces applied to a Thermionic Device

University of BRISTOL

Solar Thermal Characterisation of Micro-Patterned High Temperature Selective Surfaces applied to a Thermionic Device

Hanyu Cen

Department of Electrical and Electronic Engineering

A dissertation submitted to the University of Bristol in accordance with the requirements for award of the degree of Doctor of Philosophy in the Faculty of Engineering

March 2020

DECLARATION

I declare that the work in this dissertation was carried out in accordance with the requirements of the University's Regulations and Code of Practice for Research Degree Programmes and that it has not been submitted for any other academic award. Except where indicated by specific reference in the text, the work is the candidate's own work. Work done in collaboration with, or with the assistance of, others, is indicated as such. Any views expressed in the dissertation are those of the author.

Signed:_____

Date:_____

ABSTRACT

Solar thermal energy converters have been widely studied for many years and are suitable for both small and large-scale deployment. Solar thermionic energy converters are a much more direct and potentially more efficient way of generating electricity from solar energy. An ideal absorber aims to maximise solar absorption while minimising infra-red emissivity in order to achieve the highest possible temperature. Preventing conduction and convection heat loss of the solar absorber is also a key to obtain a higher temperature.

In this thesis, molybdenum samples were fabricated using laser micromachining. Finite Difference Time Domain modelling of the microstructure has shown the absorptivity increased over the visible and near-infrared region. The microstructures were characterised using an integrating sphere and an infrared microscope.

In-air solar simulator-heated temperature results for the molybdenum samples with different microstructures showed good agreement with the absorptivity measurements. Two vacuum devices were developed to reduce the convection heat loss with a mount designed to minimise conduction loss. The molybdenum samples were heated in the vacuum devices with a solar simulator and focused sunlight and >400°C has been achieved.

COMSOL Multiphysics has been used to model the heat transfer between the

molybdenum sample and the holder. Based on the simulation results, a prototype of fully sealed thermionic emission convertor was proposed which has a new design of the sample and the holder. Overall, this work shows that low-cost laser micro-patterned molybdenum samples have good potential to obtain high temperature for thermionic emission applications.

ACKNOWLEGEMENT

First of all, I would like to thank my supervisor Professor Martin Cryan for his guidance and support for this work. I have learnt so much from him and I can only express my deepest respect and gratitude towards him. I would like to thank Professor Ruth Oulton for her guidance over my annual reviews.

I am also thankful to Dr. Neil fox, Dr. James Smith, Ian Bickerton and Dr. Andrei Sarua whose support and feedback has been extremely helpful for this work.

A special thanks to John Rowden, for helping me build the vacuum device. This work could not be done without his patience with numerous times of pumping the device.

I would like to express my gratitude and appreciation for my colleagues in the Photonics and Quantum Group members: Jon Pugh, Sara Nunez-Sanchez, Nathan Ahmad, Neciah Dorh, Simeng Jia and Weiran Pang.

From the bottom of my heart I would like to say thank you to my parents. They have been very supportive throughout my PhD time and their love have played a tremendous role in the creation of this work.

CONTENTS

1. Introduction 1

1.1. Motivation 1

1.2. Solar Energy Conversion 2

1.2.1. Photovoltaics 4

1.2.2. Solar Thermal Technology 5

1.2.3. Thermoelectrics 7

1.2.4. Thermophotovoltaics 10

1.2.5. Thermionic Emission 11

1.3. Outline of Thesis 13

1.4. Contributions 14

2. Theory of Heat Transfer and Selective Absorbers 16

2.1. Laws of Thermodynamics 16

2.2. Carnot's theorem 18

2.3. Conduction 19

2.4. Convection 21

2.5. Radiation 23

2.5.1. Blackbody Radiation 25

2.5.2. Kirchhoff's Law 28

2.5.3. Selective Surfaces 30

2.6. Current selective surfaces 32

2.6.1. Intrinsic absorbers 32

2.6.2. Semiconductor-metal tandems....33
2.6.3. Multilayer absorbers....34
2.6.4. Cermets....35
2.6.5. Surface texturing....35
2.7. Chapter Conclusion....36
3. Computational Methods....38
3.1. Simulation methods for heat transfer....38
3.1.1. The Finite Element Method....39
3.1.2. Numerical Approximation....40
3.1.3. Discretisation....40
3.1.4. An example of heat transfer simulation with COMSOL Multiphysics....41
3.2. Simulation methods for micro-patterned structures....45
3.2.1. The Finite-difference time-domain method....45
3.2.2. An example of Lumerical FDTD simulation....49
3.3. Chapter Conclusion....52
4. Fabrication and Characterisation....54
4.1. Laser Etching....54
4.2. Fabrication of 2D Micro-patterned Molybdenum using Laser Etching Technique....57
4.3. Optical Simulation....59
4.4. Optical Characterisation of Microstructures....62
4.4.1. Integrating Sphere....62

4.4.2. Reflectance Measurements 64
4.4.3. Emissivity Measurements 67
4.5. Chapter Conclusion 69
5. In air and vacuum light heating experiment 70
5.1. 2D Patterned Molybdenum in-air heating measurements.....71
5.2. 2D Patterned Molybdenum in-vacuum results in India 75
5.2.1. Solar heating measurements using a dual axis solar tracker with Fresnel lens 79
5.2.2. Solar heating measurements using a parabola dish 81
5.3. 2D Patterned Molybdenum in-vacuum results using solar simulator 84
5.4. Chapter Conclusion 92
6. Thermal Optimisation and Thermionic Device Prototype.....94
6.1. COMSOL Multiphysics Thermal Modelling 95
6.1.1. Modelling Methodology 95
6.1.2. Modelling Results 98
6.2. Thermionic Convertor Prototype 102
6.3. Chapter Conclusion 107
7. Conclusion and Future Works 108
7.1. Conclusion.....108
7.2. Future Works.....110

8. References.....112

9. Appendix.....123

9.1. Power output of the solar simulator 123

9.2. Calculating natural convection coefficient 125

LIST OF TABLES

Table 1.1 Characteristics of concentrating solar power technologies [19-22] 7

Table 3.1 The sampling positions for each component in the Yee's cell..49

Table 4.1 Laser pulse period and laser energy used for 9 molybdenum samples.....58

Table 5.1 Parameters used in COMSOL Multiphysics simulation.....89

Table 6.1 Swept parameters in the modelling.....97

LIST OF FIGURES

Figure 1.1 Shares of global energy consumption from 1985-2018 [1]. 2

Figure 1.2 Solar irradiation spectrum above the atmosphere and at sea-level [5]. 3

Figure 1.3 Typical PN junction Photovoltaic Cell [13] 5

Figure 1.4 Thermophotovoltaic system 10

Figure 1.5 Schematic diagram of the electron thermionic emission process [29]. 11

Figure 2.1 Solar to thermal, thermal to work and solar to work efficiencies in a solar thermal system [42]. 19

Figure 2.2 One-dimensional heat transfer through a solid 20

Figure 2.3 Heat transfer between two solids in contact.....21

Figure 2.4 Electromagnetic spectrum 24

Figure 2.5 Blackbody spectral radiance at different temperatures [55] ...27

Figure 2.6 Blackbody spectral radiance at 5500 K (orange) and 1000 K (blue), the scale of the spectral radiance of 5500 K is on the left axis and the scale of the spectral radiance of 1000 K is on the right axis [55] 31

Figure 2.7 Schematic design of solar selective absorbers, (a) Intrinsic absorbers, (b) Semiconductor-metal tandems, (c) Multilayer absorbers, (d) Cermets (metal-dielectric composites), and (e) Surface texturing

[59] 32

Figure 3.1. Geometry and node placement for 1D, 2D and 3D linear elements. [104].....41

Figure 3.2 A metal disc sits on a quartz disc. The top surface of the metal disc is heated with a 10 W heat source in air. 42

Figure 3.3 Simulation results: (a) Mesh of the geometry; (b) Temperature distribution of the system.....43

Figure 3.4 Temperature of the metal disc as functions of time 43

Figure 3.5 Temperature of the metal disc as functions of time when the convective heat transfer coefficient is 0 and 20 W/(m^2·K) and the thermal contact conductivity is 10 and 1000 W/(m^2·K). 44

Figure 3.6 The Anatomy of the Yee cell 48

Figure 3.7 XY view of simulated 2.5 μm thick flat Molybdenum 50

Figure 3.8 2D and 3D views of Lumerical FDTD simulation of bulk molybdenum, (1). XY view; (2). 3D view; (3). XZ view; (4). YZ view 51

Figure 3.9 Left axis: Theoretical and simulated reflectivity of molybdenum in the wavelength range of 0.3 to 5.0 μm; Right axis: Values of the real (n) and imaginary part (k) of the refractive index of molybdenum...52

Figure 4.1 Schematics of laser micromachining, (a) direct laser writing; (b) mask projection technique [119].....56

Figure 4.2 SEM image of a laser patterned molybdenum sample produced

at 20% laser power and 30μm period 58

Figure 4.3 Optical microscope images of the laser micro-patterned molybdenum surfaces at: a) 28.6 μJ/pulse and b) 48.1 μJ/pulse with a laser firing distance of 10μm, c) 38.3 μJ/pulse and d) 48.1 μJ/pulse with a laser firing distance of 30 μm 59

Figure 4.4 Simulated molybdenum periodic structure with trapezoidal holes 60

Figure 4.5 Absorptivity obtained from simulations of a flat molybdenum and a periodic and non-periodic molybdenum structure with large trapezoidal holes, where L_{top}=20 μm, L_{bottom}=5 μm and D=10 μm. ..60

Figure 4.6 (a) Simulated absorptivity of molybdenum periodic structures with 3 different sized holes and a flat molybdenum; (b) Electric field distribution inside the large hole (L_{top}=20 μm, L_{bottom}=5 μm and D=10 μm) at 500 nm wavelength; (c) Electric field distribution inside the medium hole (L_{top}=15 μm, L_{bottom}=3.75 μm and D=7.5 μm) at 500 nm wavelength; (d) Electric field distribution inside the small hole (L_{top}=10 μm, L_{bottom}=2.5 μm and D=5 μm) at 500 nm wavelength; ..61

Figure 4.7 Schematic diagram of integrating sphere 63

Figure 4.8 An integrating sphere and a spectrometer setup for measuring the reflectance of the samples 64

Figure 4.9 Reflectance measurements with the integrating sphere. (a)-(c): Reflectance of the samples dependence on period. (d)-(f): Reflectance of the samples dependence on laser energy. 66

Figure 4.10 Absorptivity at 500 nm (wavelength at maximum of solar spectrum) for all samples as a function of the pulse energy and the average periods. 67

Figure 4.11 Emissivity measurement setup including an IR microscope and a Peltier heater.....68

Figure 4.12 Emissivity measurement results for both sides of 3 molybdenum samples at 75℃ 69

Figure 5.1 Schematic diagram of general light heating experiment.....70

Figure 5.2 Measurement setup for molybdenum samples in air thermal test, (a) a picture of the setup; (b) schematic diagram shows how sample is mounted on the glasses; (c) top view schematic diagram 73

Figure 5.3 The highest temperatures achieved of ten samples over 500s solar simulator illumination. Triangles, circles and squares represent 30μm,20μm and 10μm average period of the sample microstructure; x-axis represents the laser energies used to produce the samples 75

Figure 5.4 Vacuum device for temperature experiment 76

Figure 5.5 The internal design of the vacuum device, the inserted picture shows the quartz holder 77

Figure 5.6 (a) Vacuum device in air measurement setup; (b) Measured temperature rises of the molybdenum sample 9 and the sample holder over 500s illumination 78

Figure 5.7 The vacuum device pumped to vacuum while heating up to 200℃ in an oven.....79

Figure 5.8 vacuum device solar heating measurement on a dual axis solar tracker.....80

Figure 5.9 Measured temperature response of sample 9 and the holder with DNI in 2 hours and 46 minutes.....81

Figure 5.10 vacuum device mounted on a parabola dish 82

Figure 5.11 Measured temperature response of the sample and the holder in 42 minutes.....83

Figure 5.12 vacuum device with a glass dome, (a) front side; (b) inside; (c) back side; (d) quartz holder and sample 85

Figure 5.13 (a) Simulated top view of the proposed sample mounting mechanism with Molybdenum sample, (b) Gaussian profile heat source applied on top of the sample.....86

Figure 5.14 Simulated cross section diagram of the proposed sample mounting mechanism with patterned surface on top 87

Figure 5.15 Illustrations of three cases for the temperature measurements: (a) flat-flat, (b) patterned-flat and (c) flat-patterned.....88

Figure 5.16 COMSOL simulation of the effects on the highest achieved temperatures by varying the thermal contact conductance between the molybdenum sample and the quartz holder 90

Figure 5.17 COMSOL simulated (thermal contact conductance=700 $W/(m^2 \cdot K)$ and measured highest achieved temperature of patterned-flat, flat-flat, flat-patterned cases in air and vacuum (0.15 Torr).....91

Figure 5.18 COMSOL simulated (thermal contact conductance=700 $W/(m^2 \cdot K)$ for 0.15 Torr and 50 $W/(m^2 \cdot K)$ for 0.005 Torr) and measured highest achieved temperature of flat-patterned case in vacuum of 0.15 Torr and 0.005 Torr 92

Figure 6.1 Simulated diagram of the sample mounting mechanism and Molybdenum sample with arms, (a) top view; (b) cross section.....96

Figure 6.2 Simulated highest sample temperatures achieved after 1000s heating by varying nine parameters in the model, (i) sample radius; (ii)

sample thickness; (iii) thermal contact conductance; (iv) length of the sample arm; (v) convective heat transfer coefficient; (vi) absorptivity of the sample top surface; (vii) emissivity of the sample top surface; (viii) input light power; (ix) light spot radius. 101

Figure 6.3 Thermionic convertor design, (a) top quartz holder; (b) bottom quartz holder; (c) assembly with molybdenum emitter and collector 102

Figure 6.4 schematic of proposed thermionic convertor design (a) top view; (b) cross section view.....103

Figure 6.5 Simulated equilibrium emitter and collector temperatures achieved after 1000s heating on the emitter with different gap 104

Figure 6.6 (a) star shape flat molybdenum tested in vacuum device; (b) measured temperature response of the flat molybdenum after 500s solar simulator heating in air and in vacuum. Red dotted line shows the simulated temperature rise of the flat molybdenum after 500s solar simulator heating in vacuum. 105

Figure 6.7 Integrated thermionic convertor 106

Figure 9.1 Spectral irradiance of Newport 6255 Arc Lamp 123

PUBLICATIONS AND CONFERENCES

Publications

H. Cen, S. Nunez-Sanchez, A. Sarua, I. Bickerton, N. A. Fox, and M. J. Cryan, "Solar thermal characterization of micropatterned high temperature selective surfaces," Journal of Photonics for Energy, vol. 10, no. 2, p. 024503, 2020.

Conferences

H. Cen, N. Ahmad, S. Nunez-Sanchez, A. Reip, P.J. Dobson, I.Bickerton, N.A. Fox and M.J.Cryan, “Solar Thermal Characterisation of Micro And Nano-Patterned Solar Absorbers”, published at SIOE’16: Semiconductor and Integrated Opto-Electronics Conference 2016, Cardiff, Wales, UK, 2016. Poster.

H. Cen, N. Ahmad, S. Nunez-Sanchez, A. Reip, P.J. Dobson, I.Bickerton, N.A. Fox and M.J.Cryan, “Solar Thermal Characterisation of Micro And Nano-Patterned Solar Absorbers”, published at PECX-XII: The 12th International Symposium on Photonic and Electromagnetic Crycal structures, York, UK, 2016. Poster

H. Cen, N. Ahmad, S. Nunez-Sanchez, I.Bickerton, N.A. Fox and M.J.Cryan, “Solar Thermal Characterisation of Micro And Nano-Patterned Solar Absorbers”, published at NanoMeta2017: The 6th International Topical Meeting on Nanophotonics and Metamaterials, Seefeld(Tirol), Austria, 2017. Poster.

H. Cen, S. Nunez-Sanchez, N.A. Fox and M.J.Cryan, “Solar Thermal Characterisation of Micro-Patterned Solar Absorbers”, published at META 2019: The 10th International Conference on Metamaterials, Photonic Crystals and Plasmonics, Lisbon, Portugal, 2019. Poster

1. Introduction

1.1. Motivation

Renewable energy is one of the most important technical areas in the world economic development in the 21st century. With the rapid growth of the world economy, the demand for energy has increased drastically. In addition, the increasing depletion of fossil fuels leads to an energy bottleneck in the economic development of various countries. At the same time, the burning of fossil fuels causes rise of carbon dioxide in the atmosphere, which results the deterioration of the ecological environment and the global warming. With the increasing depletion of fossil fuels and emphasis on the environment protection, the issue of looking for clean and renewable alternative energy is becoming urgent. Figure 1.1 shows the shares of global energy consumption from 1985-2018 [1]. From the graph we can see that fossil fuels (oil, coal and natural gas) have been dominating global energy consumption over the past decades and renewables only contributed 4% in 2018 despite its strong growth in recent years.

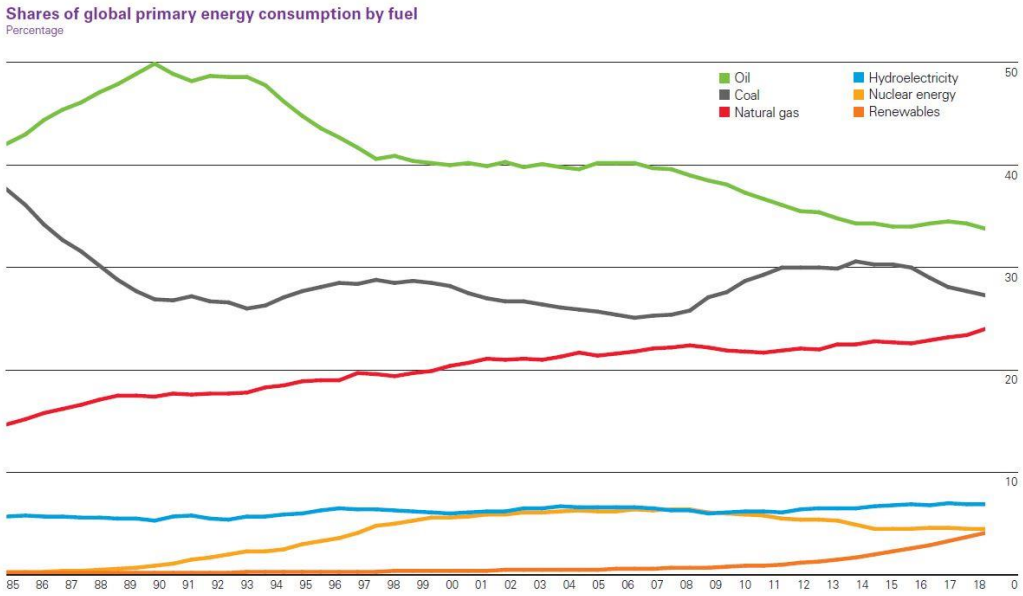

Figure 1.1 Shares of global energy consumption from 1985-2018 [1].

1.2. Solar Energy Conversion

Solar energy is a renewable clean energy, and is drawing more and more people's attention. In order to popularise these technologies, further improving efficiency and reducing costs are the main challenges for engineers and scientists. Improving the utilisation of solar energy is the key.

Most of the energy that supports mankind comes directly or indirectly from the sun. Solar energy is converted into chemical energy through photosynthesis and is stored in plants. Crude oil, coal, natural gas and other fossil fuels are formed from ancient plants and animals underground over hundreds of millions of years. In addition, hydro, wind, wave and ocean current energy are also from solar energy conversion [2].

The sun is an enormous and endless energy resource. The amount of energy that the Earth receives from the sun is 174 PW [3], which equals to the power generating from about 5 million tons of coals. Approximately 23% is absorbed by the atmosphere, 30% is reflected into space and the rest, 47% is received by the Earth surface [4]. Figure 1.2 shows the solar irradiation spectrum above the atmosphere and at sea-level.

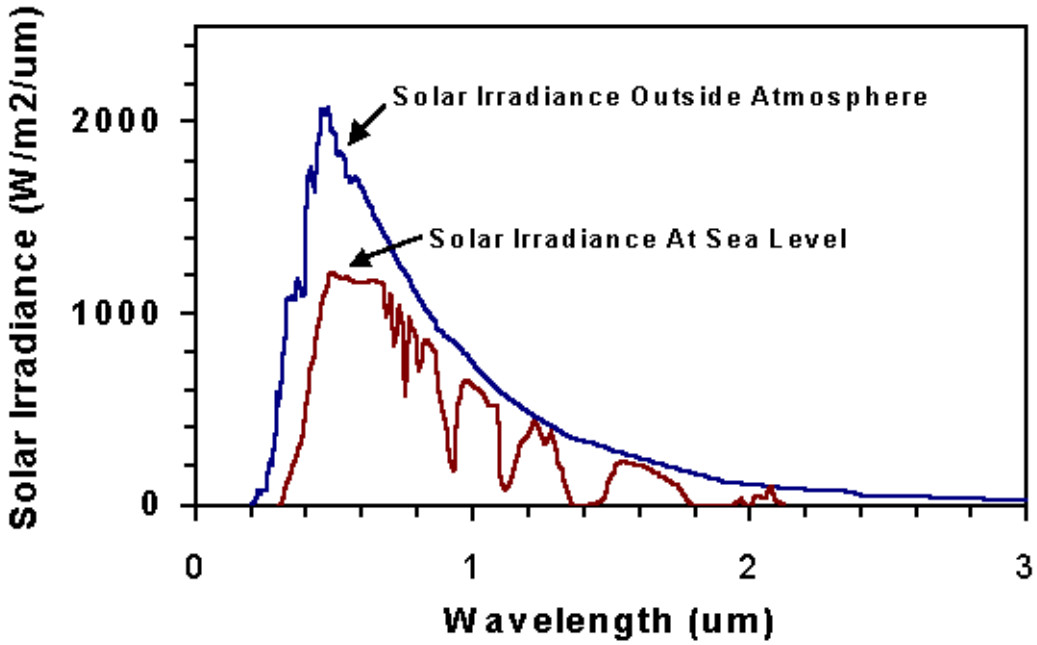

Figure 1.2 Solar irradiation spectrum above the atmosphere and at sea-level [5].

The distribution of solar irradiation spectrum is similar to a blackbody with temperature of 5777 K [6]. The energy from the sun received on a unit area outside the atmosphere is roughly 1367 W/m^2 [3, 7, 8], this data is also called the solar constant. After passing through the atmosphere, the irradiance at the Earth's surface is approximately 1000 W/m^2 [9]. In addition, most part of the solar radiation lies in the 300 to 2000 nm wavelength region.

Solar energy conversion technology can be divided into two main categories: solar photovoltaics or solar thermal technologies. Both methods absorb sun light directly or indirectly using various solar panels which combine different systems to generate electricity. An introduction of the technologies along with comparisons will be presented in this section.

1.2.1. Photovoltaics

Photovoltaics uses semiconductor electronic devices to absorb solar radiation effectively, and transforms directly into electrical power. It is today's mainstream of solar power generation. Currently, the most widely used solar cells are single crystal silicon, polycrystalline silicon and thin film solar cells. In 1839, French physicist Edmond Becquerel discovered that platinum electrodes coated with silver chloride having a voltage at both ends, produce a current under light illumination, which is known as the photovoltaic effect [10]. In 1954, Bell Labs developed monocrystalline silicon solar cells with 6% efficiency which was the beginning of the silicon solar cells era [11, 12]. A solar cell is essential a PN junction with a large surface area. As shown in Figure 1.3, the photovoltaic cell includes N-type material and P-type material. A depletion zone is between these two materials. When a photon is absorbed by the N-type material, an electron and a hole are created in the depletion zone. By connecting the N-type material and P-type material with an electric wire, the electron flow through the wire from the front electrical contact to the back electrical contact. On the other

hand, the hole travels to the P-type material and combines with the electron at the back electrical contact.

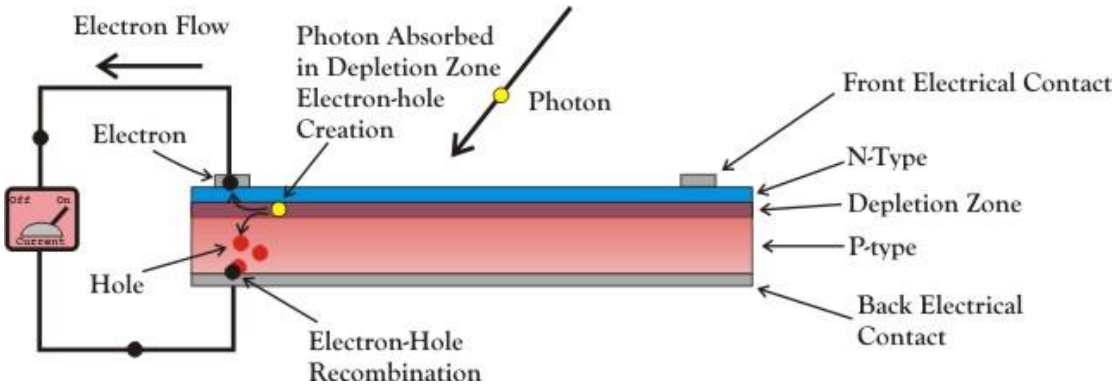

Figure 1.3 Typical PN junction Photovoltaic Cell [13]

The main limitation of photovoltaics is that only photons with energies higher than 1.1eV can be utilised in silicon base solar cell [14]. This results a maximum theoretical efficiency of 33% because 23% of the solar energy is wasted below 1.1eV [15]. Therefore, researchers are encouraged to explore other approaches such as solar thermal technologies.

1.2.2. Solar Thermal Technology

The principle of Solar thermal technology is to collect solar radiation and convert into heat, then using the thermal energy to generate electricity. Unlike photovoltaics, solar thermal technology requires high temperatures to operate. Currently, the most used solar thermal energy collection device are flat-plate collectors, vacuum tube collectors and concentrated solar power collectors [16]. Usually, depending on the temperature

can be achieved and usage, the solar thermal utilisation divides into low temperature collectors (<200℃), medium temperature collectors (200–800℃) and high temperature collectors (>800℃) [17]. Systems for utilising low temperature include solar water heaters, solar house heating and solar air conditioning, etc. Systems for medium temperature collectors include solar cooking, solar drying and solar distillation, etc. High temperature collectors are generally used in industrial power plants.

During the day the sun has different positions. For low temperature collectors, sun tracking can be avoided because the light is not focused. On the other hand, for high temperature collectors, this is unavoidable since the sun light concentration is needed. There are three main solar concentrating technologies depending on how they concentrate the light and track the sun [18].

- Parabolic dish designs

  The most efficient heat engine for the dish design solar thermal power system is Stirling engine. Under high-scale production in the hot regions, it is predicted to be able to produce the cheapest energy within all renewable energies. The main part of the dish solar thermal system includes a large, reflective, parabolic dish and an energy converter. The solar dish collecting energy from the sun and focus onto a very small area. This dish-like structure can track the sun continuously.

- Power tower designs

  This design uses a whole array of solar tracking mirrors to concentrate sunlight to

a central receiver which is mounted on a tower. Heat transfer fluid inside the receiver can be used to generate steam to drive turbines to generate electricity.

- Parabolic trough designs

  Parabolic trough design uses a curved mirror to reflect the sunlight to the fluid in the tube. The trough changes its direction based on the daily position of the sun.

Table 1.1 lists the main characteristics of these three concentrating solar power technologies.

Table 1.1 Characteristics of concentrating solar power technologies [19-22]

	Parabolic dish	Power tower	Parabolic trough
Concentration ratio	1000-3000	300-1000	25-100
Solar-to-electric efficiency	20-35%	20-35%	15%
Operating temperature	800 °C	250–650 °C	290–550 °C

1.2.3. Thermoelectrics

When electrons in a heated object move from a high temperature region to a low temperature region, a current is generated. This is called the thermoelectric effect. The

temperature difference is converted into electric voltage directly and vice versa. The thermoelectric effect includes three fundamental principles: The Seebeck effect, Peltier effect, and Thomson effect [23].

In a circuit consisting of two different metals, if the temperature at the junction of the two metals is different, the circuit will generate a thermoelectromotive force. This is the Seebeck effect [24]. Different metallic conductor or semiconductor has a different density of free electrons. When two dissimilar metal conductors are in contact with each other, the electrons in the contact surface diffuse to eliminate differences in the electron density. The rate of diffusion of electrons is proportional to the temperature difference. Therefore, electrons can be continued to spread, and form a stable voltage due to the temperature difference between two metals. The resulting voltage per Kelvin temperature difference is usually only a few microvolts. Thermocouple is a widely used application based on the Seebeck effect. It is made from two metals to measure the temperature.

When a circuit consists of two different materials, cooling or heating emerges at the contact point depending on the current direction. This effect is called Peltier effect. Peltier effect uses electromotive force to obtain current and provides cooling to one contact point and provides heating to another one. The Peltier effect can be considered as the counter effect of the Seebeck effect.

The Thomson effect was observed by William Thomson in 1851 [25]. When the

temperature is uneven inside the metal, the free electrons in the high temperature region have more kinetic energy than the ones in the low temperature region. Like in gas, a thermal diffusion occurs when the temperature is uneven. The free electrons from high temperature region diffuse to the low temperature region, thereby forming an electric field in the conductor which produces a potential difference. This diffusion of free electrons continues until the thermal diffusion is balanced.

Based on the thermoelectric effect, heat can be directly converted into electricity through solid-state devices without moving parts. However, the challenge to the technology is its relative high cost and low efficiency. It is uncommon for a material which conducts electricity well but conducts heat poorly. The goal for the researchers is to discover such material.

1.2.4. Thermophotovoltaics

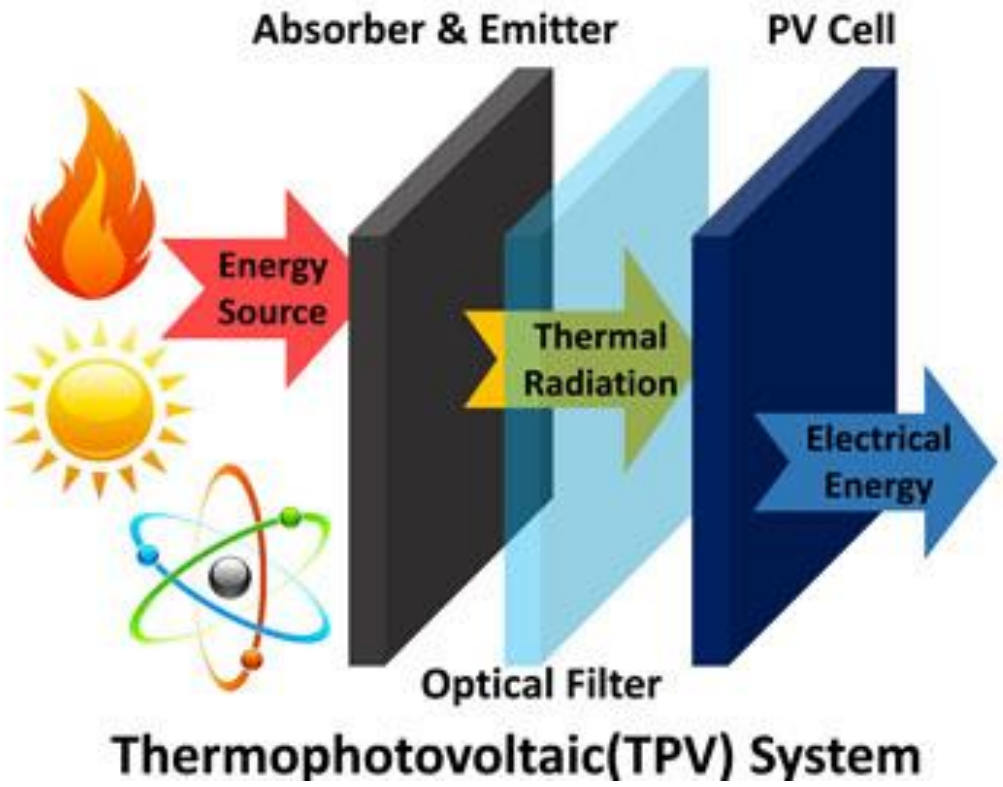

Figure 1.4 Thermophotovoltaic system

Figure 1.4 shows the principle of a thermophotovoltaic system. Thermophotovoltaic is a direct conversion of the radiation energy from a hot radiator to electricity using a semiconductor p-n junction. It uses the semiconductor p-n junction in the near-infrared light to produce photovoltaic effect [26]. The basic principle is similar to normal photovoltaic solar cells, but utilises different frequencies of radiation. Photovoltaic cells use sunlight or visible light, whereas thermophotovoltaic cells use infrared and near infrared frequencies. The structure of thermophotovoltaic cells is similar to photovoltaic cells, consists of the p-n junction, etc, which is used to absorb optical

energy, generate electron pairs and convert the energy into electricity. Thermophotovoltaic cells, compared to thermomechanical generators, have advantages of quiet, portable, no mechanical moving parts, simple structure and higher efficiency in unit volume or weight. Gallium Antimonide is the most used material in thermophotovoltaic cells. Compare to conventional photovoltaics, the efficiency is increased since the diode has a bandgap matching the peak emission of the radiator [27].

1.2.5. Thermionic Emission

A basic thermionic converter consists of a hot cathode, which emits electrons into the vacuum or a gas-filled space and collected by a cold anode [28]. As shown in Figure 1.5, the two electrodes are connected by conducting leads to two power terminals.

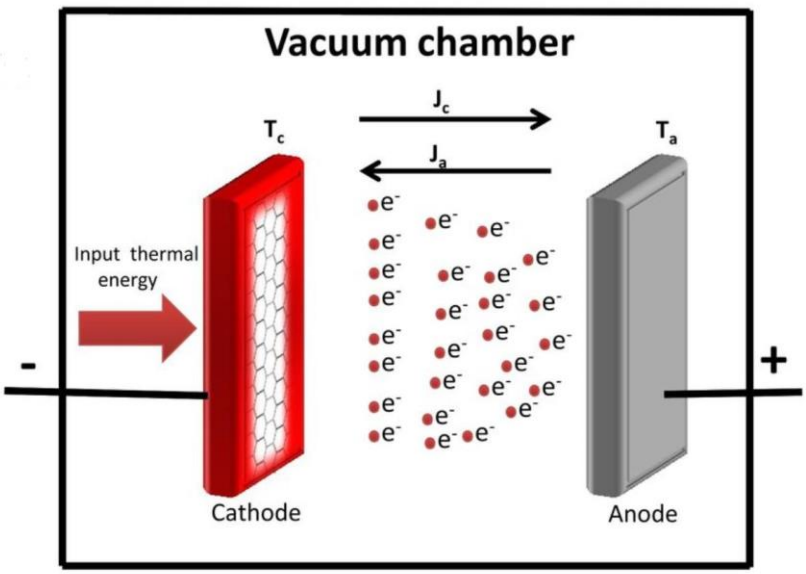

Figure 1.5 Schematic diagram of the electron thermionic emission process [29].

In the mid-18th century, Charles François de Cisternay Du Fay, a French chemist, found that electricity can be conducted in gaseous matter (Plasma) adjacent to a hot body. In the 1880s, Thomas Edison applied for a patent of thermionic emission in a vacuum [30]. In his patent, he stated that a current passed from a heated filament of an incandescent electric lamp to a conductor in the same glass globe. In 1899, J.J. Thomson defined the nature of the negative charge carriers. In the 1950s, George N. Hatsopoulos described in detail of thermionic devices [28]. Due to its solid-state characteristics and relatively low weight, thermionic space reactor development programs were conducted in the US, France and Germany in the 1970s [31]. Unlike photovoltaics, the theoretical conversion efficiency of thermionics is >60% under ideal conditions [28]. In 1998, the Japan Solar Upper Stage programme achieved a conversion efficiency of 23.2% at the operating temperature of 1577°C [32]. In 2010s, a new thermionic conversion mechanism called photon-enhanced thermionic emission (PETE) was developed by Stanford University which pushed the conversion efficiency above 50% [33].

In a similar way to thermoelectric converters, thermionic converters utilise heat as the source of energy. However, thermionic converters have a higher efficiency because they operate at much higher temperature than thermoelectric converters [34].

The major challenge for thermionic converters is that they require relatively high operating temperature (>1000 K). However, recent research showed that nano diamond lays grown on the emitter surface could reduce the operating temperature to ~600°C

[35]. This project collaborated with School of Physics and School of Chemistry in the University of Bristol. They have presented that Nitrogen-doped diamond thin films deposited on molybdenum substrates as the thermionic emitters enhanced the thermionic emission current and lowered the emission threshold temperature [36]. The main goal of this project is to achieve highest temperature possible using laser machined molybdenum absorber in a vacuum device.

1.3. Outline of Thesis

The introduction has covered the motivation of the research of renewable energy. The history and theory of photovoltaics and solar thermal technologies have been reviewed. We have introduced thermionic emission which is the primary goal for the research in this thesis.

Chapter 2 will introduce the theories of heat transfer including conduction, convection and radiation. These will help us understand the simulations and measurements in the following chapters. We will also give a review on recent researches of selective surfaces.

Chapter 3 will give a detailed description of the modelling methods. Finite element method based COMSOL Multiphysics will be used for modelling heat transfer throughout the thesis. Finite-difference time-domain based Lumerical solutions will be used to predict the optical behaviour of the surfaces. Some examples are provided with these two simulation methods.

Chapter 4 will look at the fabrication technique which produced the 2D patterned molybdenum samples. Both simulation and measurements of the optical behaviour of the patterning will be shown.

Chapter 5 shows various light heating measurements on the 2D patterned molybdenum samples. The measurements are conducted using a solar simulator in lab and using solar concentrators under sun. Vacuum devices are developed and used in the heating measurements to achieve much higher temperature. The measurement results will be discussed with comparison of simulation results.

Chapter 6 will focus on thermal optimisation using COMSOL Multiphysics. A thermionic device prototype will be shown with some heating tests.

Finally, in Chapter 7, conclusions are drawn and suggestions for future works are made.

1.4. Contributions

The main contributions of the thesis are as follows:

- FDTD modelling and optical measurements showed low-cost laser micropatterned molybdenum samples have good absorptance improvement compared to flat molybdenum. It also agreed with the heating experiments in air.

- Solar heating experiments have been conducted using a vacuum chamber with a quartz holder. The molybdenum samples have been heated up to >400℃ with low

solar concentration [37].

- Heat transfer behaviour of the sample and the quartz holder has been explored using COMSOL modelling. A thermionic emission convertor prototype has been proposed and preliminary test has been done with newly designed sample and quartz holder.

2. Theory of Heat Transfer and Selective Absorbers

Solar thermal technologies convert absorbed incident radiation into different types of energy. For thermionic convertors which will be focused in this thesis, the temperature difference between the emitter and collector directly links to its efficiency. In order to achieve a higher emitter temperature, we need to understand the heat transfer theories behind the operation. This chapter will start with introducing laws of thermodynamics and three heat transfer mechanisms, thermal conduction, thermal convection and thermal radiation. Then the concept of selective surfaces and their recent researches will be covered.

2.1. Laws of Thermodynamics

The zeroth law of thermodynamics defines the concept of temperature. It states that if both thermodynamic systems are in thermal equilibrium with the third system, the two

systems must also be in thermal equilibrium with each other. The state function of the heat balance system is defined as the temperature. It is the necessary condition for thermal equilibrium at equal temperatures [38].

The first law of thermodynamics is the extension of the law of conservation of energy to non-isolated systems [39]. When thermal energy and other forms of energy are converted to each other, the total amount of energy remains the same.

The second law of thermodynamics quantitatively defines the concept of entropy and is used to determine the phase in which any phenomenon may occur. Entropy is a measure of the total amount of energy that cannot do useful work in terms of dynamics [40]. It can also be described as a measure of randomness of a system. For example, ice cubes have lower entropy compared to water when they have same number of molecules. Heat cannot be spontaneously, unconditionally transmitted from a low temperature object to a high temperature object. It is impossible to make a heat engine that works in a cycle, taking heat from a single high-temperature heat source to completely convert it into useful work without radiating heat to the low-temperature heat source.

The third law of thermodynamics is also called Nernst's theorem. It states that no system can reduce its temperature to 0 K with limited steps [41].

2.2. Carnot's theorem

Based on the second law of thermodynamics, heat will not flow from a cooler body to a hotter body unless other work has been done to the system. It also limits the efficiency of the conversion of thermal energy to work. The maximum efficiency possible for any engine taking heat from a hotter body at temperature T_H and releasing heat to a cooler body at temperature T_C is giving by Carnot's theorem [42]:

$$\eta_c = 1 - \frac{T_C}{T_H} \tag{2.1}$$

In a solar thermal converter system, the overall efficiency is the product of the efficiencies of subsystems. One subsystem is the solar radiation transformed into useful thermal energy. The second subsystem is the useful thermal energy transformed into work by a heat engine. Figure 2.1 shows the maximum efficiencies of the overall system and each subsystem at different operating temperature.

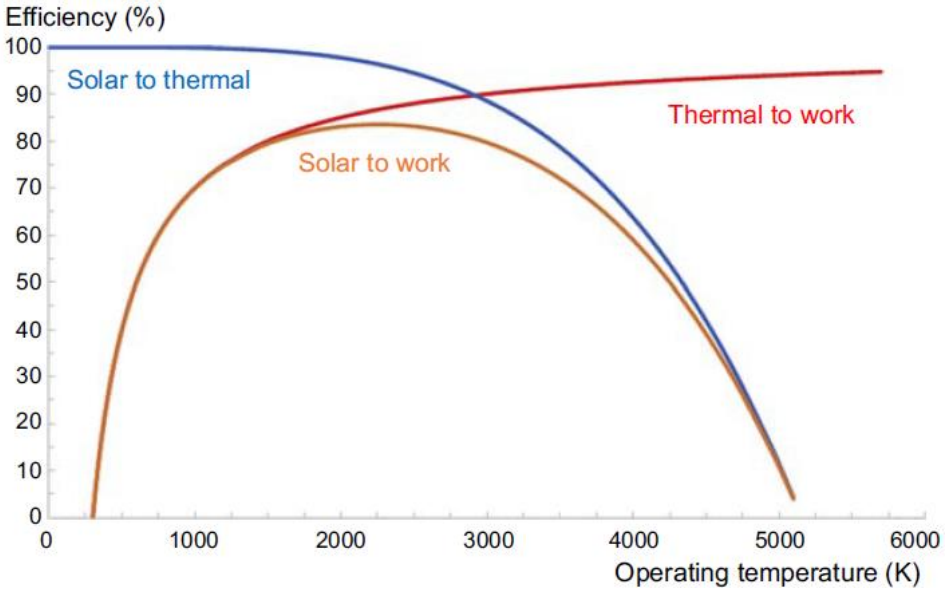

Figure 2.1 Solar to thermal, thermal to work and solar to work efficiencies in a solar thermal system [42].

2.3. Conduction

Thermal conduction is the process of transferring thermal energy from high temperature to low temperature [43]. Thermal conduction is the primary method of heat transfer in solids. The thermal conductivity is a measure of the ability to conduct heat. Metals are good thermal conductors which have higher thermal conductivity. On the other hand, Materials like glass, wood and gases are less thermal conductive.

The rate of heat transfer per area in the x-direction q_x through conduction depends on the temperature gradient dT/dx.

$$q_x = -k\frac{dT}{dx} \qquad 2.2$$

Equation 2.2 is called Fourier's law [44] and k is the thermal conductivity of the material (W/(m·K)).

As shown in Figure 2.2Figure 2.2, Fourier's law can be expressed as equation 2.3 when considering one-dimensional thermal conduction in a solid.

$$q_x = -kA\frac{T_2 - T_1}{\Delta x} \tag{2.3}$$

where T_1 and T_2 are the temperature of the different side of the solid. Δx is the thickness of the solid and A is the cross-section area.

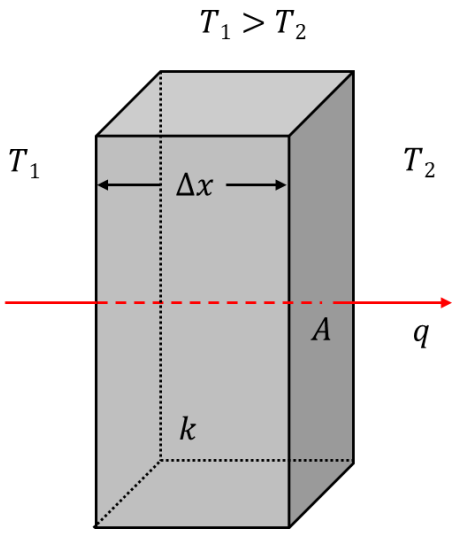

Figure 2.2 One-dimensional heat transfer through a solid

Figure 2.3 shows the heat flow from a hotter solid A to a cooler solid B. There is thermal contact resistance between the two solids due to imperfect contact. Thermal contact conductance, which is the inverse of the thermal contact resistance, is influenced by many factors such as surface roughness [45], deformations [46] and contact pressure

[47]. The equation [43] can be derived from equation 2.3.

$$q_x = -\frac{T_2 - T_1}{\Delta x_A/(k_A A) + 1/(h_c A) + \Delta x_B/(k_B A)} \tag{2.4}$$

where Δx_A and Δx_B are the thickness of solid A and solid B. k_A and k_B are the thermal conductivities of solid A and solid B. h_c is the thermal contact conductance.

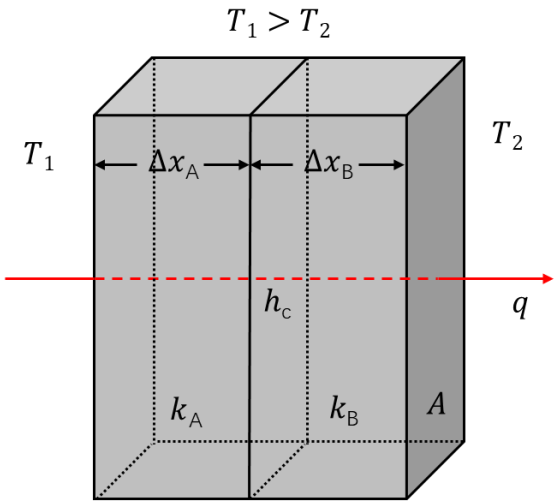

Figure 2.3 Heat transfer between two solids in contact

2.4. Convection

Thermal Convection is a process of transferring heat from a hot place to a cold place by the movement of fluids [43]. There are two forms of thermal convections, forced convection and natural convection. Natural convection is often caused by uneven temperature. Forced convection is often caused by external influences. Convection can be described by Newton's law of cooling [48].

$$q = hA(T_f - T_o) \quad 2.5$$

Where q is the heat transfer rate, h is the heat transfer coefficient, A is the area of the object, T_f is the temperature of the fluid and T_o is the temperature of the object's surface. The heat transfer coefficient can be very different depending on fluid types, heat transfer modes and thermohydraulic conditions [43].

Theoretically, the heat transfer coefficient can be obtained through complex mathematical analysis and calculation by studying the physical model of convection and momentum transfer. However, there is no mathematical model to solve all practical problems. Therefore, the heat transfer coefficient can only be determined experimentally in complex models.

Various researchers [49, 50] have provided correlations to estimate the convective heat transfer coefficient in different cases. Three dimensionless numbers, the Nusselt number Nu, the Rayleigh Number Ra, the Grashof number Gr and the Prandtl number Pr are used in the correlations. They can be derived from the following equations.

$$Nu = \frac{hL}{k} \quad 2.6$$

$$Ra = Gr\ Pr \quad 2.7$$

$$Gr = \frac{\rho L^3 g\beta(T_o - T_f)}{\mu^2} \quad 2.8$$

$$Pr = \frac{c_p \mu}{k} \quad 2.9$$

Where L is the characteristic length, ρ is the fluid density, g is the acceleration due to gravity, β is the thermal expansion coefficient, α is the thermal diffusivity and μ is the dynamic viscosity, c_p is the specific heat capacity of the fluid.

Churchill and Chu [49] developed the relation for free convection and external laminar flows for vertical plane.

$$Nu = 0.68 + \frac{0.67Ra^{1/6}}{\left(1+(0.492/\mathrm{Pr})^{9/16}\right)^{4/9}} \quad 2.10$$

W.H.McAdams [50] developed the relation for horizontal plane. For the hotter surface facing upward,

$$Nu = 0.14Ra^{1/3} \quad 2.11$$

For the hotter surface facing downward,

$$Nu = 0.27Ra^{1/4} \quad 2.12$$

2.5. Radiation

In this section, I will introduce the third mode of heat transfer, thermal radiation. Thermal radiation is a heat transfer method in which an object radiates heat outward by electromagnetic radiation. Any object temperature above 0 K will release heat radiation. Thermal radiation does not require direct contact between objects. When heat is

transferred by heat radiation, no medium is required. It also does not require an intermediate medium and can be delivered in a vacuum, and it is most effective in a vacuum. Thermal radiation is one type of electromagnetic radiation and it is propagated at the speed of light. The relation between the propagational speed, wavelength and frequency is:

$$c = f\lambda \tag{2.13}$$

where c is the speed of light, f is the frequency and λ is the wavelength.

Figure 2.4 shows a portion of the electromagnetic spectrum. Thermal radiation lies between 0.1 to 100 μm and it includes the visible light, parts of ultra-violet and infrared.

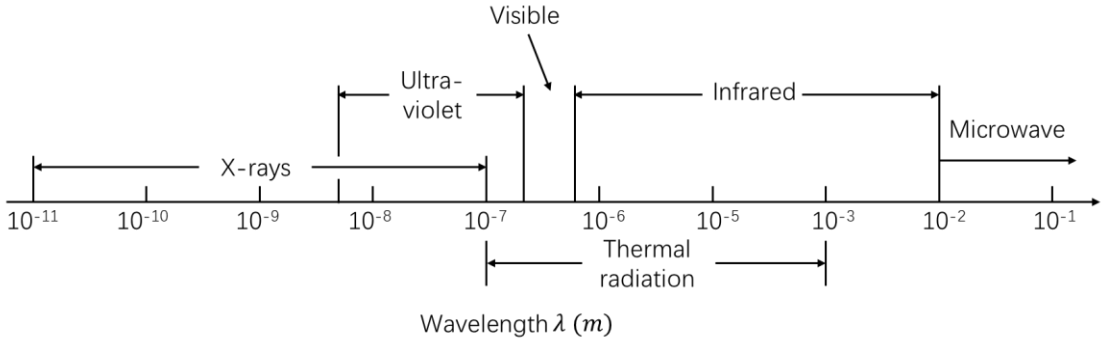

Figure 2.4 Electromagnetic spectrum

When thermal radiation Q_i is projected onto the surface of a body, it follows the law of visible light. Some of which is absorbed by the object Q_α, partially reflected Q_ρ, and the rest is transmitted through the object Q_τ. Hence,

$$Q_i = Q_\alpha + Q_\rho + Q_\tau \quad 2.14$$

$$1 = \frac{Q_\alpha}{Q_i} + \frac{Q_\rho}{Q_i} + \frac{Q_\tau}{Q_i} \quad 2.15$$

We define the absorptivity $\alpha = Q_\alpha/Q_i$, the reflectivity $\rho = Q_\rho/Q_i$ and the transmissivity $\tau = Q_\tau/Q_i$. Thus,

$$\alpha + \rho + \tau = 1 \quad 2.16$$

For most solids, the transmissivity equals to zero. Therefore, $\alpha + \rho = 1$, and we will only discuss the absorptivity and reflectivity in the following sections.

2.5.1. Blackbody Radiation

A blackbody is an ideal object that is capable of absorbing all of the electromagnetic radiation of any frequency and direction of incidence [51]. It was proposed by Gustav Kirchhoff in 1860 and introduced into thermodynamics [52]. According to this definition, the reflectivity and the transmissivity of the blackbody are both 0 and the absorptivity is 1. Due to the differences in the material properties of the objects in nature, their absorptivity, reflectivity and transmissivity can be very different, which brings great difficulties to the study of thermal radiation. Therefore, the blackbody is usually used as an idealised object in the research.

An example of a blackbody is a small hole in a cavity with dark walls [53]. Any light entering the small hole will be reflected or absorbed by the wall in the cavity, leaving

only a very small amount of light to be emitted from the hole. Hence, almost all incident light was absorbed.

Planck's law is one of the most basic laws in blackbody radiation theory, which reveals the relationship between the spectral radiance of a blackbody B_λ and the wavelength λ and temperature T. The formula of Planck's law [54] is

$$B_\lambda(\lambda, T) = \frac{2hc^2\lambda^{-5}}{e^{hc/\lambda kT}-1} \quad 2.17$$

where the spectral radiance is the radiant flux absorbed, reflected, emitted or transmitted by a surface per unit solid angle, per unit area and per unit wavelength. Its unit is W·sr^{-1}·m^{-3}. h is the Planck constant with the value of 6.625×10^{-34} J·s. k is the Boltzmann constant with the value of 1.38×10^{-23} J/K. c is the speed of light 3×10^8 m/s. Planck's Law can also be written as

$$u_\lambda(\lambda, T) = \frac{8\pi hc\lambda^{-5}}{e^{hc/\lambda kT}-1} \quad 2.18$$

where u_λ is the spectral irradiance which is obtained by multiply the spectral radiance and the total solid angle of a sphere (4π steradian). The unit is W·m^{-3}. When equation 2.17 is integrated over the wavelengths from 0 to ∞, we can have the Stefan-Boltzmann law.

$$E = \int_0^\infty B_\lambda(\lambda, T)d\lambda = \int_0^\infty \frac{2hc^2\lambda^{-5}}{e^{hc/\lambda kT}-1}d\lambda = \sigma T^4 \quad 2.19$$

where E is the irradiance with the unit of W·m^{-2} and σ is the Stefan-Boltzmann

constant, which is

$$\sigma = \frac{2\pi^5 k^4}{15h^3c^2} = 5.669 \times 10^{-8} W/m^2 \cdot K^4 \qquad 2.20$$

Figure 2.5 shows the blackbody spectral irradiance curve with temperature in the range of 300~450 K. The dotted line in the figure shows the position of the radiation peaks. We can see that the spectral radiation emittance of the blackbody changes continuously with the wavelength, and there is a radiation peak at each temperature. The spectral irradiance of the blackbody increases as the temperature increases. The peak wavelength of the blackbody spectral irradiance moves toward the shorter wavelength as the temperature increases.

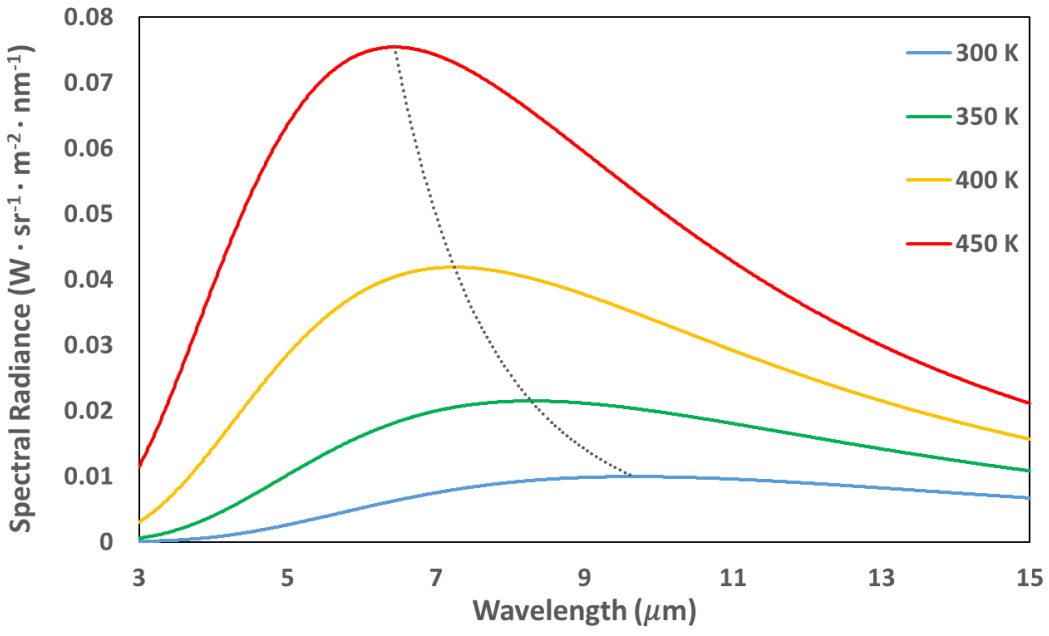

Figure 2.5 Blackbody spectral radiance at different temperatures [55]

The peak wavelength of the blackbody spectral irradiance λ_{max} can be given by Wien's law of displacement [56].

$$\lambda_{max}T = b = 2.898 \times 10^{-3} m \cdot K \quad 2.21$$

where b is Wien's displacement constant.

In summary, Planck's law describes the distribution of the blackbody radiation. The blackbody radiation has a peak in the spectrum at a certain temperature, which is determined by Wien's law of displacement. The total irradiance of a blackbody is obtained by the Stefan-Boltzmann law.

2.5.2. Kirchhoff's Law

The absorptance is a property of a surface. It is the fraction of the incident radiation that is absorbed by the surface. However, this property depends on both the wavelength λ and the angle of the incident radiation μ (polar angle), ϕ (azimuthal angle). In equation form [57]:

$$\alpha_\lambda(\mu, \phi) = \frac{I_{\lambda,\alpha}(\mu,\phi)}{I_{\lambda,i}(\mu,\phi)} \quad 2.22$$

where α_λ is the monochromatic directional absorptance, subscripts α and i mean absorbed and incident.

All the radiation that is absorbed by a surface (not depending on the incident angle and

wavelength) is called the directional absorptance and is defined by the following equation:

$$\alpha(\mu,\phi) = \frac{\int_0^\infty \alpha_\lambda(\mu,\phi) I_{\lambda,i}(\mu,\phi)\, d\lambda}{\int_0^\infty I_{\lambda,i}\, d\lambda} \quad 2.23$$

The directional absorptance α is not a property of the surface because it depends on the wavelength of the incident radiation.

The emittance is also a property of a surface. It is the ratio of the radiation emitted by a surface to the radiation emitted by a blackbody at the same temperature. This property depends on the angle of the emitted radiation. In equation form:

$$\varepsilon_\lambda(\mu,\phi) = \frac{I_\lambda(\mu,\phi)}{I_{\lambda b}} \quad 2.24$$

The monochromatic directional emittance ε_λ is a property of a surface, as is the directional emittance ε, defined by:

$$\varepsilon(\mu,\phi) = \frac{\int_0^\infty \varepsilon(\mu,\phi)\, I_{\lambda b}\, d\lambda}{\int_0^\infty I_{\lambda b}\, d\lambda} \quad 2.25$$

All objects have a temperature and emit electromagnetic radiation. The objects above absolute zero can produce thermal radiation. The higher the temperature, the greater the total radiated energy and the peak emission shifts to shorter wavelength range. The radiation and absorption of an object are related to their temperature, surface area and blackness, etc. In thermal equilibrium, the ratio of the radiation to absorption of an object is only a function of its temperature and the wavelength. The property of the

object is not affected this ratio. In a word, at the same temperature, the monochromatic absorptance and the monochromatic emittance are equal at the same wavelength. This is called Kirchhoff's law:

$$\varepsilon = \alpha \tag{2.26}$$

As discussed before, three phenomena occur when radiation energy strikes on the surface of an object which are absorption, reflection and transmission.

According to Kirchhoff's law:

$$\varepsilon_\lambda(\mu, \varphi) = \alpha_\lambda(\mu, \varphi) = 1 - R_\lambda(\mu_i, \phi_i) - T_\lambda(\mu_i, \phi_i) \tag{2.27}$$

where $\rho_\lambda(\mu_i, \phi_i)$ is the monochromatic angular-hemispherical reflectivity and $T_\lambda(\mu_i, \phi_i)$ is the monochromatic angular-hemispherical transmittance.

The transmittance equals to zero for opaque surfaces, equation 2.27 becomes:

$$\varepsilon_\lambda(\mu, \varphi) = \alpha_\lambda(\mu, \varphi) = 1 - R_\lambda(\mu_i, \phi_i) \tag{2.28}$$

2.5.3. Selective Surfaces

Kirchhoff's Law states that $\varepsilon = \alpha$. However, it requires the same temperature for the object and source. For solar thermal devices, their temperatures are significantly lower than the radiation source. Figure 2.6 shows the blackbody emission at 5500 K which is approximately the temperature of the sun and at 1000 K which is the temperature of the

thermionic emitter. According to the spectral radiance spectrum of the sun and the low temperature blackbody, most solar radiation lies at short wavelength range (less than 3μm) where the radiation of the absorbing surface lies at long wavelength range. In order to maximise the absorption of solar radiation while minimising the emitted radiation of the absorbing surface, it is necessary to manipulate the absorptance of the surface, that is, create a selective surface.

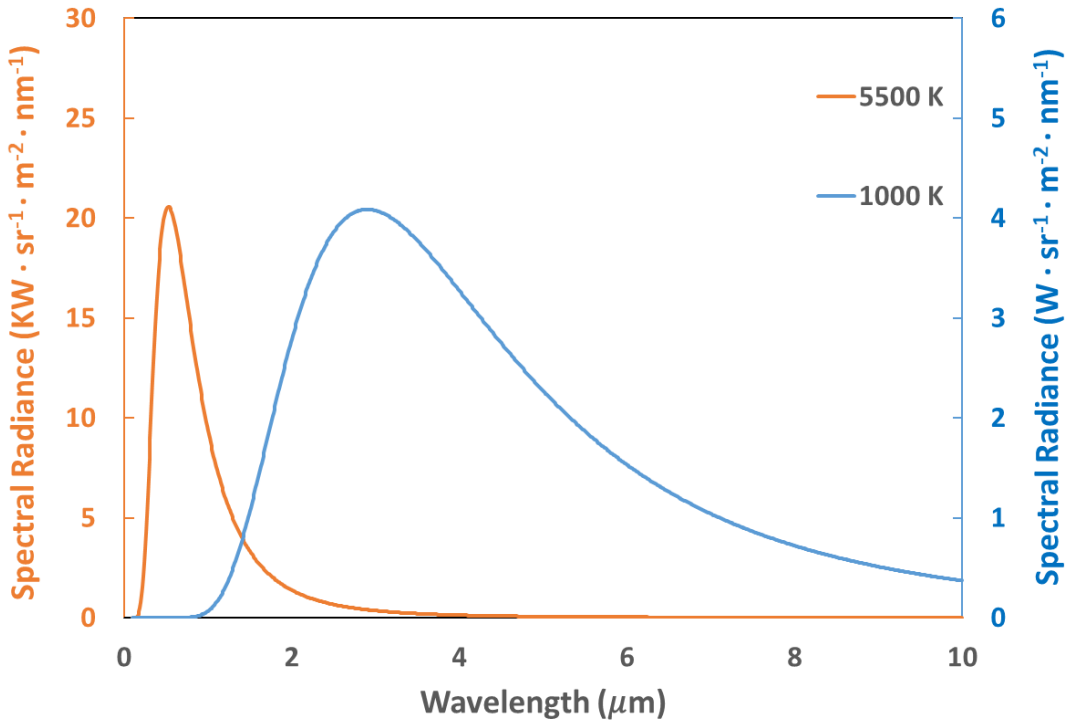

Figure 2.6 Blackbody spectral radiance at 5500 K (orange) and 1000 K (blue), the scale of the spectral radiance of 5500 K is on the left axis and the scale of the spectral radiance of 1000 K is on the right axis [55]

2.6. Current selective surfaces

Tabor [58] first introduced the concept of solar selective absorbers. For decades, selective absorbers have been a very active research topic in the field of solar thermal technology. The design of ideal selective absorbers can be categorised into six different types as shown in Figure 2.7.

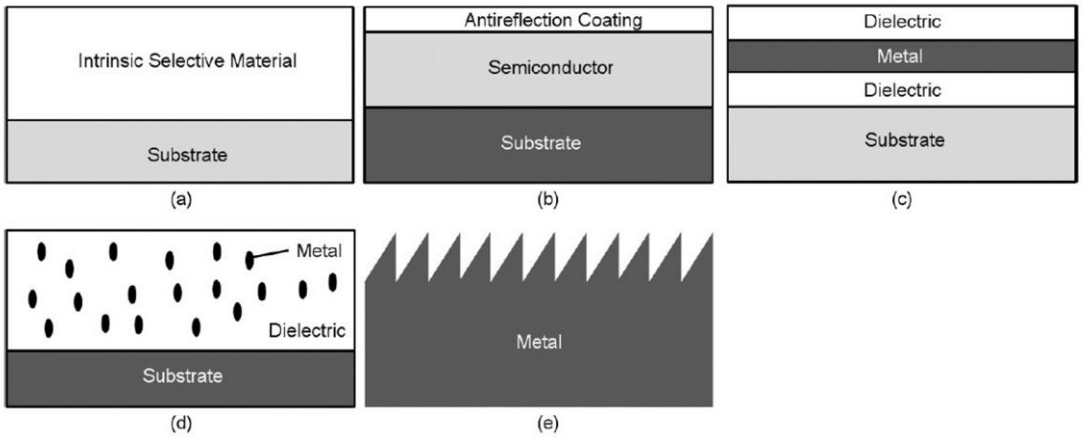

Figure 2.7 Schematic design of solar selective absorbers, (a) Intrinsic absorbers, (b) Semiconductor-metal tandems, (c) Multilayer absorbers, (d) Cermets (metal-dielectric composites), and (e) Surface texturing [59]

2.6.1. Intrinsic absorbers

Materials with good absorption properties can often be directly used in selective absorbers, that is, intrinsic selective material. It can be prepared into a film with a thickness of several hundred nanometres or even several tens of nanometres and coated on a metal substrate, based on its strong intrinsic absorption. This design is simple and

easy to implement and it is widely used in early days. Common materials are copper oxide, black chrome and black nickel [60]. In recent years, some polymetallic oxides and nitrides have been reported to have good absorbing properties, such as $CuMn_2O_4$ [61], $CuMnO_x$ [62], TiAlN [63], $TiAlO_xN_y$ [64], NbTiON [65], HfMoN [66], etc. ZrB_2 on Si_3N_4AR showed α=0.93 and ε=0.09 at 375K [67]. However, it has obvious limitations when relying only on the intrinsic absorption of the material to improve the absorption performance. The intrinsic materials with high absorptivity are limited and their cut-off wavelength can be very short. Therefore, it is not the ideal choice for selective absorbers and often combined with other absorption mechanisms to further improve absorption efficiency.

2.6.2. Semiconductor-metal tandems

Semiconductor materials have intrinsically selective absorption characteristics because they can effectively absorb photons at high frequencies and are transparent to photons at lower frequencies due to the semiconductor bandgap. Selective absorption can be achieved if a semiconductor coating is deposited on a metal substrate due to the high reflectance at longer wavelength of the metal. Semiconductors generally have higher reflectance in the short wavelength range so it is necessary to add an anti-reflection coating to improve transmission [68]. Amorphous silicon film was used in a selective absorber and it had α=0.79~0.81 and ε=0.1~0.12 at 400℃ [69]. Chatterjee and Pal [70] used thermal evaporation technique to deposit a coating of galena which had

α=0.95~0.97 and ε=0.21~0.27 at 375 K. Bermel [71] simulated silicon as an absorber which had α=0.868 and ε=0.073 at 1000 K. Although semiconductor materials have certain selective absorption properties, they have poor oxidation resistance and do not have long-term thermal stability.

2.6.3. Multilayer absorbers

A multilayer absorber is composed of alternating metal and dielectric layers. The dielectric layer acts as an absorber and the metal layer acts as a reflector. It can effectively reduce the reflection and improve the absorptivity without affecting the infrared radiation transmittance, and effectively improve the performance of the selective surface. Multilayer absorbers can be easily modelled with Finite Difference Time Domain. Sergeant [72] modelled two multilayer absorbers. One with W, TiO_2 and MgF_2 showed α>0.94 and ε<0.07 at 720 K. Another with Mo and MgO showed α>0.85 and ε<0.16. Liu [73] reported a six-layer structure with SiO_2, Ti and Cu which had α=0.955 and ε=0.136 at 700 K with good thermal stability. Num [66] prepared a three-layer MgO/Zr/MgO using e-beam evaporation. It had α=0.92 and ε=0.1 at 400°C. Barshilia [74] fabricated an Al_xO_y/Al/Al_xO_y multilayer absorber. The top Al_xO_y layer acted an AR coating and the middle Al layer acted as an IR reflector. This multilayer absorber exhibited high selectivity of α=0.97 and ε=0.05 at 82°C. Selvakumar [75] optimised HfO_x/Mo/HfO_2 multilayer absorber on CU substrate with α= 0.905–0.923 and ε= 0.07–0.09 at 82°C.

2.6.4. Cermets

Metal-dielectric composite, also called cermet is composed of metal nanoparticles randomly embedded in a ceramic matrix [76]. The metal nanoparticles can effectively absorb solar radiation through electronic transitions, and are transparent to infrared radiation. The surface selectivity of the cermet coating can be effectively controlled by varying the size, shape and distribution of the metal nanoparticles in the ceramic medium [77]. It can achieve high solar absorption and low infrared emission by depositing a cermet coating on a highly reflective metal, and adding an anti-reflection layer on the top surface. Among different types of selective absorbers for the solar spectrum, the preparation method of the cermet coating is relatively cheap, and the optical performance of the coating is controllable. The performance is stable at temperatures below 500℃ and it is one of the most successful commercialisation, mainly used in vacuum tube collectors [78]. Gaouyat [79] reported $NiCrO_x$ selective absorber cermets which had α=0.94 and ε=0.02 at 373 K. Cao [80] showed W-Ni-Al_2O_3 cermet-based selective absorber with $\alpha\approx$0.9 and ε=0.15 at 500℃. Zhang [81] designed a Mo- Al_2O_3 cermet which had α=0.96 and ε=0.11 at 350℃. Chester [82] fabricated a 4-layer SiO_2-W cermet absorber which achieved high selectivity with α=0.979/ε=0.042 at 400K and α=0.945/ε=0.172 at 1000K.

2.6.5. Surface texturing

Surface texturing can effectively improve the absorption of the surface because the

incident radiation is reflected multiple times inside the structure so that the energy is trapped inside the surface. There are many types of surface texturing which have been reported such as Pyramid-shaped surfaces [83, 84], V-groove surfaces [85, 86], irregular rough surfaces [87, 88], columnar surfaces [89, 90], porous surfaces [91, 92], nanowire and nanocone arrays [93]. Tungsten whiskers grew on chromium showed α=0.98 and $\varepsilon = 0.26$ at 550℃ [95]. Kussmaul [96] showed an ion beam treated copper surface which had α=0.983 at 900K. Recently, hydrogenated amorphous silicon (a-Si:H) nanocones and nanowire were grew on an indium-tin-oxide (ITO) substrate with Chlorine-based reactive ion etching process. The nanocones showed α>0.93 between 400-650nm which was significantly higher than the flat surface (α=0.64). The nanocones structure also outperformed the nanowires due to the gradual change of the effective refractive index between the air and the surface [94]. Although the structured surface exhibits greater thermal stability than cermets, its emissivity is generally higher which increases its energy loss. This thesis will focus on this technique and 2D disordered periodic surface structuring will be fabricated using laser etching.

2.7. Chapter Conclusion

This chapter has covered the theories of heat transfer, which includes thermal conduction, convection and radiation. Important principles such as Planck's law, Stefan-Boltzmann law and Kirchhoff's Law were introduced. Various types of selective surfaces were presented, along with their previous researches. The next chapter will

introduce the computational methods used to analyse the thermodynamics of solar thermal application and design and characterise the micro-structures.

3. Computational Methods

3.1. Simulation methods for heat transfer

COMSOL Multiphysics [97] is a simulation tool based on the Finite Element Method (FEM) for various mathematics, physics and engineering applications. It solves single field or multifield the partial differential equations (PDE) to realise the simulation of real physical phenomena, and uses mathematical methods to solve real world physical phenomena. It has a large number of predefined physical application modes, ranging from fluid flow, heat transfer, to structural mechanics, electromagnetic analysis and other physical fields. The definition model in COMSOL is very flexible. The material properties, source terms, and boundary conditions can be constants, functions of arbitrary variables, logical expressions, or an interpolation function directly representing the measured data. The main advantage of this software is the multiphysics coupling. The predefined multiphysics application modes can solve many common

physical problems. At the same time, users can also choose the physics fields they need and define their relationships.

3.1.1. The Finite Element Method

FEM is an approximate numerical method developed based on the rapid development of modern computers. It is used to solve PDEs with specific boundary conditions in mechanics and mathematics [98, 99]. These PDEs are the basis of solid mechanics and fluid mechanics problems that are common in engineering practice. The development of finite elements and computers together form the basis of modern computational mechanics. The core idea of FEM is "Numerical Approximation" and "Discretisation", so its historical development also revolves around these two points.

FEM originally originated from the study of elastic and structural analysis problems in civil and aeronautical engineering. The earliest development of FEM can be found in the work of A. Hrennikoff [100] and R.Courant [101] in the 1940s. The methods used by these pioneers are very different, but they have the same essential feature which is the use of grid discretisation to transform a continuous region into a group of discrete subregions, often called elements. Hrennikoff's work discretises using grid-like discrete regions [100]. Courant's method decomposes a region into a finite number of triangular sub-regions, which is used to solve the second-order elliptic partial differential equations derived from the cylindrical torque problem [101]. Courant's contribution propelled the development of FEM and plotted the results of earlier studies of partial

differential equations. The development of FEM began in the mid-to-late 1950s in the use of fuselage frames and structural analysis, and in the 1960s it was used in civil engineering by J.Argyris and R.W. Clough [102].

3.1.2. Numerical Approximation

Before FEM was invented, all PDEs in mechanical problems could only be solved by simple analytical solutions which is mathematically demanding and relies on idealised assumptions. Once the mechanical problems become more complicated, we cannot directly use the analytical methods, or the answers of the analytical solutions are too large. FEM discretises the overall structure into a finite number of elements. The idealised assumption and mechanical equation are applied to each element inside the structure. Then the overall mechanical equation of the structure is obtained by element analysis and the problem is solved by boundary conditions and constraints. One-to-one mapping of the total reaction can then be used to obtain the response of each unit in the entire structure, thereby avoiding the mechanical and mathematical models of complex structures [103].

3.1.3. Discretisation

A continuous medium is discretised into several simple basic geometric units, namely elements. These elements are interconnected through nodes. This process is commonly referred to as meshing. For the element, you can use the method of Numerical

Approximation to solve, and then combine the results of the element into the result of the entire domain through the connection between nodes, that is, assemble the stiffness matrix. The study of discretisation and corresponding element characteristics and convergence is also an important research area in finite elements. In general, finite elements are mainly divided into 1D, 2D and 3D geometries. Figure 3.1 shows some examples of the geometries for the elements. Each element can increase the order of the shape function (the number of control point nodes) to improve the accuracy.

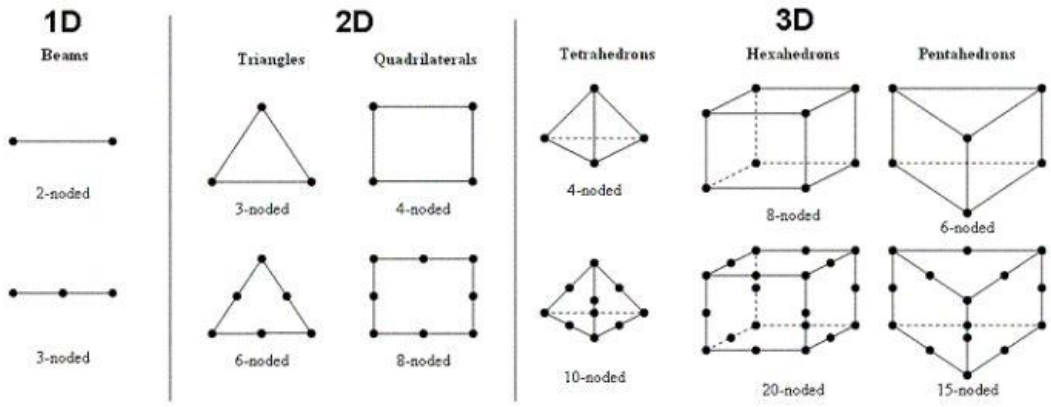

Figure 3.1. Geometry and node placement for 1D, 2D and 3D linear elements. [104]

3.1.4. An example of heat transfer simulation with COMSOL Multiphysics

As shown in Figure 3.2, a thin metal disc sits on a quartz disc. The top surface of the metal disc is heated with a 10W plane heat source. The ambient temperature is fixed at 293.15 K. The heat loss of the overall system is from the surfaces via radiation and free convection. The emissivity of the surface of the metal is 0.3 and the absorptivity is 0.6.

The emissivity of the surface of the quartz is 0.9. Typically, the convective heat transfer coefficient for air natural convection is 0.5-1000 W/(m^2·K) [105]. The thermal contact conductance of solid-solid joints is 100-10000 W/(m^2·K) [106]. Here, the convective heat transfer coefficient of all surfaces is assumed to be 20 W/(m^2·K). Due to the roughness and unflatness of the metal disc and quartz, the thermal contact conductance is assumed to be 1000 W/(m^2·K). Here, we used the default mesh settings in the COMSOL simulation. The mesh of the geometry is showed in Figure 3.3 (a). The geometry consists of 1708 tetrahedras. The simulation time was 28s and the required physical memory was 1.38GB. If a finer mesh was established with 14476 tetrahedras, the simulation time increased to 138s and the required memory was 3.2GB. The simulation results were identical. It indicates that modifying the mesh can mimise calculation time and required memory. However, finer meshing may required for smaller or key areas of the geometry in order to get accurate results.

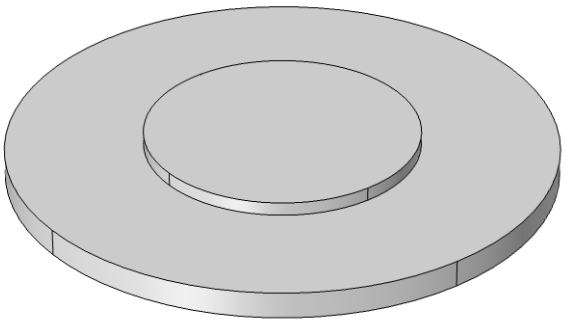

Figure 3.2 A metal disc sits on a quartz disc. The top surface of the metal disc is heated with a 10 W heat source in air.

Figure 3.3 (b) shows the temperature variation across the metal disc and the quartz after 1000 seconds of heating. We can see that the metal disc achieved approximately 435 K. Due to the low thermal conductivity of the quartz, the temperature increase across the quartz is much less. Figure 3.4 shows the simulation result for the temperature of bottom centre point of the metal disc as functions of time.

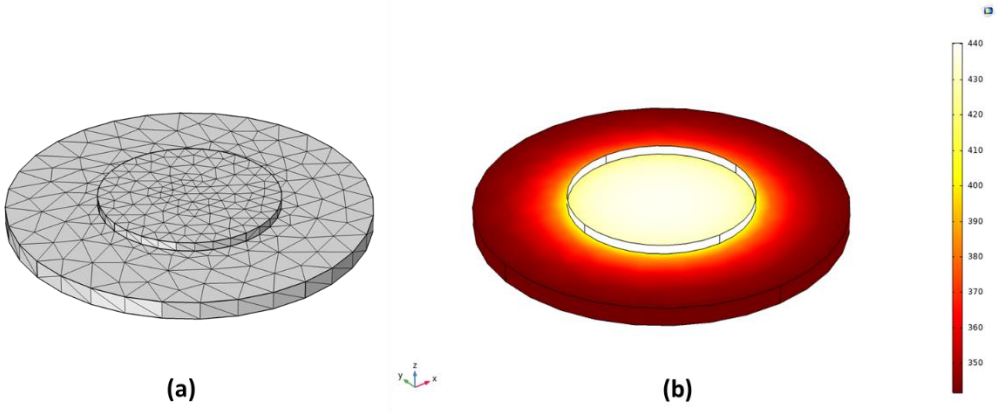

Figure 3.3 Simulation results: (a) Mesh of the geometry; (b) Temperature distribution of the system

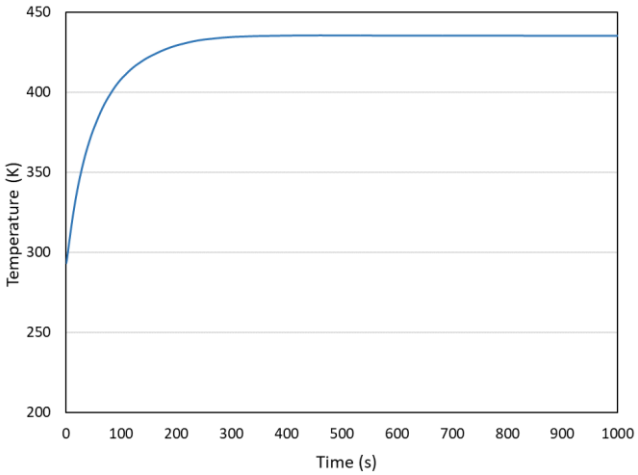

Figure 3.4 Temperature of the metal disc as functions of time

There are many parameters can be adjusted in this simulation which can change the final temperature. Here is an example shown in Figure 3.5 where we assume the convective heat transfer coefficient is 0 and 20 W/(m^2·K) and the thermal contact conductivity is 10 and 1000 W/(m^2·K). When the convective heat transfer coefficient is 0 W/(m^2·K), it means that the system is in the high vacuum which convective loss never occurs. When two objects have very poor contact, the thermal contact conductivity is assumed to be very low, such as 10 W/(m^2·K). From Figure 3.5, It can be seen that these two parameters can affect the thermal equilibrium temperature significantly.

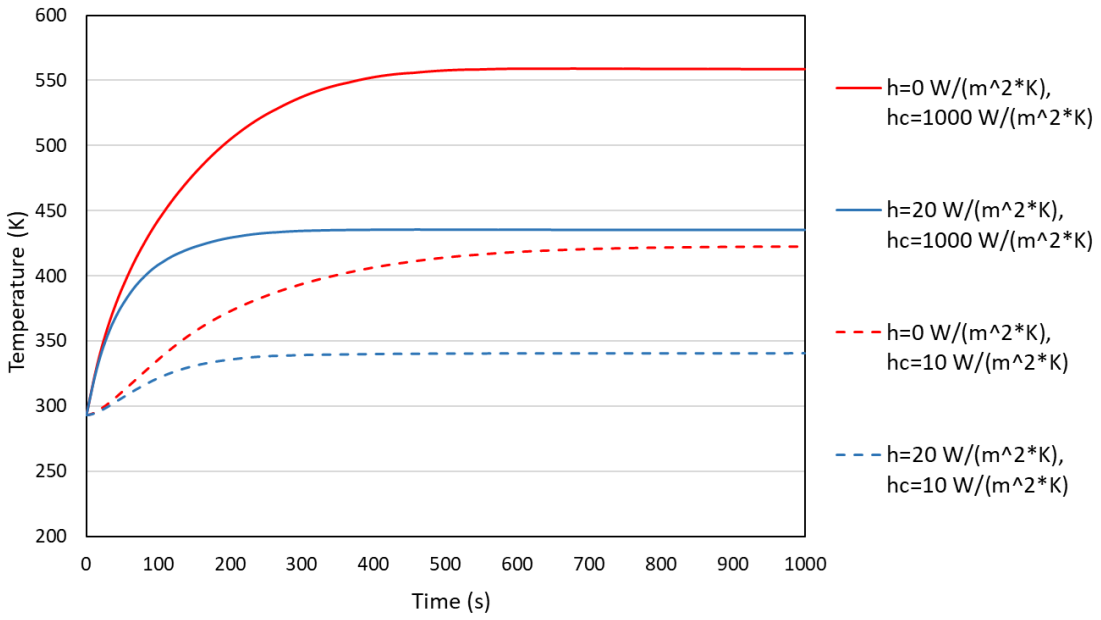

Figure 3.5 Temperature of the metal disc as functions of time when the convective heat transfer coefficient is 0 and 20 W/(m^2·K) and the thermal contact conductivity is 10 and 1000 W/(m^2·K).

3.2. Simulation methods for micro-patterned structures

Lumerical FDTD software [107] is produced by a Canadian company called Lumerical Solutions. It is used to solve a wide variety of applications involving light scattering, diffraction, and radiation. This simulation software is based on Finite-difference time-domain method (FDTD). In this thesis, the electromagnetic behaviour of the absorber will be investigated using this software.

3.2.1. The Finite-difference time-domain method

The FDTD method is a set of time-domain advancing formulas obtained by differentially discretising Maxwell's curl equations in differential form. Maxwell in 1864 summarised a set of equations that can perfectly describe all electromagnetic phenomena. This set of equations is called Maxwell's equations. The form of Maxwell's equation is very simple, and it describes the correlation between the electromagnetic field and the field source from a macro perspective. Maxwell's equations have both integral and differential forms. The finite-difference time-domain method is a technique for solving Maxwell's equations in differential form. The differential Maxwell equations are as follows [108]:

$$\nabla \times \boldsymbol{H} = \frac{\partial \boldsymbol{D}}{\partial t} + \boldsymbol{J} \tag{3.1}$$

$$\nabla \times \boldsymbol{E} = -\frac{\partial \boldsymbol{B}}{\partial t} \tag{3.2}$$

$$\nabla \cdot \mathbf{B} = 0 \tag{3.3}$$

$$\nabla \cdot \mathbf{D} = \rho \tag{3.4}$$

Where $\boldsymbol{H}$ is the magnetic field in A/m, $\boldsymbol{D}$ is the electric flux density in C/m^2, $\boldsymbol{J}$ is the electric current density in A/m^2, $\boldsymbol{E}$ is the electric field in V/m, $\boldsymbol{B}$ is the magnetic flux density in Wb/m^2 and ρ is the electric charge density in C/m^3.

Equation 3.1 is Ampéres's Law. It describes that a time-varying electric field generates a time-varying magnetic field. The time-varying magnetic field is generated by a conduction current and a displacement current together. Equation3.2 is Faraday's law of induction. It describes that a time-varying magnetic field generates a time-varying electric field. Equation 3.3 is Gauss's Law of magnetism. It states that the magnetic flux is always continuous, and the magnetic field is a divergence-free field. Equation 3.4 is Gauss's law. It states that if there is a positively charged body density at any point in space, an electric displacement line is issued at a different point and if a negatively charged body density exists, the electrical displacement line converges at this point.

For isotropic and linear materials, the relationship follows:

$$\boldsymbol{D} = \varepsilon \boldsymbol{E} \tag{3.5}$$

$$\boldsymbol{B} = \mu \boldsymbol{H} \tag{3.6}$$

$$\boldsymbol{J} = \sigma \boldsymbol{E} \tag{3.7}$$

Where ε is the permittivity in F/m, μ is the permeability in H/m and σ is the Conductivity in S/m.

With the relationship stated above, the equations 3.1 and 3.2 can be written as:

$$\frac{\partial \boldsymbol{H}_z}{\partial y} - \frac{\partial \boldsymbol{H}_y}{\partial z} = \varepsilon \frac{\partial \boldsymbol{E}_x}{\partial t} + \sigma \boldsymbol{E}_x \tag{3.8}$$

$$\frac{\partial \boldsymbol{H}_x}{\partial z} - \frac{\partial \boldsymbol{H}_z}{\partial x} = \varepsilon \frac{\partial \boldsymbol{E}_y}{\partial t} + \sigma \boldsymbol{E}_y \tag{3.9}$$

$$\frac{\partial \boldsymbol{H}_y}{\partial x} - \frac{\partial \boldsymbol{H}_x}{\partial y} = \varepsilon \frac{\partial \boldsymbol{E}_z}{\partial t} + \sigma \boldsymbol{E}_z \tag{3.10}$$

$$\frac{\partial \boldsymbol{E}_z}{\partial y} - \frac{\partial \boldsymbol{E}_y}{\partial z} = -\mu \frac{\partial \boldsymbol{H}_x}{\partial t} \tag{3.11}$$

$$\frac{\partial \boldsymbol{E}_x}{\partial z} - \frac{\partial \boldsymbol{E}_z}{\partial x} = -\mu \frac{\partial \boldsymbol{H}_y}{\partial t} \tag{3.12}$$

$$\frac{\partial \boldsymbol{E}_y}{\partial x} - \frac{\partial \boldsymbol{E}_x}{\partial y} = -\mu \frac{\partial \boldsymbol{H}_z}{\partial t} \tag{3.13}$$

The above six PDEs are the basis of the FDTD method. The method was proposed by Yee [109] for the first time in 1966. The spatial arrangement of the electric and magnetic nodes in the FDTD method is shown in Figure 3.6. This is the famous Yee cell. It can be seen that each electric field component is surrounded by four magnetic field components and each magnetic field component is also surrounded by four electric field components.

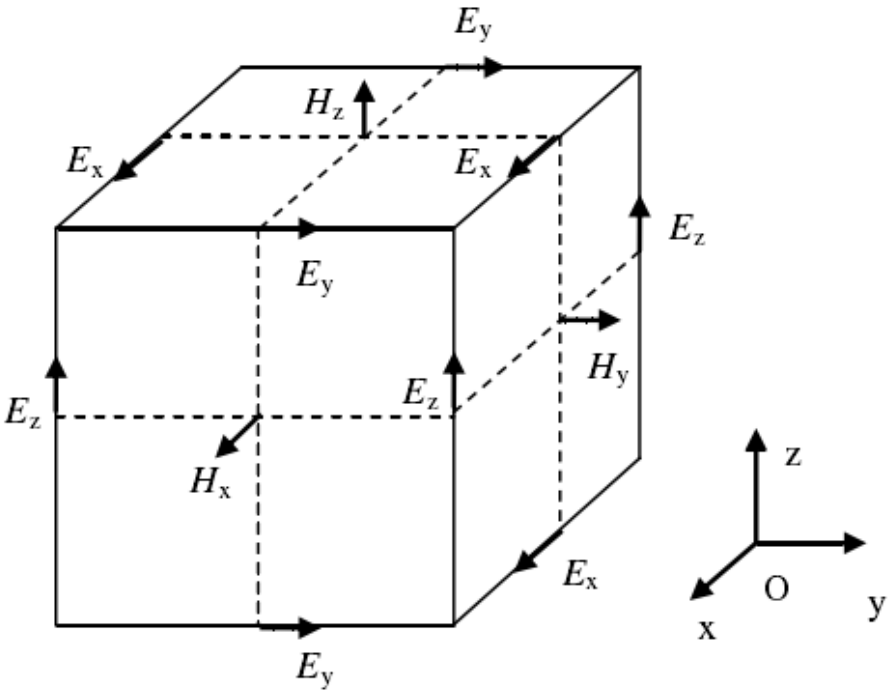

Figure 3.6 The Anatomy of the Yee cell

In time sequence, the electric and magnetic fields are sampled alternately. The sampling times are integer and semi-integer multiples of Δt, which are different from each other by half a time step, so that the Maxwell equation is discretised into an explicit difference equation. Therefore, it can be solved recursively in the time domain without performing matrix inversion. Then, for an electromagnetic problem, given its initial values and boundary conditions, the FDTD equation can be used to gradually iterate to obtain the distribution of the spatial electromagnetic field at each moment. The integer and half-integer conventions for the space nodes and time step values of the components of the electric and magnetic fields in the Yee cell are shown in Table 3.1.

Table 3.1 The sampling positions for each component in the Yee's cell

Electromagnetic field components		Space components sampling			Timeline t sampling
		x-axis	y-axis	z-axis	
$\boldsymbol{E}$ node	$\boldsymbol{E}_x$	$i + 0.5$	j	k	n
	$\boldsymbol{E}_y$	i	$j + 0.5$	k	
	$\boldsymbol{E}_z$	i	j	$k + 0.5$	
$\boldsymbol{H}$ node	$\boldsymbol{H}_x$	i	$j + 0.5$	$k + 0.5$	$n + 0.5$
	$\boldsymbol{H}_y$	$i + 0.5$	j	$k + 0.5$	
	$\boldsymbol{H}_z$	$i + 0.5$	$j + 0.5$	k	

3.2.2. An example of Lumerical FDTD simulation

Figure 3.7 shows the schematics of modelling reflectance of a piece of flat molybdenum in air. Figure 3.8 shows the 2D FDTD modelling interface. The four pictures show the front view, cross-section view, side view drawing and 3D perspective view of the 3D structure. A plane wave source (purple arrow) with wavelength range from 0.3-5.0 μm is injected on the molybdenum. Electric and magnetic fields are represented by the blue arrows. Periodic boundary condition is used in x-axis which enforce periodicity on the

fields and geometry. Perfect matched Layer (PML) is applied to y-axis and z-axis to minimise reflections back to the interior. PML was introduced by Berenger [110] in 1994 and it is a numerical boundary condition to simulate problems with open boundaries. PML can absorb outgoing light from the simulation region. The yellow line is the monitor which calculate the reflection of the field components.

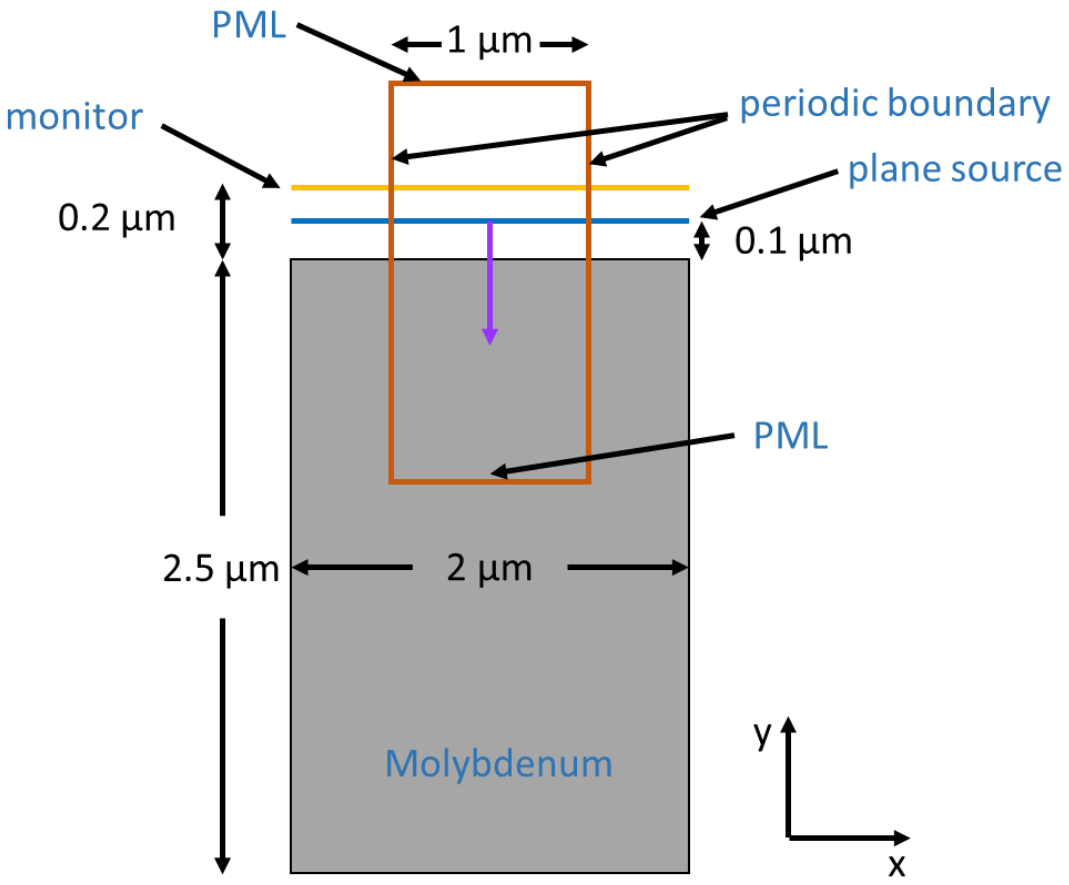

Figure 3.7 XY view of simulated 2.5 µm thick flat Molybdenum

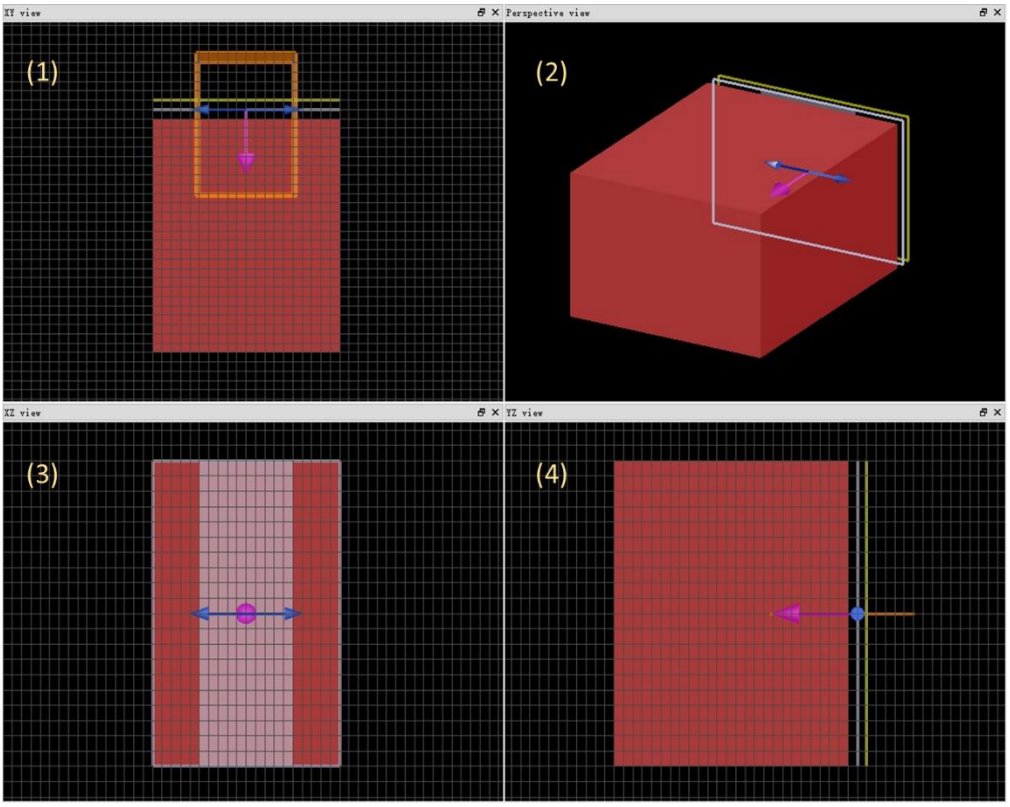

Figure 3.8 2D and 3D views of Lumerical FDTD simulation of bulk molybdenum, (1). XY view; (2). 3D view; (3). XZ view; (4). YZ view

Figure 3.9 shows the theoretical and simulated results of molybdenum. The theoretical reflectivity is calculated by the equation 3.14 and 3.15:

$$\underline{n} = n - ik \tag{3.14}$$

$$R = \left|\frac{(\underline{n}-1)^2}{(\underline{n}+1)^2}\right| \tag{3.15}$$

where $\underline{n}$ is the complex refractive index, n is the refractive index, k is the imaginary part of $\underline{n}$ which is also called extinction coefficient and R is the reflectance.

The values of refractive index and extinction coefficient of molybdenum [111] are plotted in Figure 3.9 as well. The results show that the simulation matches closely with the theoretical calculation. Simulations with periodic microstructures will be presented in chapter 5.

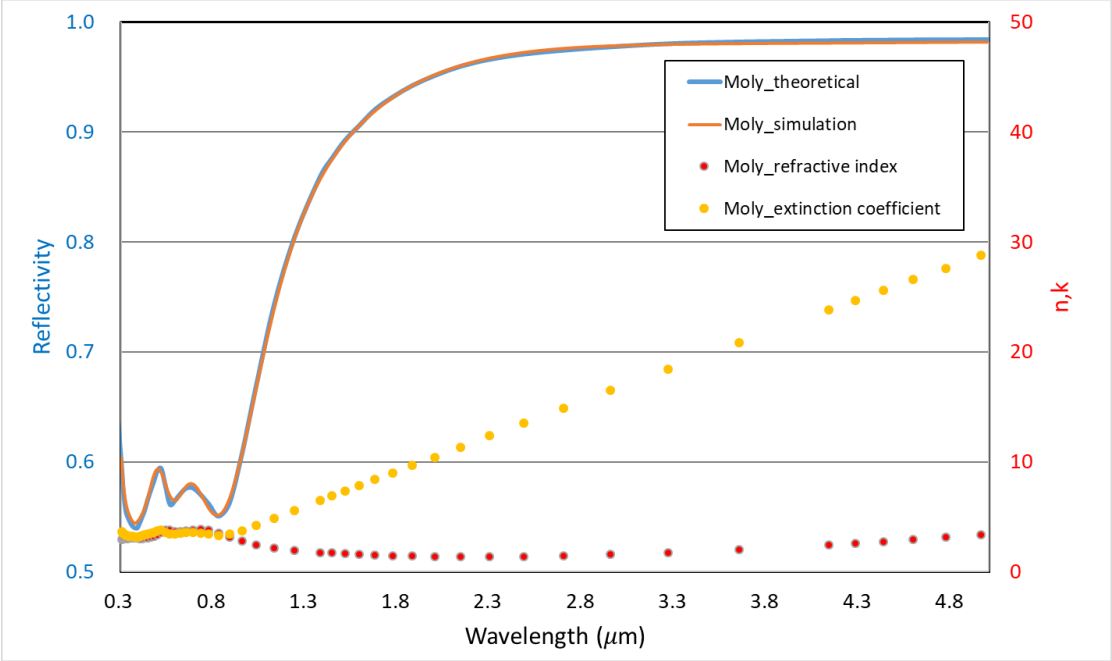

Figure 3.9 Left axis: Theoretical and simulated reflectivity of molybdenum in the wavelength range of 0.3 to 5.0 μm; Right axis: Values of the real (n) and imaginary part (k) of the refractive index of molybdenum.

3.3. Chapter Conclusion

This chapter has presented two simulation methods, COMSOL Multiphysics and Lumerical FDTD. Based on FEM, COMSOL Multiphysics will be used in Chapter 5 and 6 to simulate the sample heated up under different conditions and analyse the

thermal losses to optimise the design of thermionic converter. The optical properties of micro-patterned molybdenum will be modelled using Lumerical FDTD in Chapter 4. The optical measurements will be shown in Chapter 4 to verify the simulation results. Chapter 4 will also introduce the various fabrication methods to create selective surfaces.

4. Fabrication and Characterisation

Many techniques can be used to fabricate selective absorbers. However, the choice of different techniques will produce major differences in terms of surface structure, optical properties, thermal stability, speed of manufacture and cost. These techniques include Focused Ion Beam lithography [112, 113], nanoimprinting [114, 115], displacement Talbot lithography [116] and laser etching. The most important point is that low cost methods are needed in commercial applications. This chapter will look in detail at the Laser etching technique, which was used to etch the molybdenum microstructures that were used in this thesis. The second part of this chapter will show the optical simulation results using Lumerical FDTD. Then we will optically characterise the molybdenum microstructures by measuring the reflectance and emissivity of the samples.

4.1. Laser Etching

Research on laser-material interaction has been carried out since the first ruby laser was

introduced in 1960 [117]. After years of development, in order to meet different needs, various lasers have emerged and have been widely used in industrial processing and medical fields [118]. Laser micromachining is a processing technology that uses laser beams to cut, weld, punch and etch materials. It can be used for many materials such as metal, silicon, polymer and ceramics. Different wavelengths, pulse duration and repetition rates are offered by this technique. Thus it can achieve very fine structures in the micrometre range on the material surface [119]. Laser micromachining can be implemented with two main methods, direct laser writing (DLW) and the mask projection technique (MP) [120]. Figure 4.1 displays the schematics of both DLW and MP. As displayed in Figure 4.1(a), DLW uses a galvanometer scan head to guide the incident solid state laser and focus on the material surface. The laser light heats, melts and vaporises the material and DLW is generally used for hard or low-sensitivity materials [119]. For high-sensitivity materials, Excimer lasers are often used with MP as shown in Figure 4.1(b). It transfers the information on the mask to the target sample using shorter wavelength lasers [121].

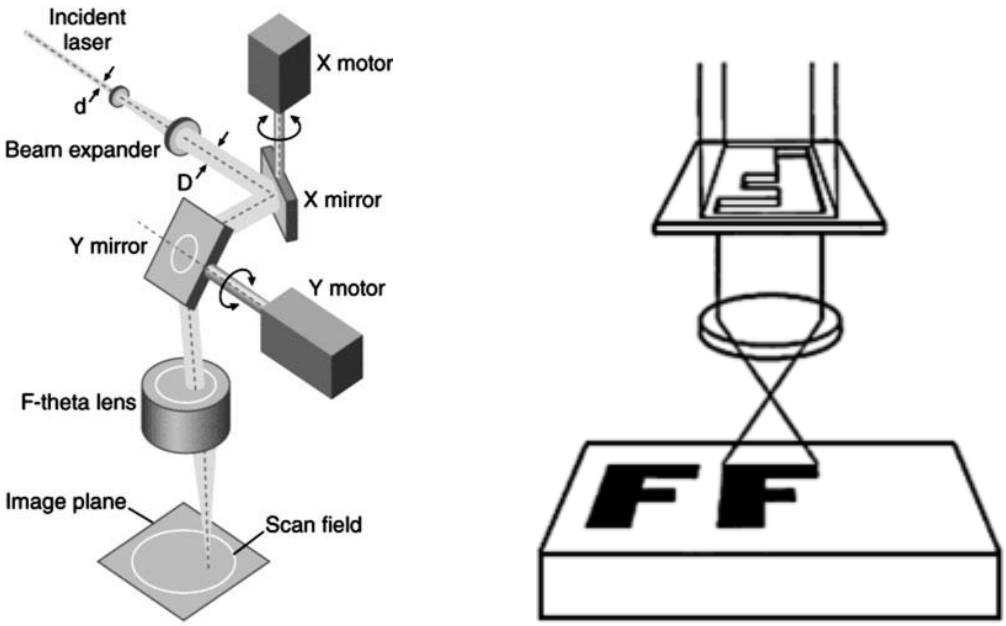

(a) *(b)*

Figure 4.1 Schematics of laser micromachining, (a) direct laser writing; (b) mask projection technique [119]

Laser micromachining can overcome some disadvantages of other processing technologies. It can be used in nearly all materials and the non-contact processing offers no mechanical stress on the material. The initial cost and maintenance cost are considerably lower compared to other surface treatment techniques such as displacement Talbot lithography. It is also low-cost for small batch production. On the other hand, laser micromachining has the limitations that it cannot offer nanometre scale processing and the production rate is low which is not suitable for large scale production.

4.2. Fabrication of 2D Micro-patterned Molybdenum using Laser Etching Technique

The fabrication work has been done by Dr. Sara Nunez-Sanchez. Samples were fabricated using commercial industrial molybdenum foil supplied by Goodfellow Cambridge Ltd. The foil has the thickness of 0.25 μm with annealing treatment. In order to maintain a flat surface, the samples were firstly laser cut into 1 cm × 1 cm squares (1 kHz, 456 μJ/pulse, speed 1 mm/s, 300 passes per line). We used a nanosecond pulsed Nd:YAG laser (ALPHA 532-XYZ-A-U system, Oxford Lasers) which operates at 532nm wavelength. Nine samples have been produced in 1cm × 1cm areas maintaining the patterning across the whole surface and allowing heating measurements under illumination. The samples have 2D disordered periodic surface structuring with different average periods (10, 20 and 30 μm). The period is disordered due the nature of the laser pulsing and movement. The surfaces were made by single pulse laser firing at different laser energies (20% =28.6 μJ/pulse, 30% =38.3 μJ/pulse, 40% = 48.1 μJ/pulse) and Table 4.1 summarises the different samples. Each laser pulse ablates a certain amount molybdenum depending on the laser pulse energy, therefore the morphology of the holes depends on the pulse energy. As the energy per pulse increases the diameter and depth of laser ablated hole increases. The holes obtained at 48.1 μJ/pulse (largest energy used) have a diameter around 20 μm (see Figure 4.2). The average period is controlled by the laser firing distance (see Figure 4.3).

Table 4.1 Laser pulse period and laser energy used for 9 molybdenum samples

Sample Number	Pattern period [μm]	Laser energy [μJ/pulse]	Laser energy Percentage
1	10	28.6	20%
2	20	28.6	20%
3	30	28.6	20%
4	10	38.3	30%
5	20	38.3	30%
6	30	38.3	30%
7	10	48.1	40%
8	20	48.1	40%
9	30	48.1	40%

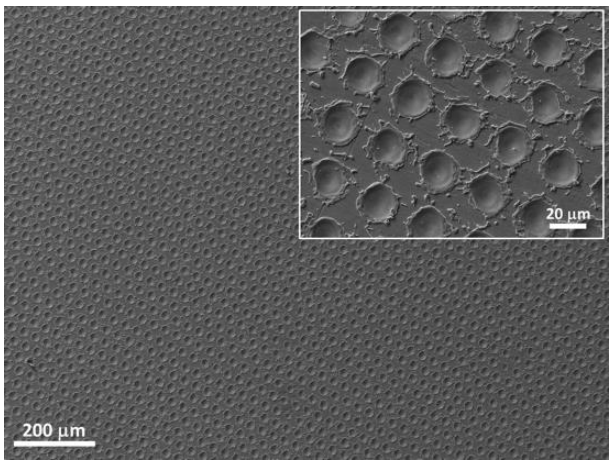

Figure 4.2 SEM image of a laser patterned molybdenum sample produced at 20% laser power and 30μm period

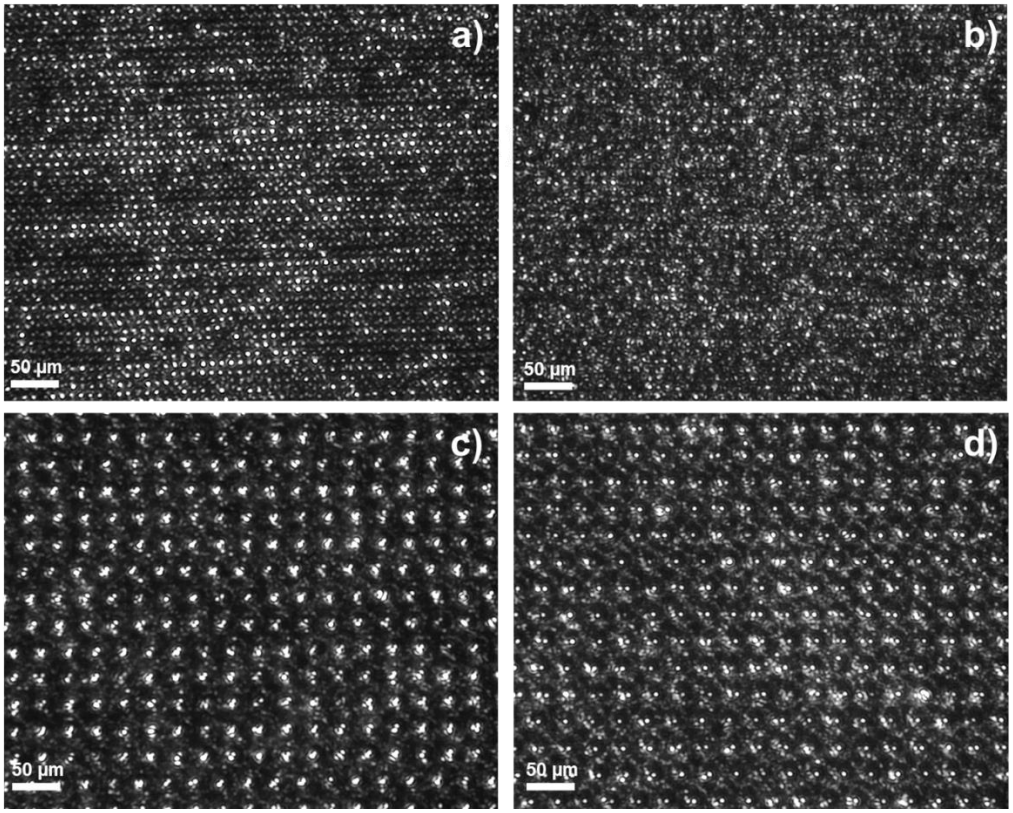

Figure 4.3 Optical microscope images of the laser micro-patterned molybdenum surfaces at: a) 28.6 µJ/pulse and b) 48.1 µJ/pulse with a laser firing distance of 10µm, c) 38.3 µJ/pulse and d) 48.1 µJ/pulse with a laser firing distance of 30 µm

4.3. Optical Simulation

FDTD reflectivity simulations have been done with Lumerical software with a planar light source and with and without periodic Bloch boundaries. Figure 4.4 shows the simulated periodic structure of molybdenum. Holes have been simulated as a trapezoids and molybdenum optical properties are plotted in Figure 3.9. As shown in Figure 4.5, patterned surfaces show larger values of absorptivity in the VIS-NIR wavelength range than flat molybdenum layer. Due to the period being much longer than the wavelength

(solar spectrum) no differences between periodic and non-periodic boundaries have been observed revealing that the dominant parameter in the reflectivity response for large holes is mainly related with hole shape and size.

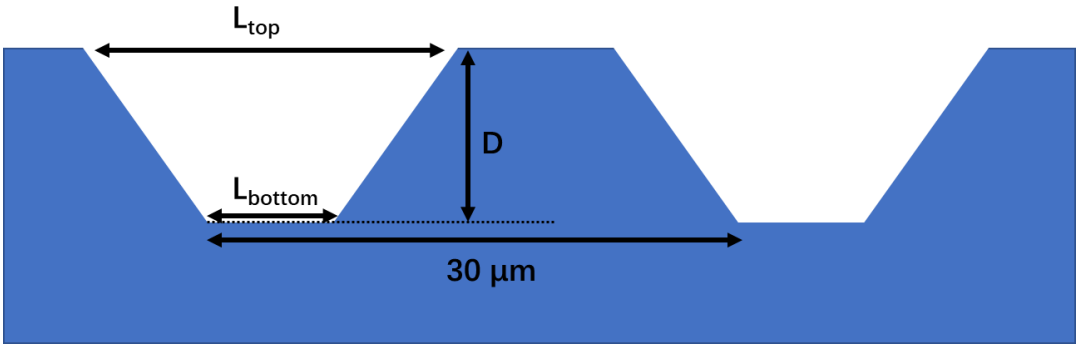

Figure 4.4 Simulated molybdenum periodic structure with trapezoidal holes

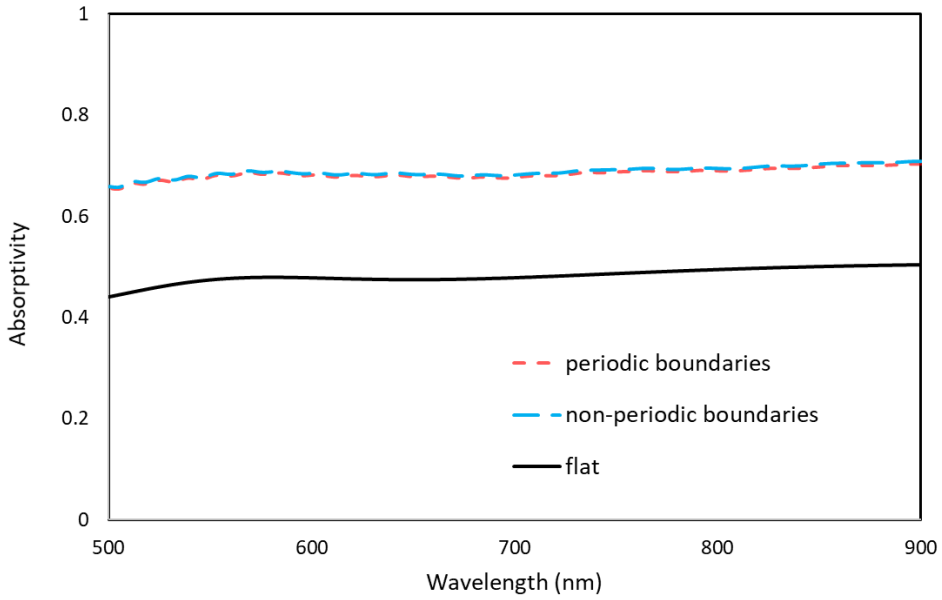

Figure 4.5 Absorptivity obtained from simulations of a flat molybdenum and a periodic and non-periodic molybdenum structure with large trapezoidal holes, where L_{top}=20 µm, L_{bottom}=5 µm and D=10 µm.

Figure 4.6 (a) shows simulated absorptivity of molybdenum periodic structures with different sized holes. We can see that deeper and larger holes result larger absorptivity of the molybdenum surfaces. As shown in Figure 4.6 (b-d), at maximum of the peak of solar spectrum (500 nm) the light is concentrated within the hole increasing the reflections at the molybdenum interfaces within the hole volume. Therefore, an increase of the temperature is expected due to the interaction of light with the walls of the hole.

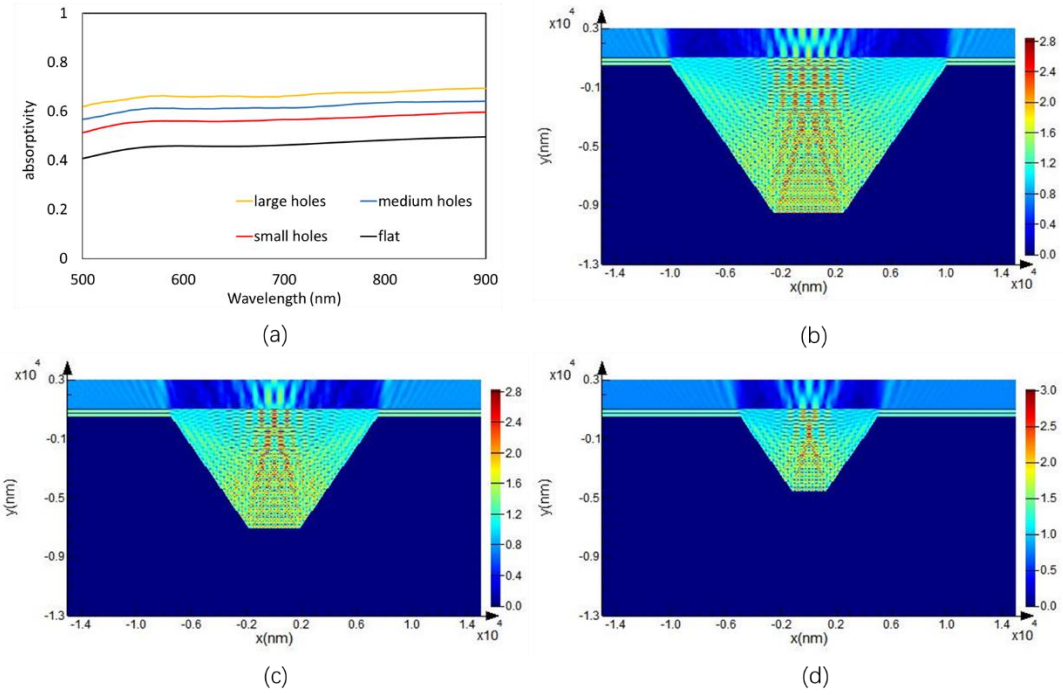

Figure 4.6 (a) Simulated absorptivity of molybdenum periodic structures with 3 different sized holes and a flat molybdenum; (b) Electric field distribution inside the large hole (L_{top}=20 µm, L_{bottom}=5 µm and D=10 µm) at 500 nm wavelength; (c) Electric field distribution inside the medium hole (L_{top}=15 µm, L_{bottom}=3.75 µm and D=7.5 µm) at 500 nm wavelength; (d) Electric field distribution inside the small hole (L_{top}=10 µm, L_{bottom}=2.5 µm and D=5 µm) at 500 nm wavelength;

4.4. Optical Characterisation of Microstructures

To characterise the microstructures of the molybdenum samples, it is important to measure the reflectance in the VIS-NIR wavelength range and the emissivity in the longer wavelength range. In this section, we will show optical measurement results of the molybdenum samples with an integrating sphere and IR microscope.

4.4.1. Integrating Sphere

An integrating sphere was used to measure the reflectance of the samples. Ulbricht implemented the integrating sphere the first time in 1900 [122]. As shown in Figure 4.7, the integrating sphere is a hollow spherical cavity with diffuse reflective coating on the inner wall. The highly reflective coating ensures that the light entering the integrating sphere is absorbed by the wall as little as possible during repeated reflections. There are three ports on the wall of the integrating sphere. The light source illuminates directly onto the test sample. Light reflected by the test sample and the interior wall of the integrating sphere is eventually collected by the detector. The detector can be connected to a measurement device such as a spectrometer.

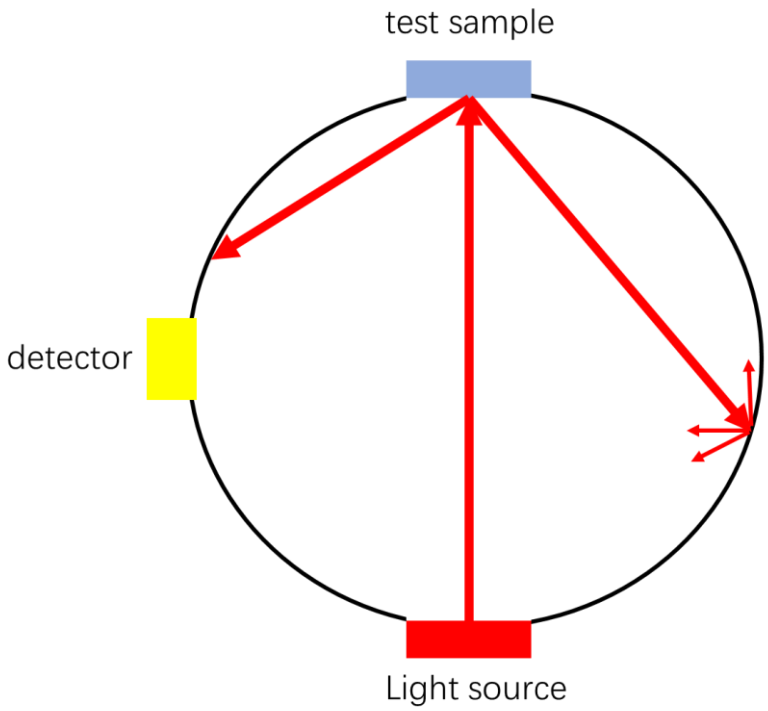

Figure 4.7 Schematic diagram of integrating sphere

Figure 4.8 shows the integrating sphere (Ocean Optics ISP-REF) and spectrometer (Ocean Optics USB2000+) setup for reflectance measurement. An optical fibre was used to connect these two devices. The integrating sphere was set to include both specular and diffuse reflections. To begin with the measurement, a high specular mirror (Ocean Optics STAN-SSH) was measured as a reflectance standard. Then the target sample replaces the reference mirror for measuring.

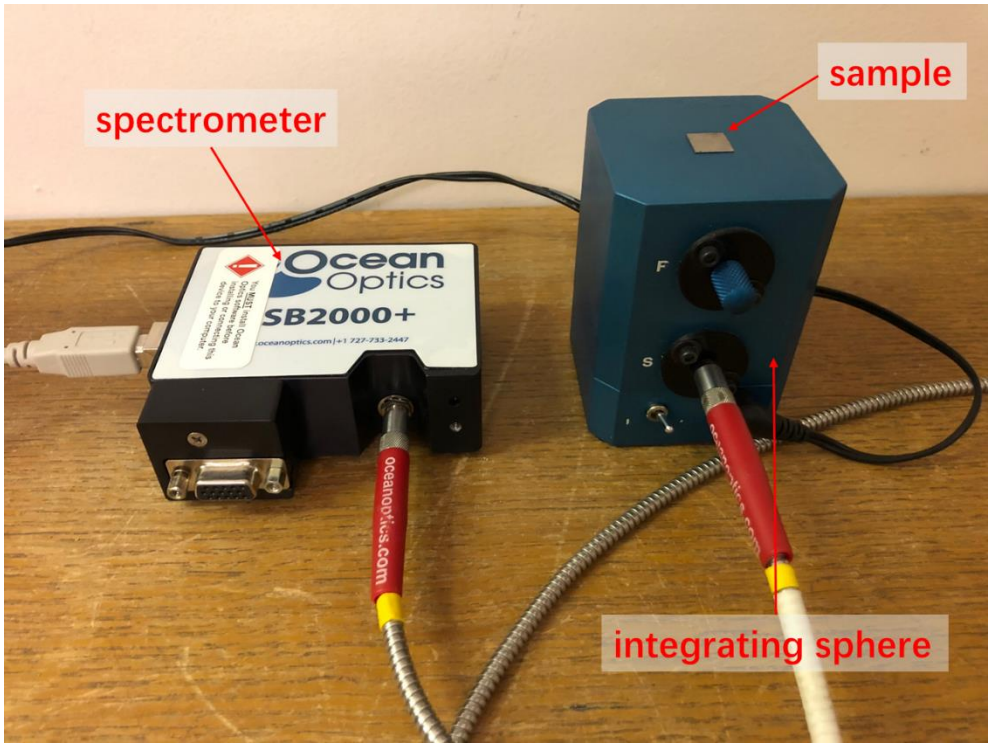

Figure 4.8 An integrating sphere and a spectrometer setup for measuring the reflectance of the samples

4.4.2. Reflectance Measurements

The reflectance of 9 micro-patterned molybdenum samples and one flat molybdenum sample were measured with the integrating sphere setup. The wavelength range is 400 to 1000 nm. The results are shown in Figure 4.9. We can see that all samples have much lower reflectance in the range of 500 to 900 nm than in the range of 400 to 500 nm and 900 to 1000 nm. Hence more obvious differences can be observed in the range of 500 to 900 nm. From Figure 4.9 (a)-(c), while keeping the laser energy the same, the reflectance of the samples increases when the period of the micro structure is reduced from 30 μm to 10 μm. From Figure 4.9 (d)-(f), the reflectance of the samples decreases

when the laser energy is increased from 20% to 40% and the period of the micro structure keeps the same. As mentioned previously in Chapter 2, the monochromatic absorptivity equals to one minus the monochromatic reflectance. Therefore, Figure 4.10 summaries all absorptivity of the samples at 500 nm. We can see that the absorptivity of the samples with 30 μm period microstructures are in the range of 0.58-0.74 and the absorptivity of the flat molybdenum is 0.43. Previously we showed the simulated absorptivity of the flat molybdenum and 30 μm period micropatterned molybdenum in Figure 4.5. It shows good agreement between the simulated and measurement results where the simulated absorptivity of the flat molybdenum and 30 μm period micropatterned molybdenum are 0.44 and 0.65 respectively.

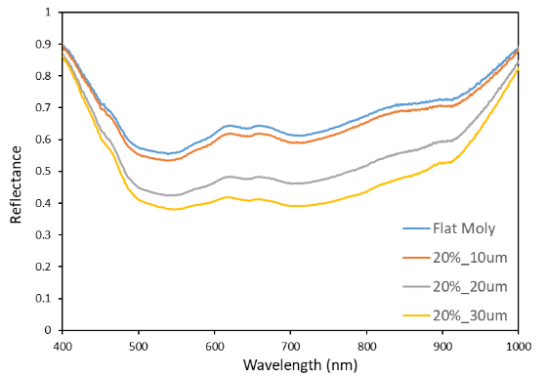

(a)

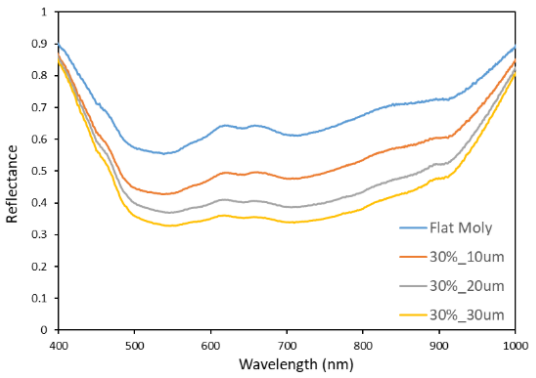

(b)

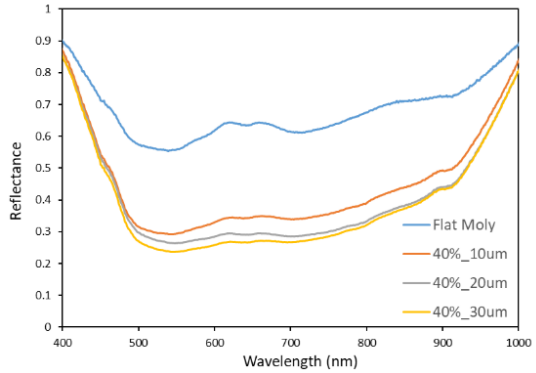

(c)

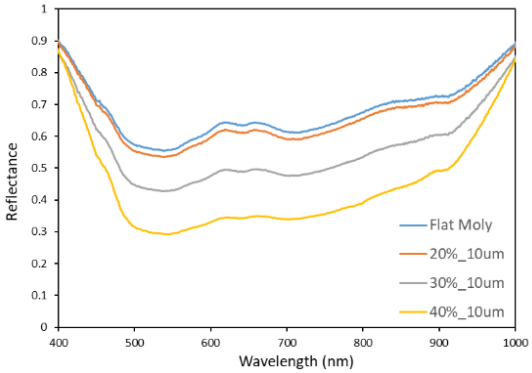

(d)

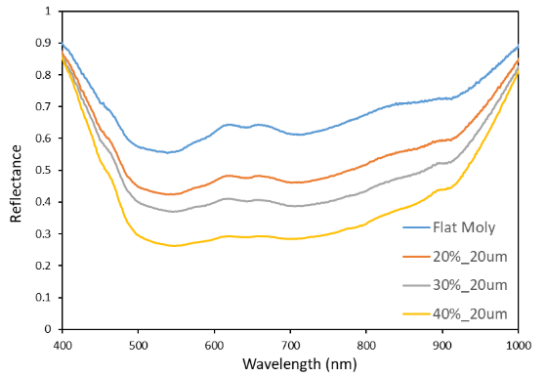

(e)

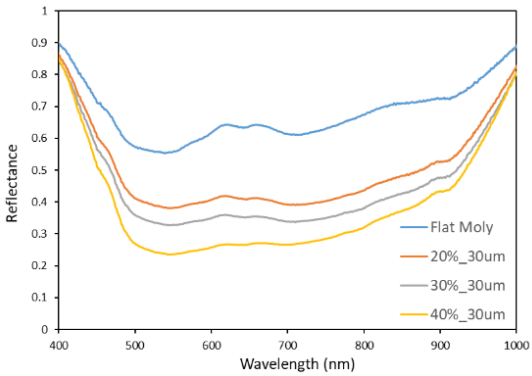

(f)

Figure 4.9 Reflectance measurements with the integrating sphere. (a)-(c): Reflectance of the samples dependence on period. (d)-(f): Reflectance of the samples dependence on laser energy.

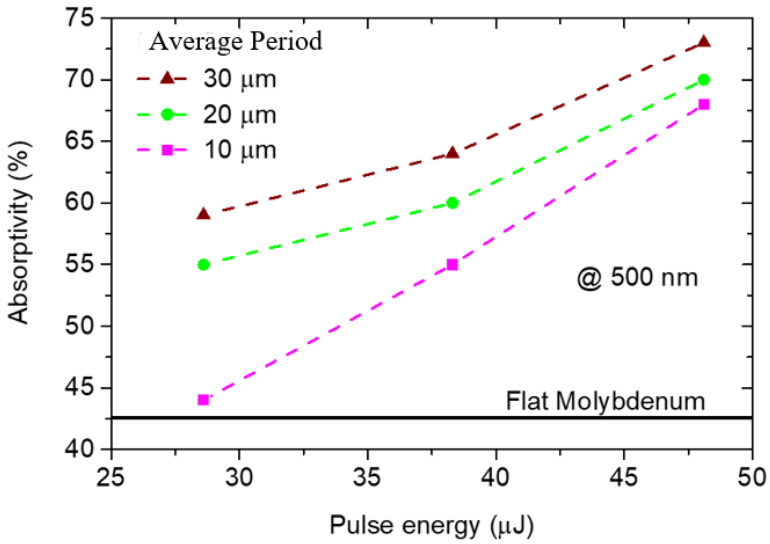

Figure 4.10 Absorptivity at 500 nm (wavelength at maximum of solar spectrum) for all samples as a function of the pulse energy and the average periods.

4.4.3. Emissivity Measurements

The absorptivity measurement results of the molybdenum samples over 400-1000 nm range has been shown in the previous section. It is also important to investigate the optical behaviour of these samples at longer wavelengths (1.5 μm to 10 μm). Hence the total emissivity of three samples in the 2.5-5.5 μm range were measured using an infrared (IR) microscope. These measurements were done with the help from Dr. Andrei Sarua. As shown in Figure 4.11, the sample was placed on a Peltier heater and can be heated up to 100℃. The IR microscope firstly took a radiance image at room temperature. Then the sample was slowly heated to 75℃ and another radiance image was recorded. The system then created an emissivity map of the sample and the average emissivity can be calculated.

Figure 4.11 Emissivity measurement setup including an IR microscope and a Peltier heater

Figure 4.12 shows the emissivity measurement results of 3 molybdenum samples (sample 1, 5 and 6). The emissivity of the unpatterned surfaces of 3 molybdenum samples were ~0.155 consistently. The patterned surface of sample 6 has the highest emissivity of 0.35 and sample 1 has the lower emissivity of 0.22. This strongly indicates that the micro-patterning process also increases the emissivity at longer wavelength while increasing the absorptivity at 400-1000 nm. It also shows a similar pattern of results that larger and deeper holes on the sample surface increases the emissivity. The

measured emissivity of the patterned and unpatterned samples will be used in COMSOL thermal modelling in Chapter 6.

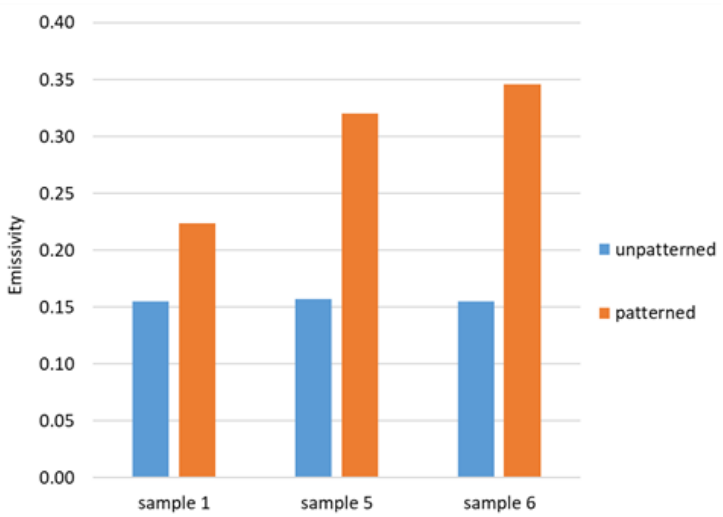

Figure 4.12 Emissivity measurement results for both sides of 3 molybdenum samples at 75℃

4.5. Chapter Conclusion

This chapter presented the fabrication and characterisation methods for this thesis. The 2D patterned molybdenum has been fabricated using laser etching technique. Optical simulation showed that the microstructures improved the absorptivity of the molybdenum in the VIS-NIR. Integrating sphere has been used to characterise the absorptivity of the samples. IR microscope has also been used to measure the emissivity of the samples. In the following chapter, we will investigate using these molybdenum samples as a solar absorber and present the results of the heating measurements.

5. In air and vacuum light heating experiment

In the previous chapter, we showed the optical characteristics of the 2D patterned molybdenum. This chapter will show various light heating experiments on these molybdenum samples. We begin by showing in-air measured results followed by in-vacuum results with a solar simulator. The measured results are compared with COMSOL simulated results and we also investigate the possible solutions to further minimise thermal loss which will be discussed in Chapter 6.

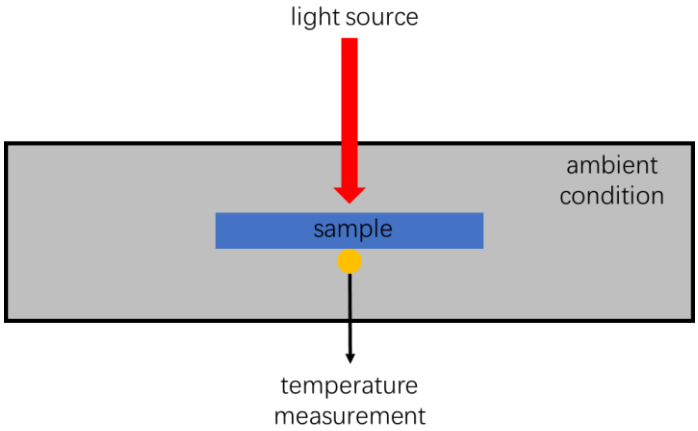

Figure 5.1 Schematic diagram of general light heating experiment

As shown in Figure 5.1, there are three main variables in the light heating experiments: light source, ambient condition and temperature measurement. Depending on the application and target temperature, different light sources can be used in the experiment. This includes the power density distribution, wavelength range and incident angle, etc.

High power lasers as a heat source can be easily manipulated with reflation mirrors to heat small samples to very high temperature with low power losses [123]. In this thesis, we mainly used a solar simulator with a spherical lens to conduct heating experiments. We will also show results of solar radiation measurements which were conducted in India. The second variable of the heating experiment is the ambient condition. It includes how the sample is held in place and whether the system is in-air or vacuum. This is most critical part to this project, and we will make extensive discussions in this chapter and Chapter 6. The last variable is the temperature measurement method. Normally two types of measuring methods can be used here. One is the thermocouple which is contact based solution. Another option is the IR camera which does not require contact with the test subject. Here we use thermocouple for this project because the sample is too small to cover the output of the solar simulator and IR radiation from the source confuses the IR camera. Thus, it can have trouble reading the temperature of the sample.

5.1. 2D Patterned Molybdenum in-air heating measurements

Here we performed the in-air heating measurement for the ten molybdenum samples including nine micro-patterned ones and a flat one. Figure 5.2 shows the measurement setup. The molybdenum sample was held on two pieces of glass using tape. The glass acted as thermal insulator and only two corners of the sample contacting with them. A K-type thermocouple was attached to the back side of the sample. The probe of the

thermocouple is made of stainless steel and has a diameter of 12 mm. The light source was a 150 W Newport 6255 Xenon arc lamp which was operated at 100W. The output of the lamp had a wavelength range of 200-2400 nm. The spectral irradiance curve of the lamp is shown in Appendix 9.1 [106]. The lamp was in a Newport 67005 arc lamp housing. It produced 33 mm diameter collimated beam from its output flange. In order to increase the light intensity on the sample, a spherical lens was placed between the solar simulator and the sample. Therefore, the diameter of the focused light spot on the sample was ~3 mm. The thermocouple was connected to a Pico TC-08 thermocouple data logger which recorded the temperature over time on the laptop.

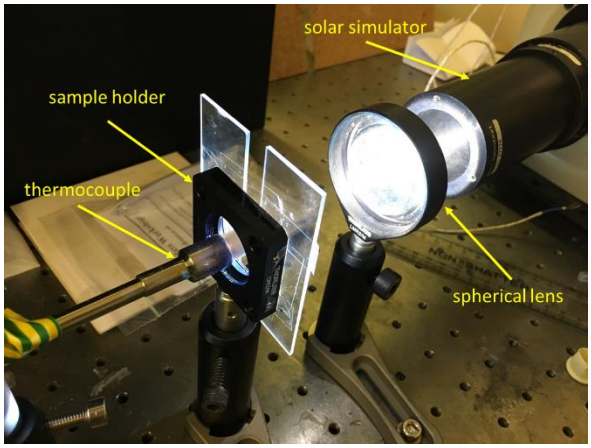

(a)

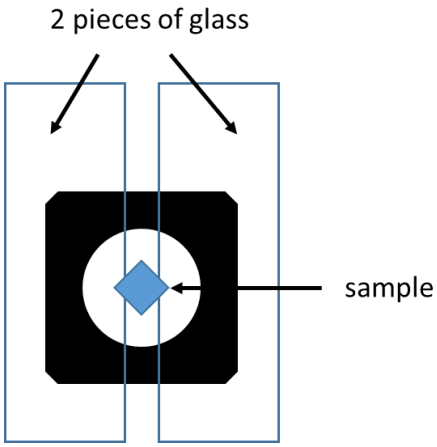

(b)

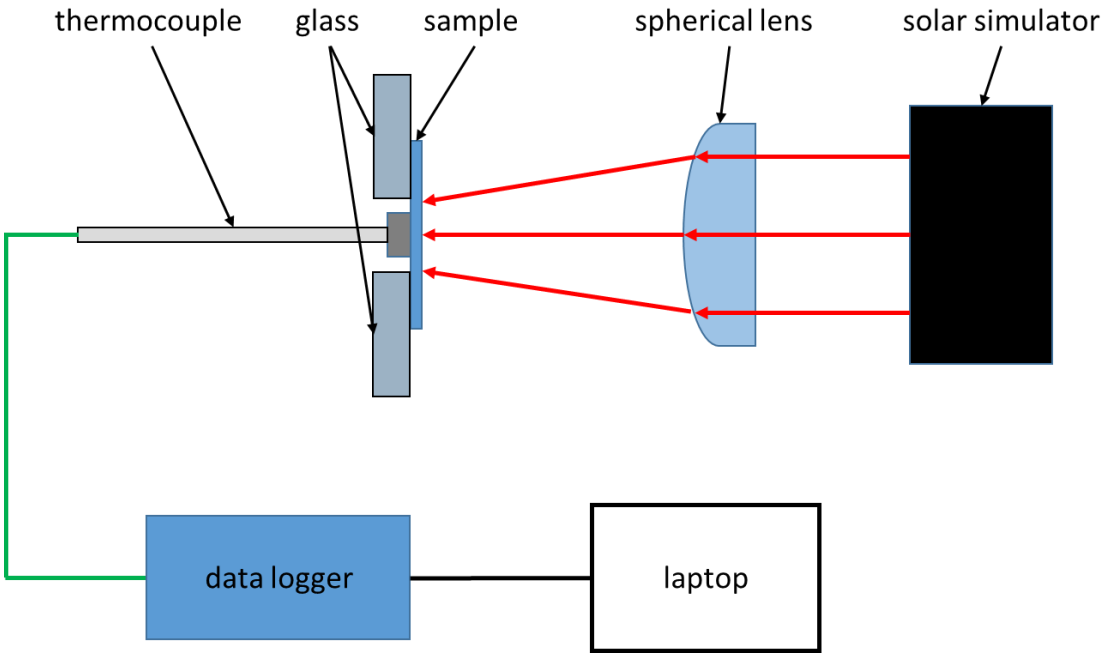

(c)

Figure 5.2 Measurement setup for molybdenum samples in air thermal test, (a) a picture of the setup; (b) schematic diagram shows how sample is mounted on the glasses; (c) top view schematic diagram

Figure 5.3 shows the highest temperatures achieved by one flat molybdenum and nine micro patterned molybdenum samples under 500s solar simulator illumination. We can see that the flat molybdenum reached the lowest temperature of 92℃. Furthermore, the higher laser energy and larger period molybdenum samples reached higher temperature. This agreed with the absorptance measurement results showed in Figure 4.10 in Chapter 4. As previously discussed, the power input, the ambient condition and the temperature measurement methods were the same for all samples. Therefore, the conduction and convection loss could be considered the same because the temperatures were relatively low and similar. The major impacts on the temperature difference were absorption and thermal emission. Although the emissivity of the samples also increases with the sample period and laser energy increases, the thermal emission seemed to play a lesser than the absorption.

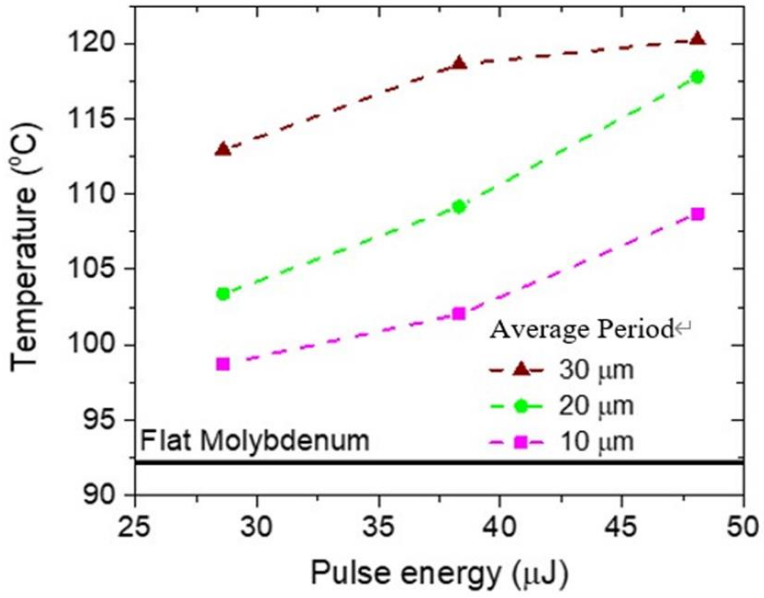

Figure 5.3 The highest temperatures achieved of ten samples over 500s solar simulator illumination. Triangles, circles and squares represent 30μm,20μm and 10μm average period of the sample microstructure; x-axis represents the laser energies used to produce the samples

5.2. 2D Patterned Molybdenum in-vacuum results in India

In chapter 3, we showed that thermal conduction and convection loss have significant impact on the sample temperature from Figure 3.5. In order to reduce the conduction loss and eliminate the convection loss, we designed a vacuum device for the temperature experiment as shown in Figure 5.4. The device consists of three Conflat (CF) flanges: one blank flange as the base, one bored flange in the middle with four drilled holes for passthrough ports and another bored flange with glass window on the top. The four passthrough ports also used smaller CF flanges. Here two ports are used

to install thermocouple connectors. One is occupied by the pump valve and the last one is blank but can be used for electric connections of the thermionic convertor in the future. Copper gaskets were seated between each flange and the bolts and nuts were tightened to 15 lbf· ft to achieve a high vacuum seal.

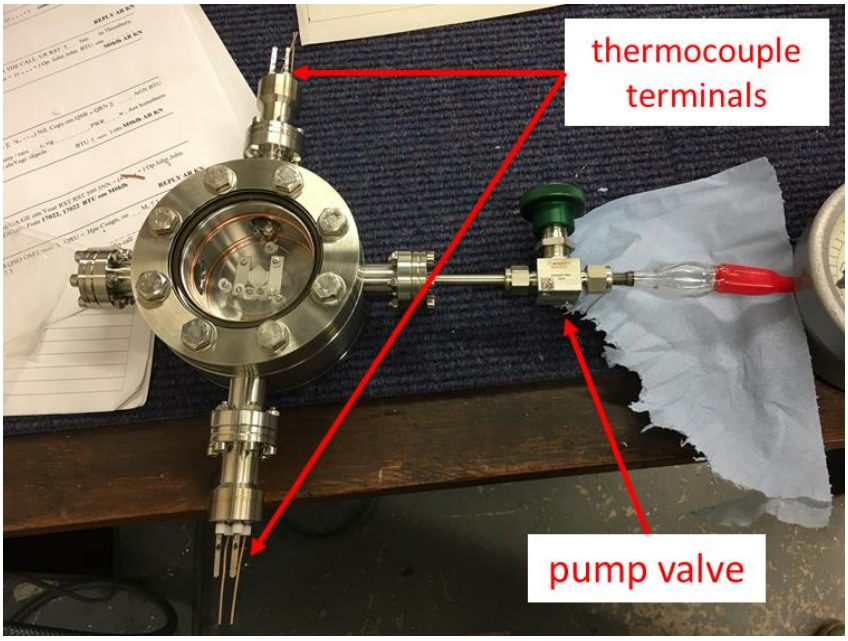

Figure 5.4 Vacuum device for temperature experiment

Figure 5.5 shows a closer look inside the vacuum device. Three long rods support a 1mm thick round sample holder made of quartz. We used quartz due to its low thermal conductivity (1.4 W/(m·K) at 293 K) [124]. Therefore, it could act as a good thermal insulator. It is also low-cost and easy to machine. There is a hole in the centre of the quartz holder and a recess for the square sample. The sample was held down by two tungsten bars with screws. Another small piece of quartz was used to hold down the thermocouple for the sample. There were two thin wire K-type thermocouples used in

the vacuum device. One was touching the top surface of the sample which measured the sample temperature. Another was wired on one of the mounting screws on a tungsten bar which measured the holder temperature.

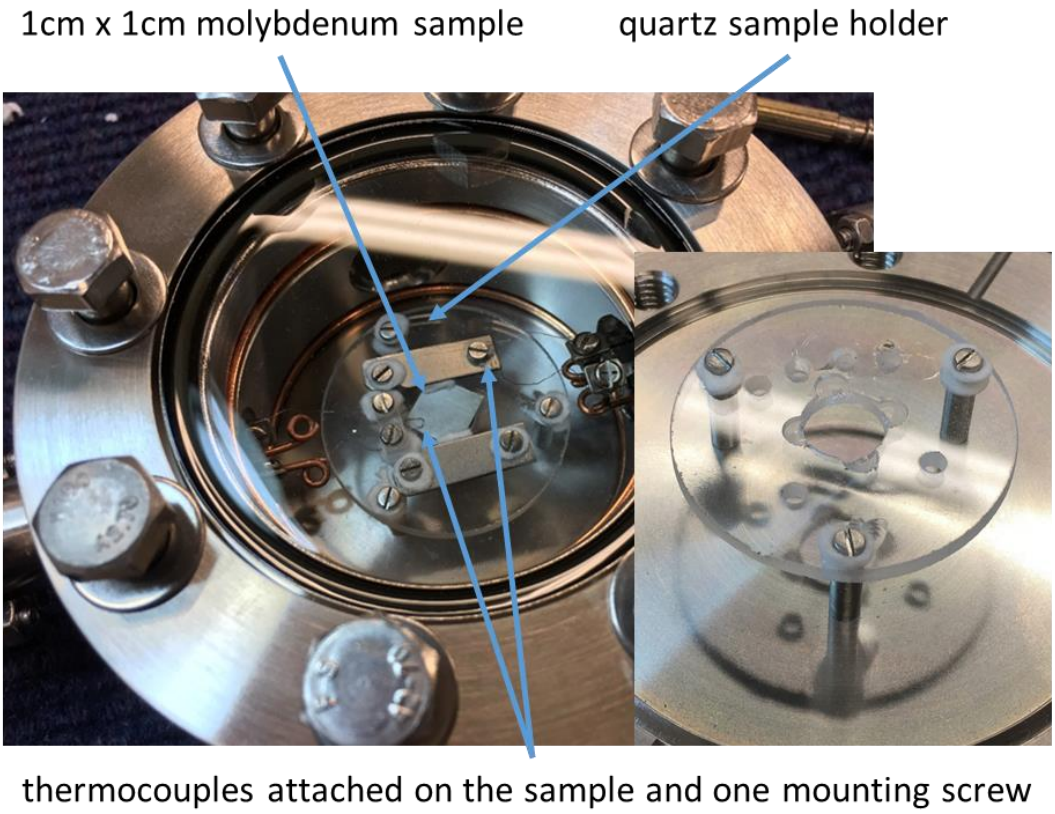

Figure 5.5 The internal design of the vacuum device, the inserted picture shows the quartz holder

As shown in Figure 5.6 (a), the vacuum device was firstly tested in air without pumping it into vacuum. Sample 9 was used due to its best absorption shown in previous measurement. The same light source with a spherical lens was used in this experiment. Figure 5.6 (b) shows the measured temperature rises of the sample and the sample

holder. We can see that the temperature of the sample achieved 98℃ after 500s illumination. This result was lower than the previous measurement of 120℃ in Figure 5.3. We believe that it caused by two reasons. The sample absorbed less power due to light going through the glass window and the change of the mounting mechanism increased the contacting area between the sample and the sample holder. The temperature of the holder was below 40℃ which proved good insulation between the sample and the sample holder.

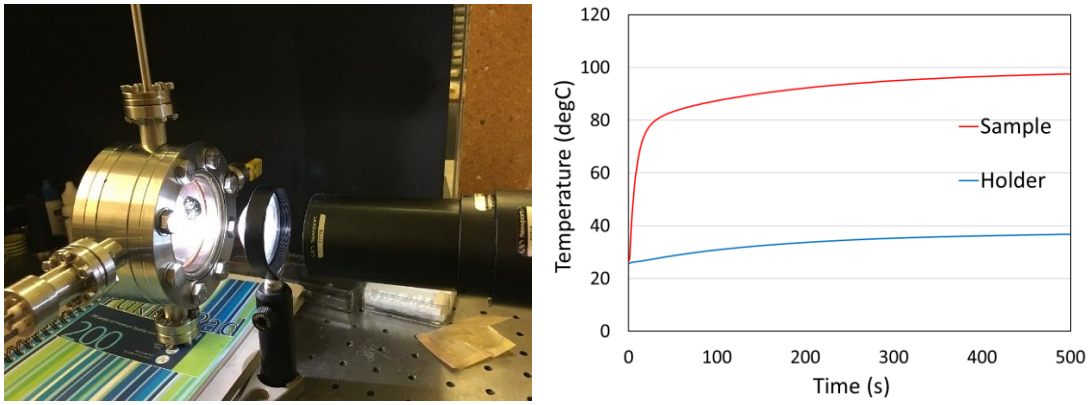

(a) *(b)*

Figure 5.6 (a) Vacuum device in air measurement setup; (b) Measured temperature rises of the molybdenum sample 9 and the sample holder over 500s illumination

As shown in Figure 5.7, the vacuum device was placed in an oven and connected to a vacuum pump. The device was heated up to 200℃ during the pump process which lasted ~12 hours. This process is called thermal degassing which removes gases in the metal so that it maintains good vacuum condition in the vacuum device when

conducting the heating measurement. The valve was closed and the glass tube was sealed after the degassing and the pump process. Then the device took ~2 hours to cool down naturally to room temperature.

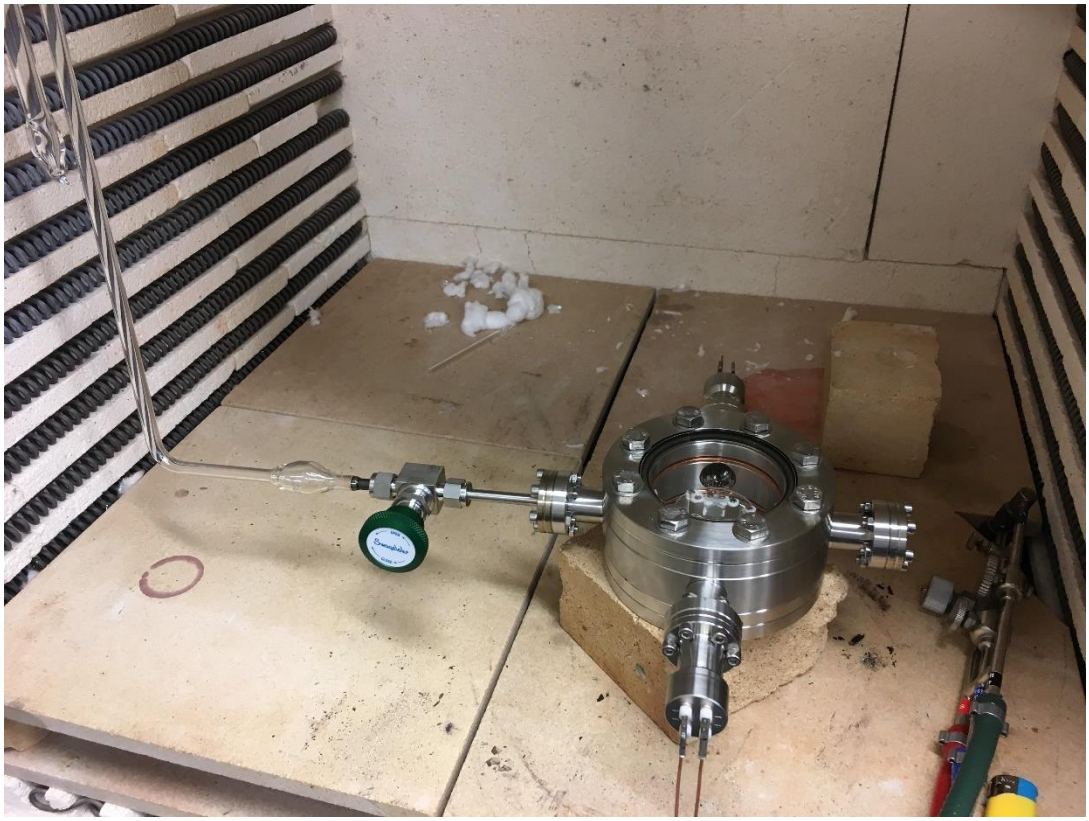

Figure 5.7 The vacuum device pumped to vacuum while heating up to 200℃ in an oven

5.2.1. Solar heating measurements using a dual axis solar tracker with Fresnel lens

The in-vacuum heating experiments were conducted in Indian Institute of Technology Madras in Chennai with the help of Premjit Singh.N and S. Lokeswaran. The first test

used a small dual axis solar tracker with a Fresnel lens as shown in Figure 5.8. The vacuum device was fixed on the tracker and the sun light was focused by the Fresnel lens onto the sample. A pyrheliometer was mounted on the side of the solar tracker which measured the Direct Normal Irradiance (DNI) over time. DNI is the solar radiation measured at the surface per unit area on the Earth perpendicular to the sun [125]. The size of the Fresnel lens is 30 cm × 30 cm and its focal length is ~40 cm. The diameter of the light spot was ~1.5 cm which covered the whole sample. The concentration ratio is ~320 if we assume the efficiency of the Fresnel lens is 0.8. The ambient temperature at the time of measurement was ~31℃.

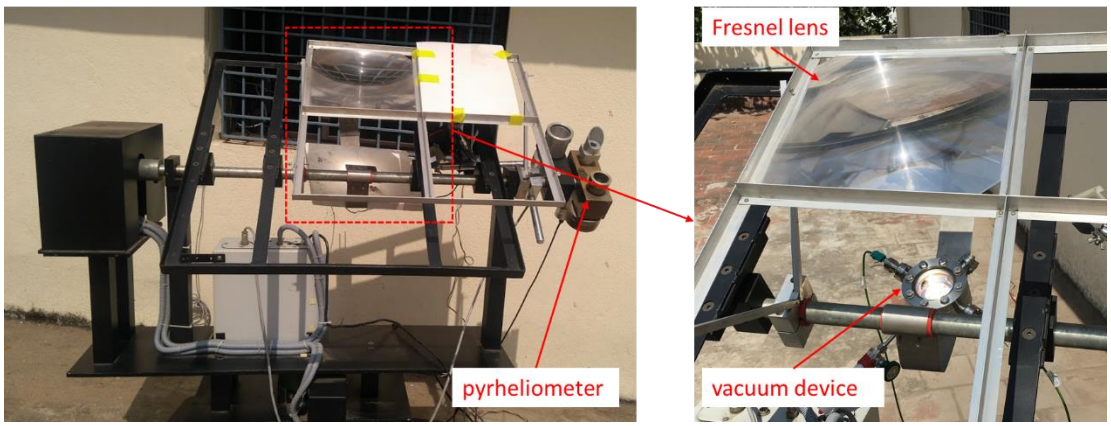

Figure 5.8 vacuum device solar heating measurement on a dual axis solar tracker

Figure 5.9 shows the temperature and DNI measurement results of solar heating using the dual axis solar tracker. The tracker was turned on at 10:39 AM and turned off at 12:16 PM. DNI started from around 520 W/m^2 in the beginning and rose to 620 W/m^2 at 12:00 PM. If we assume the solar irradiance at the time was 600 W/m^2 when the

molybdenum sample reached the highest temperature. The concentration factor can be worked out as ~192. The sample temperature rose sharply when the solar tracker was turned on and continued to rise with DNI increasing over time. The highest sample temperature achieved was 428℃ which is close to our target temperature of >500℃ for thermionic emission. This is very promising since we only used a simple Fresnel lens for solar concentration. The holder temperature increased slower than the sample temperature and stabilised at 180℃-190℃. We can see that there was ~240℃ difference between the sample and the holder, which proved good thermal insulation between them.

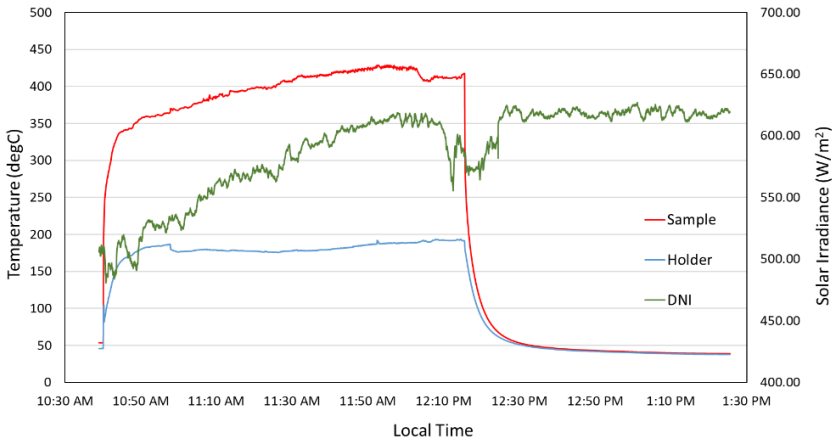

Figure 5.9 Measured temperature response of sample 9 and the holder with DNI in 2 hours and 46 minutes

5.2.2. Solar heating measurements using a parabola dish

The second experiment was conducted on a parabola dish with dual axis tracking system. As shown in Figure 5.10, the parabola dish has a square shape with nine square

reflective panels. The vacuum device was mounted on the focus area. The dish aperture area is 3.6 m × 3.6 m and the focused area is 0.4 m × 0.4 m so the concentration ratio is 81. Due to the large spot area, the entire vacuum device would expose to the solar radiation. Therefore, a heat shield was placed between the parabola dish and the vacuum device. The heat shield is made of alumina which has very high temperature resistance. It protected the vacuum device and the cables from direct exposure. There is a small hole in the centre of the heat shield for enough light illuminating the sample.

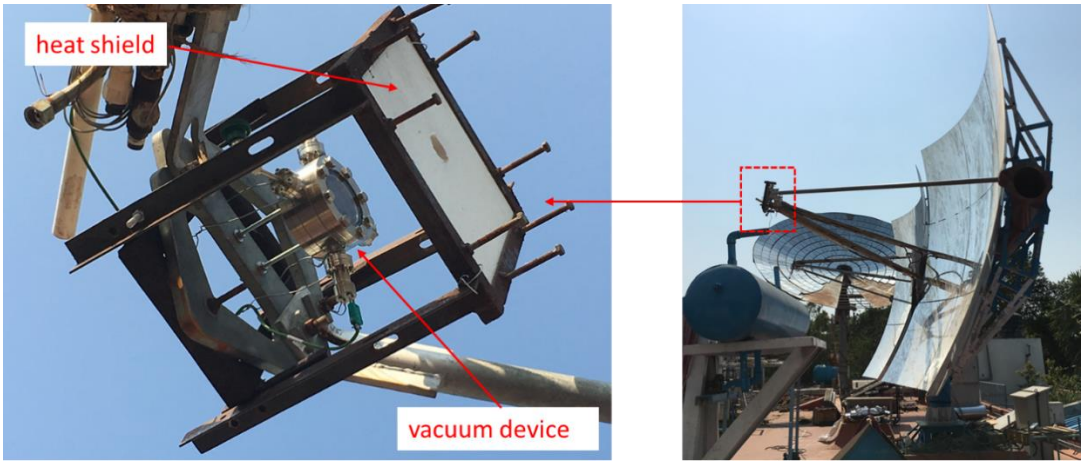

Figure 5.10 vacuum device mounted on a parabola dish

The experiment was conducted from 11:06 AM to 11:48 AM and the tracker on the parabola dish was turned on from 11:07 AM to 11:15 AM. There was no pyrheliometer on the parabola dish, so we had no DNI data. The experiment was conducted the following day from the previous small tracker experiment, and it was in the same time period of the day with same weather conditions. Therefore, we could assume the DNI was around 600 W/m^2 at the time of the experiment. Figure 5.11 shows the measured

temperatures of the sample and the holder. The highest temperature of the sample reached around 320℃ and the holder reached around 175℃. There were fluctuations in the curves due to the tracking system error of the parabola dish. The centre of focus area shifted on and off the sample regularly so that the sample received different level of irradiance. The highest temperature achieved by the parabola dish was lower than the Fresnel lens due to the concentration ratio difference between these two solar concentrators. It means that lower solar radiation was received by the sample from the parabola dish compared to the Fresnel lens. However, the parabola dish produced much larger receiver area compared to the Fresnel lens solution. The relative high temperature of 320℃ achieved by the parabola dish demonstrates the potential of large area commercialised thermionic convertors.

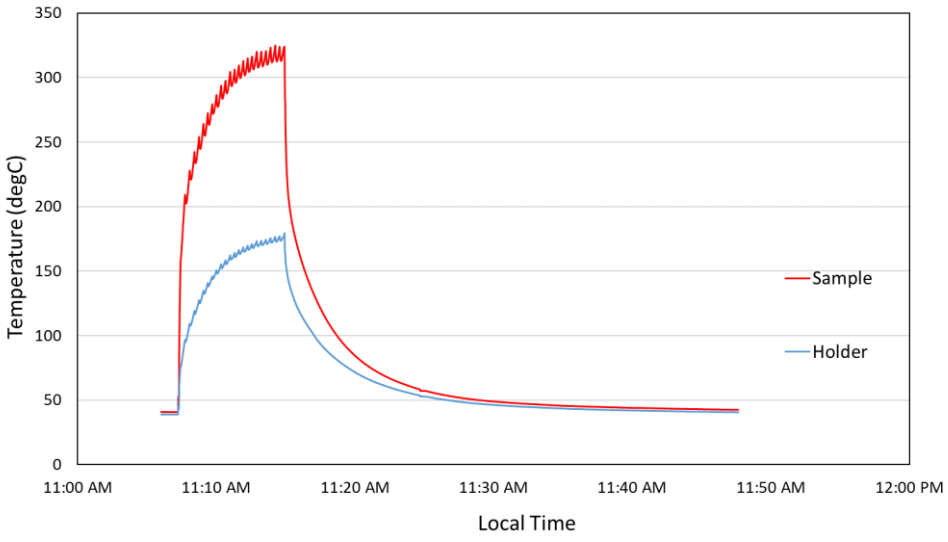

Figure 5.11 Measured temperature response of the sample and the holder in 42 minutes

5.3. 2D Patterned Molybdenum in-vacuum results using solar simulator

Due to the technical malfunctions of the parabola dish in India, the vacuum device could not be taken down for 5 months. Therefore, we designed and constructed a new vacuum device as shown in Figure 5.12 which has been used intensively for in-lab thermal testing. Compared to the previous vacuum device with a flat glass window, the new vacuum device has a glass dome attach to a CF flange. The bottom of the device has four hollow copper tube feedthroughs in a CF flange. For thermal experiments, two feedthroughs were used for thermocouple connections and one was used for the pump valve. We implemented the same mechanism for mounting the sample with a quartz holder. Three tungsten rods were soldered on the bottom flange and supported the quartz holder. A thicker K-type thermocouple was fixed on the back side of the sample and its terminals went through the copper tubes to the outside connectors. Copper gaskets were seated between each flange and the bolts and nuts were tightened to 15 lbf· ft to achieve a high vacuum seal.

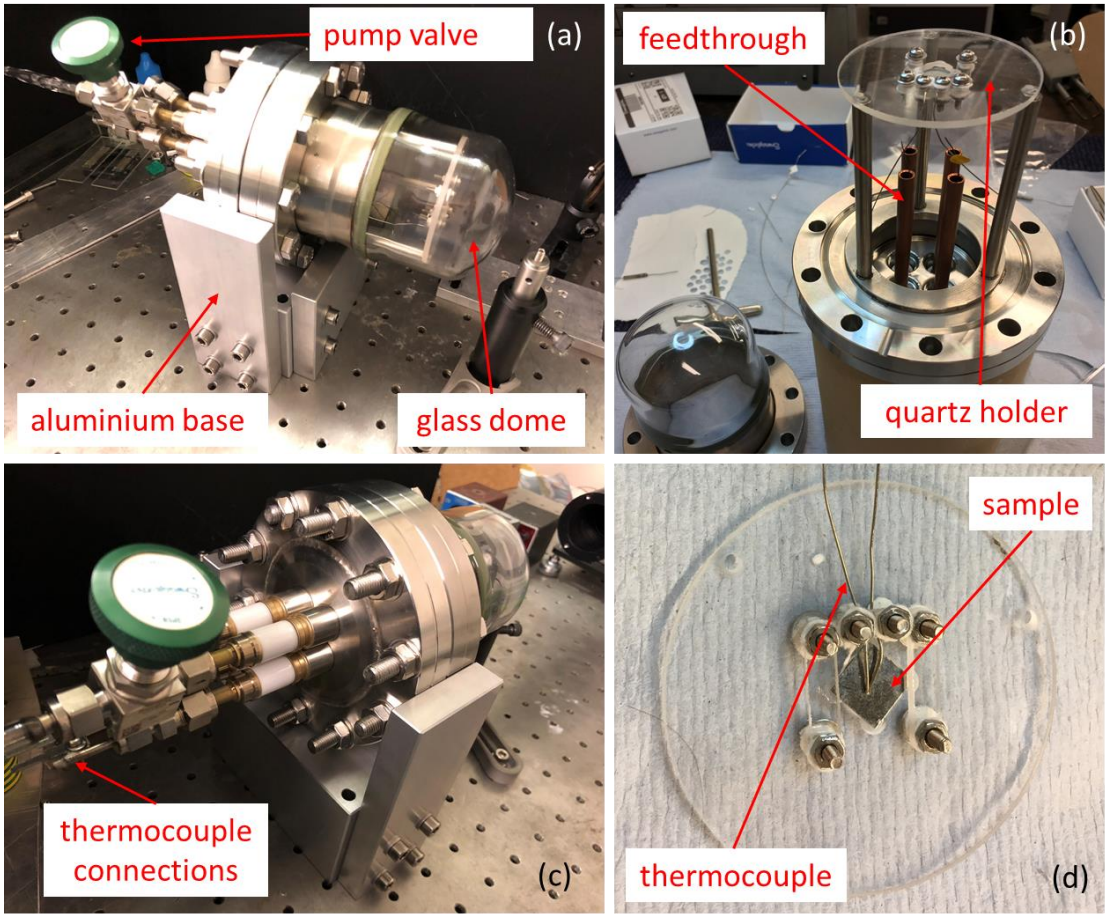

Figure 5.12 vacuum device with a glass dome, (a) front side; (b) inside; (c) back side; (d) quartz holder and sample

As shown in Figure 5.12 (a), the vacuum device seats on a base fixed on the optical table. The base consists of four aluminium blocks. This was for the purpose of keeping the device at the same place in between every test, since we were conducting multiple tests on different samples in different vacuum levels.

Prior to the experiment, we used COMSOL to model the heat transfer behaviour inside the vacuum device. Figure 5.13 (a) shows the top view of the proposed quartz holder in COMSOL simulation. The diagonal cross section diagram is shown in Figure 5.14. The

four corners of the molybdenum sample sit on the quartz holder which has a 11.8 mm diameter round cut-out. The sample is heated by the solar source which can be modelled as a Gaussian distributed heat flux shown in Figure 5.13 (b) on the top surface of the sample. The temperature monitor is at the centre of the back surface of the sample. In the experiment, the molybdenum sample and the quartz holder are placed vertically as shown in Figure 5.12 (d), the recessed area of the quartz was rough due to the machining and the molybdenum sample was not pressed firmly onto the quartz. Therefore, the sample was not contacting with the quartz holder perfectly. This can result in reduced thermal contact conductance between the molybdenum sample and the quartz which means less thermal conduction.

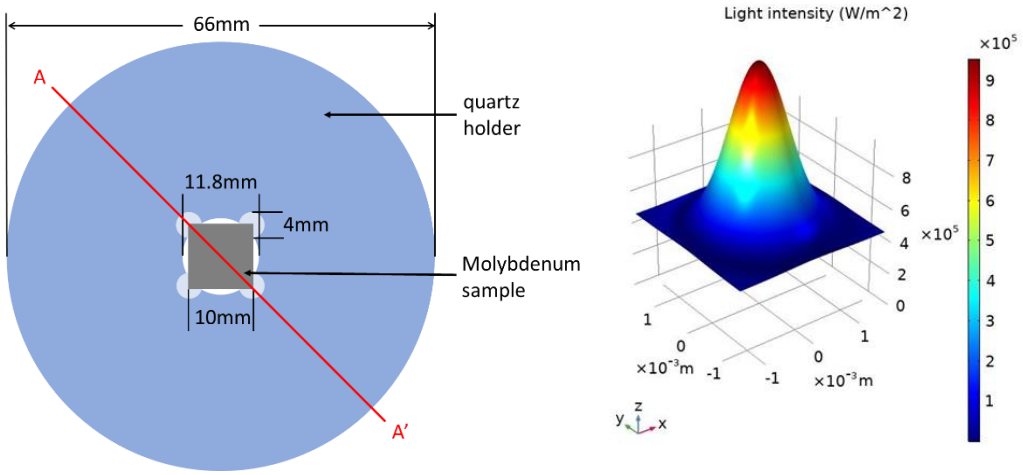

(a) *(b)*

Figure 5.13 (a) Simulated top view of the proposed sample mounting mechanism with Molybdenum sample, (b) Gaussian profile heat source applied on top of the sample

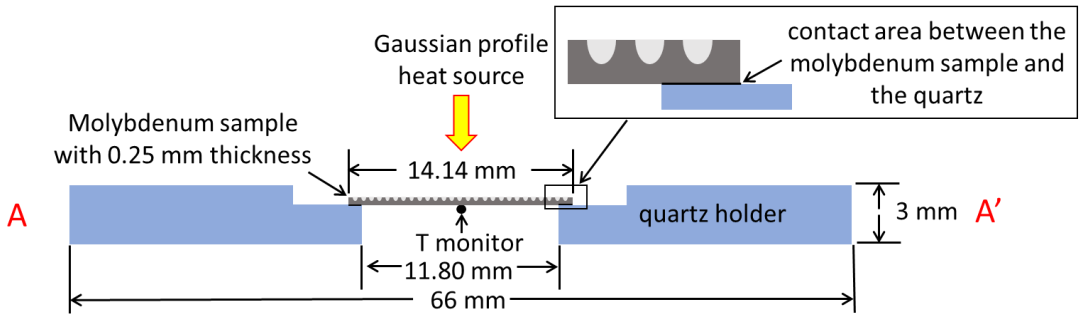

Figure 5.14 Simulated cross section diagram of the proposed sample mounting mechanism with patterned surface on top

The simulations were for two molybdenum samples in three different cases as shown in Figure 5.15. Figure 5.15 (a) flat molybdenum with unpatterned surfaces. Figure 5.15 (b) used flat-patterned and Figure 5.15 (c) patterned-flat. Because the best sample (sample 9) we have was oxidised during the experiments conducted in India, we have chosen the second best sample we have chosen the simulation parameters to match with Sample 6, they are listed in Table 5.1. The measurement heat source will be the Newport 6255 Xenon Lamp with 67005 Arc Lamp Housing. According to the manual [126], the irradiance of the lamp is across 200-2400 nm, so we divided the wavelength range into 3 sections and specified the power and the optical properties of the sample in different wavelength ranges. The solar simulator powers were calculated from the spectral irradiance of the lamp. The calculation steps are shown in Appendix 9.1. The total output of the solar simulator is 4.4 W and the total receiver area is 1 cm × 1 cm. We assume that 80% of the power is received by the sample through the lens and the glass window. Therefore, the radiant flux density on the sample is 35200 W/m^2 and the

concentration factor is 35.2. From Figure 4.10, the absorptivity of patterned surfaces of sample 6 at 500-900 nm was ~0.6 and the absorptivity of the unpatterned surface at 500-900 nm was ~0.4. For 200-500 nm and 900-2400 nm wavelength, we assume the absorptivity of both patterned and unpatterned surfaces is 0.1. The emissivity of the patterned surface and the unpatterned surface are set to 0.35 and 0.16 from our previous measurements as shown in Figure 4.12. The simulation includes six combinations: flat-flat, patterned-flat and flat-patterned in air and in vacuum. The convective heat transfer coefficients h in air for different planes are 5.4~44 W/(m^2·K) which are derived from equation 2.6-2.12. The detailed calculation of the convective heat transfer coefficient in air is shown in Appendix 9.3. In vacuum, we assume no convection occurs so h equals to 0 W/(m^2·K). The illumination time was 1000 s for both simulation and measurement which was enough for the samples to reach the highest temperature.

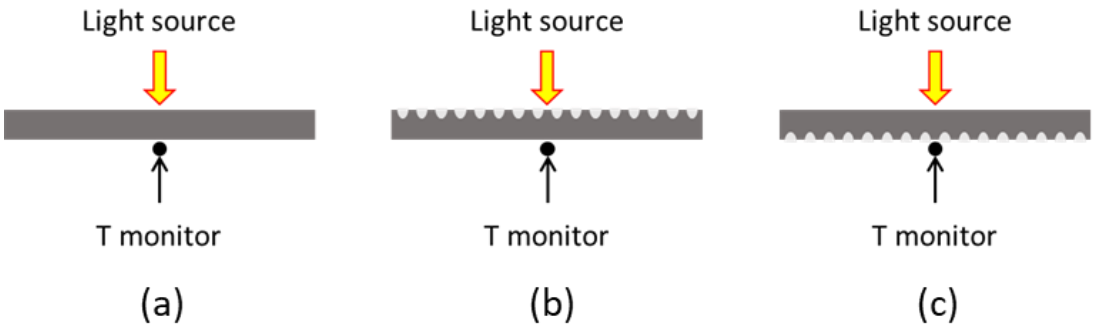

Figure 5.15 Illustrations of three cases for the temperature measurements: (a) flat-flat, (b) patterned-flat and (c) flat-patterned

Table 5.1 Parameters used in COMSOL Multiphysics simulation

wavelength $(\boldsymbol{nm})$	**200-500**	**500-900**	**900-2400**	**2500-5500**
solar simulator power $(\boldsymbol{W})$	0.8	1.5	2.1	-
absorptivity of patterned molybdenum	0.1	0.6	0.1	-
absorptivity of unpatterned molybdenum	0.1	0.4	0.1	-
emissivity of patterned molybdenum	-	-	-	0.35
emissivity of unpatterned molybdenum	-	-	-	0.16

Figure 5.16 summarises the simulation results of the effects on the highest achieved temperatures of varying the thermal contact conductance between the molybdenum sample and the quartz in six combinations. It can be seen that the samples achieved higher temperatures in vacuum than in air due to much less thermal convection. It clearly shows that increasing the thermal contact conductance increases the conduction loss from the sample to the quartz, which leads to lower temperature. It also shows that the patterned-flat case obtains the highest temperature when the thermal contact conductance is more than 100 W/(m^2·K). This is because the patterned-flat case has higher absorption than the other two cases. However, when the thermal contact conductance is less than 100 W/(m^2·K) the flat-flat case achieves a higher temperature than the patterned-flat and this seems somewhat unexpected. However, there are a number of effects occurring simultaneously here. As the contact conductance drops the achieved temperature will increase and radiative losses scale as T^4, and thus the lower emissivity of the flat-flat case becomes more dominant, and leads to higher

temperatures.

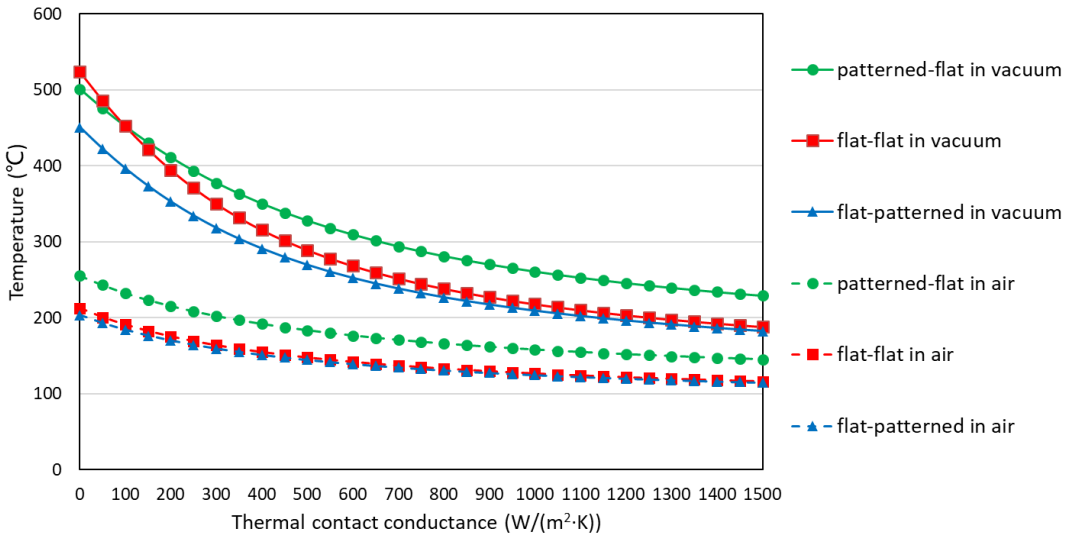

Figure 5.16 COMSOL simulation of the effects on the highest achieved temperatures by varying the thermal contact conductance between the molybdenum sample and the quartz holder

Measurements were then undertaken and shown in Figure 5.17 for three cases in air and in vacuum. The pressure inside the vacuum chamber is controlled at around 0.15 Torr for the vacuum cases. We used 700 W/(m^2·K) for the thermal contact conductance in the simulation which resulted in good agreement with the measurements.

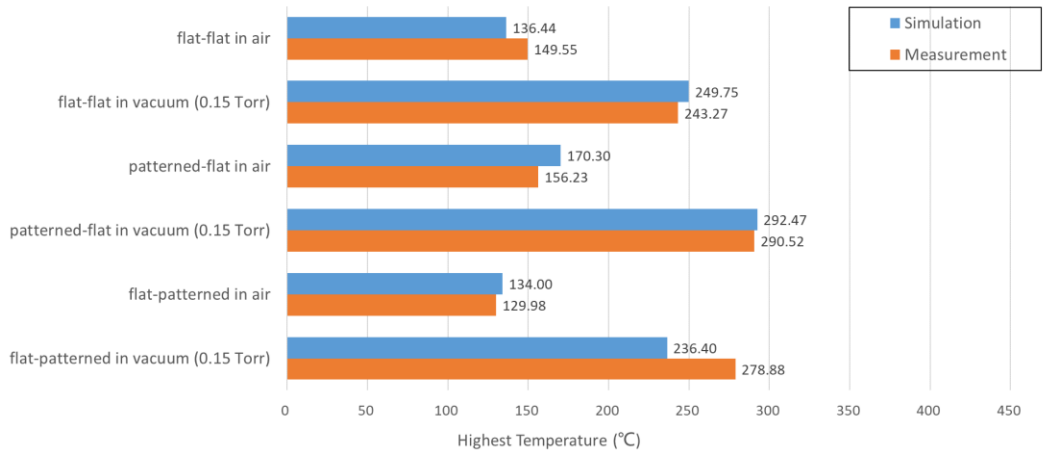

Figure 5.17 COMSOL simulated (thermal contact conductance=700 W/(m^2·K) and measured highest achieved temperature of patterned-flat, flat-flat, flat-patterned cases in air and vacuum (0.15 Torr)

Figure 5.18 shows a further measurement in a reduced vacuum level of 0.005 Torr compared to the of 0.15 Torr measurement shown in Figure 5.17. It can be seen that much higher temperature is now being achieved. In theory, the vacuum level in the chamber has little impact on the temperature when the pressure is under 1 Torr. For example, the highest temperature only drops 2.3% when the pressure increases from 0.001 Torr to 1 Torr in the simulation. However, the 0.005 Torr measurement result has a 48.2% increase compared to the 0.15 Torr one. It is difficult to explain such a result, but we speculate that this might be due to decreased contact conductance between the sample and the quartz in the 0.005 Torr case. When the sample has patterned surface contacting the quartz the thermal contact conductance is lower due to the roughness of the patterned surface. The flat-patterned case will have less conductive loss compared

to the patterned-flat and flat-flat case. Thus in Figure 5.18 we have used a thermal contact conductance of 50 W/(m^2·K) which gives a good level of agreement. This highlights the fact that much higher temperatures can be achieved by minimising the contact heat loss with the design improvement of the sample and the quartz holder.

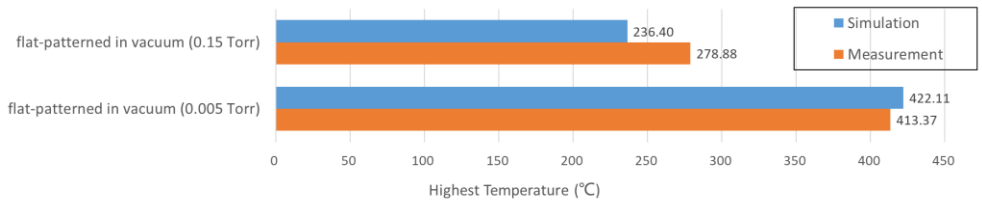

Figure 5.18 COMSOL simulated (thermal contact conductance=700 W/(m^2·K) for 0.15 Torr and 50 W/(m^2·K) for 0.005 Torr) and measured highest achieved temperature of flat-patterned case in vacuum of 0.15 Torr and 0.005 Torr

5.4. Chapter Conclusion

This chapter has presented experimental results of heating the micro-patterned molybdenum samples. We firstly tested all fabricated samples in air using a solar simulator and the temperature results shows good agreement with their measured absorptance. The in vacuum solar heating experiments conducted in India shows that >400°C sample temperature can be achieved using solar concentrators. This chapter also presents measured the temperatures achieved by patterned and unpatterned molybdenum samples in air and in vacuum using the vacuum device. It shows that more than 400 °C can be achieved with a solar simulator. In addition, our results provide

evidence for the importance of minimising the emissivity of the patterned surface at longer wavelength. In the next chapter, we will focus on reducing the conduction and convection loss with COMSOL simulations. We will also introduce a cold cathode into a fully sealed commercial grade vacuum device.

6. Thermal Optimisation and Thermionic Device Prototype

The key to solar thermal applications is to absorb as much of the incident energy as possible whilst minimising the thermal loss which includes radiation, conduction and convection. Chapter 4 focused on the radiation part where we investigated the optical characteristics of the 2D patterned molybdenum. In order to increase the sample temperature, we will investigate different factors which cause the thermal loss using COMSOL Multiphysics modelling. Then an improved design of the sample and mounting mechanism will be introduced and tested. This chapter will finish by looking at a prototype of thermionic convertor which introduces a cold cathode in a vacuum device.

6.1. COMSOL Multiphysics Thermal Modelling

We have shown an example of COMSOL Multiphysics thermal simulation in Chapter 3.1.4. We concluded that the convective heat transfer coefficient and the thermal contact conductance played a significant role in the model. In the next section, we will further discuss more factors which impact the target temperature of the sample.

6.1.1. Modelling Methodology

Figure 6.1 shows the schematic of the thermal modelling of an optimised thermal design. For the purpose of reducing the thermal loss from thermal conduction, the contact area between the sample and the quartz holder need to be minimised. This can be done by cutting the sample into a round sample with four arms as shown in Figure 6.1 (a). The sample only has four small arms contacting the quartz holder. A Gaussian profile heat source is applied directly on the middle of the sample top surface for 1000 seconds. The temperature monitor is on the back side of the sample. Table 6.1 lists all the variables we will investigate and see how they will affect the final equilibrium temperature. It also lists the default values for each parameter when varying other parameters. It should be noted that the convective heat transfer coefficient applies to all surfaces in the model and the ambient temperature is set to 24℃. The simulation is under vacuum condition as default. In addition, the sample emissivity shown in Table 6.1 is for its top patterned surface. All other surfaces of the sample have the emissivity of 0.1. The emissivity of the quartz surface is 0.9.

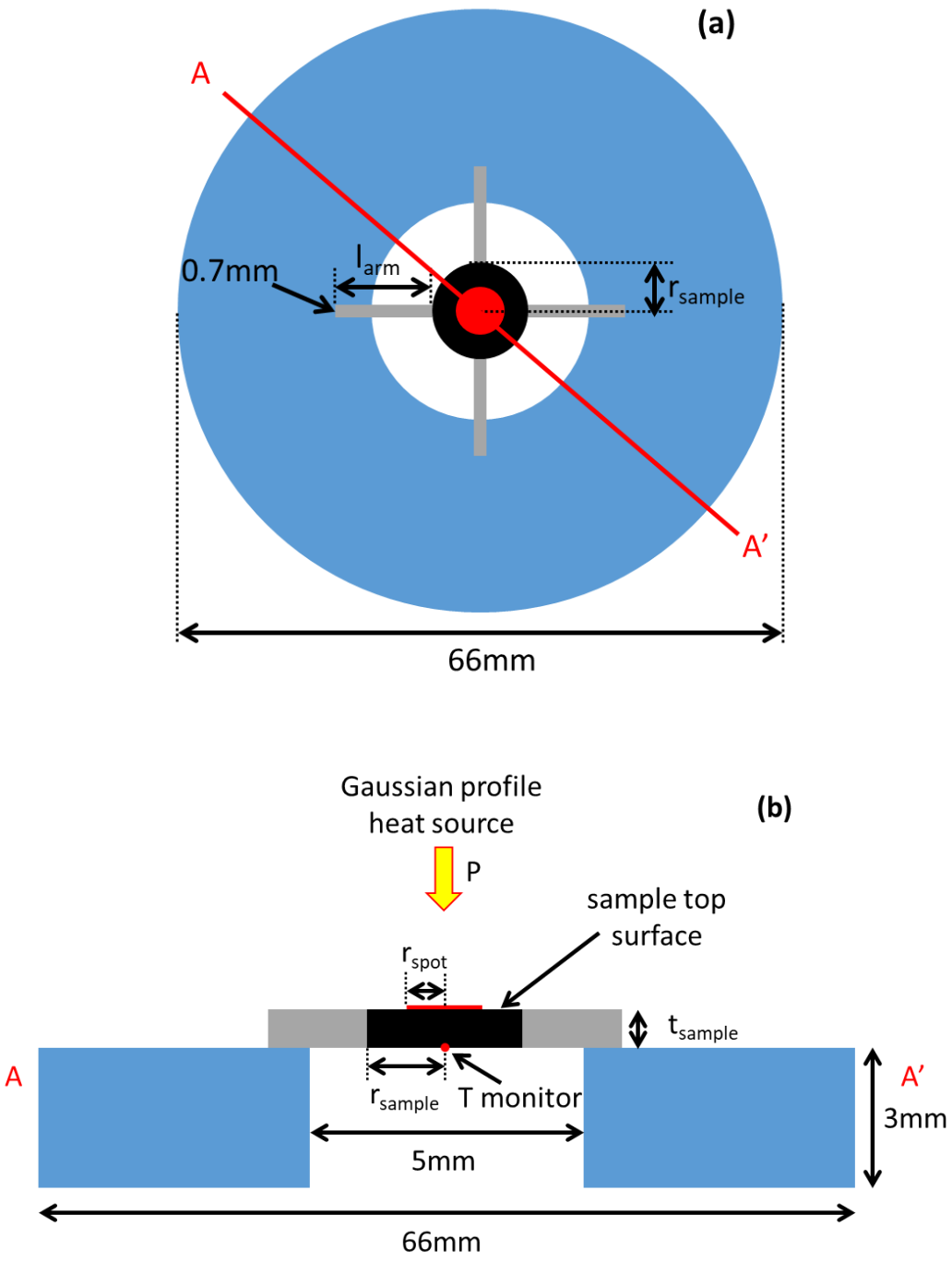

Figure 6.1 Simulated diagram of the sample mounting mechanism and Molybdenum sample with arms, (a) top view; (b) cross section

Table 6.1 Swept parameters in the modelling

NO.	Parameter	Description	Unit	Default value	Simulation sweep values
i	r_{sample}	sample radius	mm	3	2.0 - 4.8
ii	t_{sample}	sample thickness	mm	0.25	0.1 – 1.0
iii	$h_{contact}$	thermal contact conductance	$W/(m^2 \cdot K)$	1000	0 - 2000
iv	l_{arm}	sample arm length	mm	6	5 - 10
v	$h_{convective}$	convective heat transfer coefficient	$W/(m^2 \cdot K)$	0	0 - 100
vi	$\alpha_{sample\ top}$	absorptivity of the sample top surface	-	0.6	0 - 1
vii	$\varepsilon_{sample\ top}$	emissivity of the sample top surface	-	0.35	0 - 1
viii	P	input light power	W	4.4	1.5 – 15.0
ix	r_{spot}	light spot radius	mm	1.5	0.5 – 2.5

6.1.2. Modelling Results

Figure 6.2 (i-ix) show the modelled highest sample temperatures achieved after 1000s heating with varying nine parameters. From Figure 6.2 (i) and (ii), the result follows the trend of the temperature decreasing as the sample radius and thickness increases. This can be explained by equation 6.1 where Q is the thermal energy transferred, m is the mass of the body, C_p is the specific heat capacity of the material and ΔT is the change in temperature.

$$Q = mC_p\Delta T \tag{6.1}$$

With the increasing of the sample radius and thickness, the mass of the body increases. This leads to lower temperature change while the amount of the thermal energy transferred keeps the same. The results indicate that smaller and thinner sample can improve our target temperature. Although, the sample size needs to be larger than the light spot size in order to receive a total power input.

As shown in Figure 6.2 (iii) and (iv), the temperature shows significant decreases as the thermal contact conductance and the sample arm length increases. Larger thermal contact conductance means better contact between the sample arms and the quartz and longer sample arm length means larger contact area. From equation 2.3 in Chapter 2.3: $q_x = -\frac{T_2 - T_1}{\Delta x_A/(k_A A) + 1/(h_c A) + \Delta x_B/(k_B A)}$, we can know that more heat transfer from the higher temperature sample to the lower temperature quartz through conduction, which

leads to lower temperature. The results show that reducing the thermal contact between the sample and the quartz holder is the top priority in the future design. It also rises challenges for the machining of the sample and quartz since a small change in the size and shape could lead to a dramatic change in results. This may explain the inconsistency problem appeared in the previous measurement in Chapter 5.3.

Figure 6.2 (v) shows the effect of changing the convective heat transfer coefficient. The temperature can decrease significantly when the sample and the quartz holder are not in the vacuum ($h_c \approx 0$ W/(m^2·K)). This demonstrates the importance of putting the test system under high vacuum.

Figure 6.2 (vi) and (vii) show a higher temperature can be achieved when the illuminated sample surface has a higher absorptivity and a lower emissivity. It verified importance of developing highly selective solar absorbers in solar thermal applications.

Figure 6.2 (viii) and (ix) focus on the light source. It clearly shows that a higher power input results a significantly higher temperature. On the other hand, the spot size of the light does not matter much if it is smaller than the sample size. This reveals that a solar concentration system needs to be used for obtaining higher temperature.

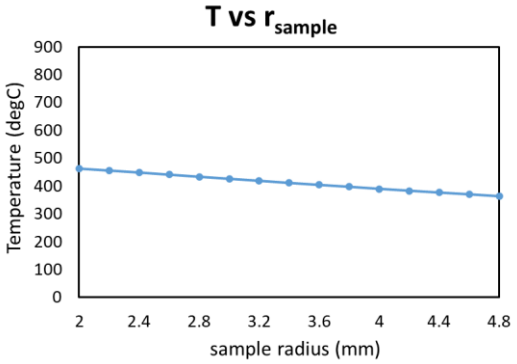

(i)

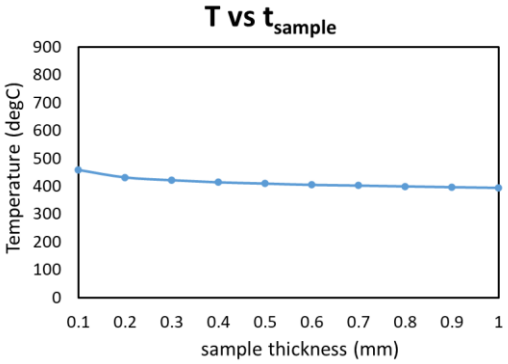

(ii)

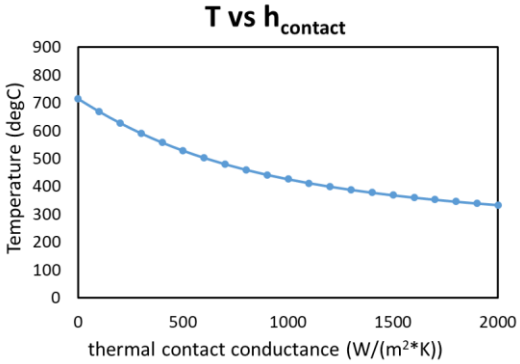

(iii)

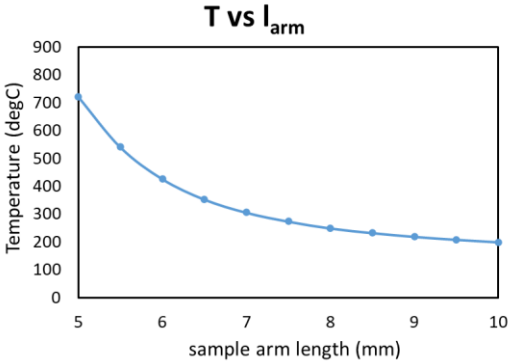

(iv)

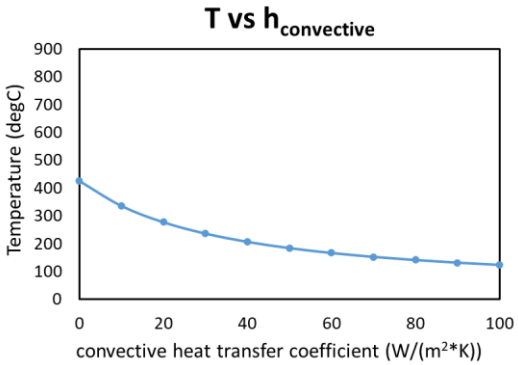

(v)

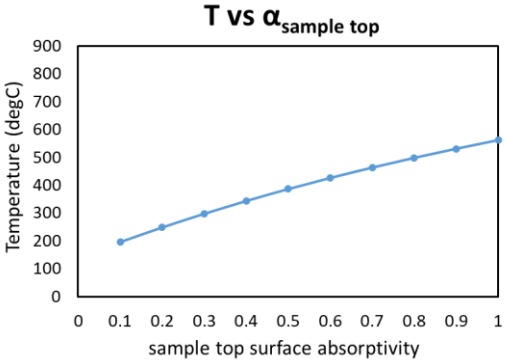

(vi)

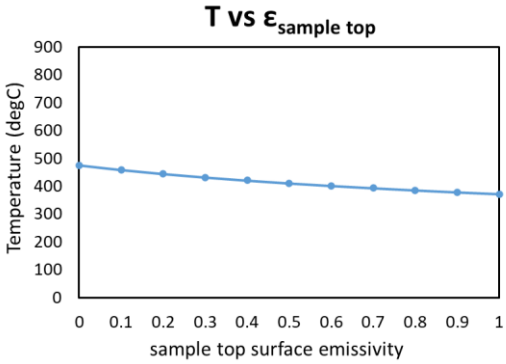

(vii)

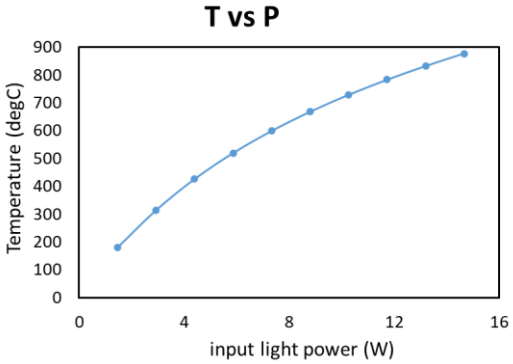

(viii)

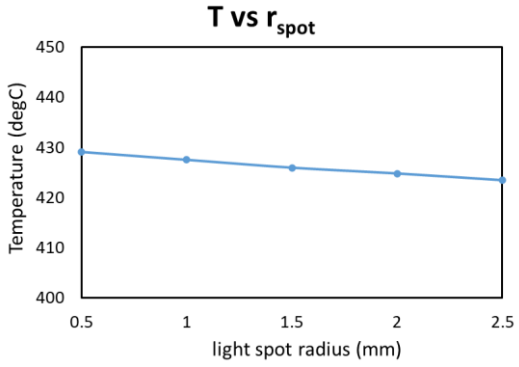

(ix)

Figure 6.2 Simulated highest sample temperatures achieved after 1000s heating by varying nine parameters in the model, (i) sample radius; (ii) sample thickness; (iii) thermal contact conductance; (iv) length of the sample arm; (v) convective heat transfer coefficient; (vi) absorptivity of the sample top surface; (vii) emissivity of the sample top surface; (viii) input light power; (ix) light spot radius.

6.2. Thermionic Convertor Prototype

From the results we obtained in the last section, we designed a new molybdenum sample with a new mounting mechanism as shown in Figure 6.3 (c). The design has two quartz holders. The bottom one as shown in Figure 6.3 (b) has a hole in the centre and a recess for the round collector which is a piece of 0.5mm thick molybdenum. The depth of the recess in the bottom quartz equals to the thickness of the collector and the gap between the emitter and the collector. A copper wire can be soldered on the bottom of the molybdenum collector. The copper wire is used for electric connection and it also can pull the collector to hold it in place. The top quartz holder as shown in Figure 6.3 (a) and the bottom quartz are screwed together. Then a star shape 0.25mm molybdenum emitter fits inside the cut-out of the top quartz. The arms of the emitter sit on the bottom quartz and create a small gap between the emitter and collector. To fix the emitter, some alumina sheets are placed between the arms and top mounting bars. Figure 6.4 shows a detailed schematic of the design.

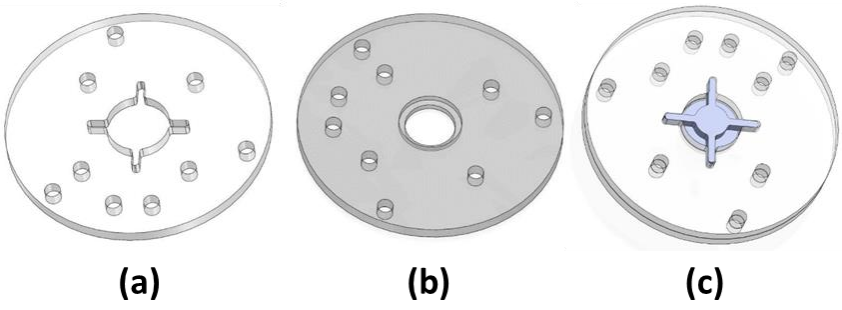

Figure 6.3 Thermionic convertor design, (a) top quartz holder; (b) bottom quartz holder; (c) assembly with molybdenum emitter and collector

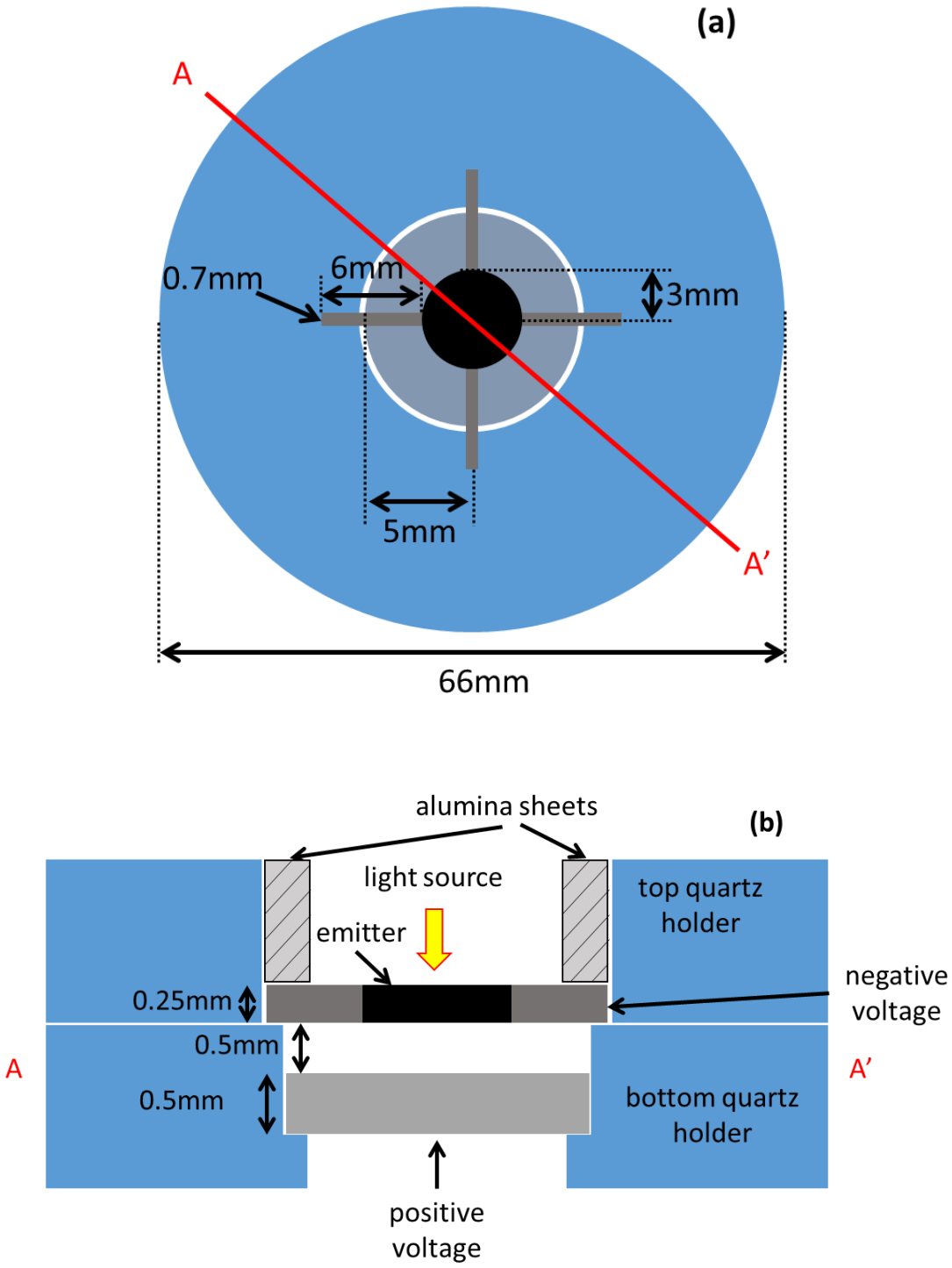

Figure 6.4 schematic of proposed thermionic convertor design (a) top view; (b) cross section view

Previous studies showed that an optimal gap of 1~100 μm is needed for high energy conversion of thermionic convertors [127]. It is also possible to use ceramic micro-beads to fill the gap [128]. Due to the machining limitation, we begin to set the gap in our design to 0.5 mm.

Figure 6.5 shows the simulated results of the emitter and collector temperatures achieved after 1000s heating on the emitter with different gap size. The simulation parameters are the same as previously stated in section 6.1.2. It clearly shows that the gap size does not impact on the heat transfer between the emitter and the collector. Although the collector temperature rises to approximately 53°C which is 29°C higher than the ambient temperature. It implies that a heat sink can be used to lower the collector temperature. This could further increase the temperature difference between the emitter and the collector; hence a higher efficiency can be achieved.

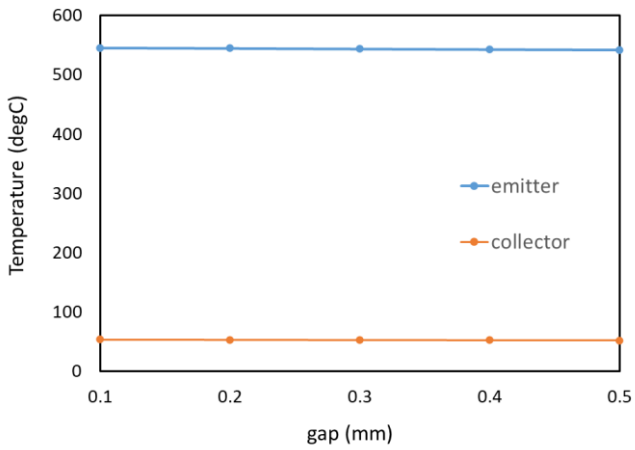

Figure 6.5 Simulated equilibrium emitter and collector temperatures achieved after 1000s heating on the emitter with different gap

Before the assembly of the thermionic convertor, we have tested the performance of the newly designed mounting mechanism. As shown in Figure 6.6 (a), a piece of flat molybdenum (0.25 mm thickness, 0.3 mm radius) with four arms was heated up using the solar simulator. The measurement setup has kept the same as previous in-lab vacuum device experiments. The only difference is that the dome vacuum device was replaced to the flat device which was used in India. The measured results are shown in Figure 6.6 (b) where the temperature reached 350°C. It also shows good agreement with the simulated result (red dotted line). This test showed good performance of the thermionic convertor and a higher temperature can be achieved with patterned molybdenum emitter and a higher power input.

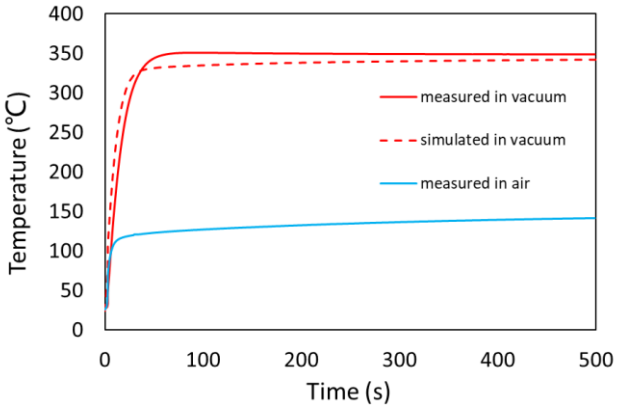

(a) *(b)*

Figure 6.6 (a) star shape flat molybdenum tested in vacuum device; (b) measured temperature response of the flat molybdenum after 500s solar simulator heating in air and in vacuum. Red dotted line shows the simulated temperature rise of the flat molybdenum after 500s solar simulator heating in vacuum.

Figure 6.7 shows an integrated one-off thermionic device. The mounting screws are embedded in a glass tube with a dome shape top. The quartz holder presented in Figure 6.6 (a) can be mounted on the screws. These screws can also function as electric connections for positive and negative leads for the convertor. After the assembly of the quartz holder, the system can be sealed in vacuum in a larger glass tube. This proposed one-off thermionic device is cheap to produce and smaller and lighter than the vacuum device. It can be easily mounted on solar concentration systems for higher power input and achieve a higher temperature on the emitter.

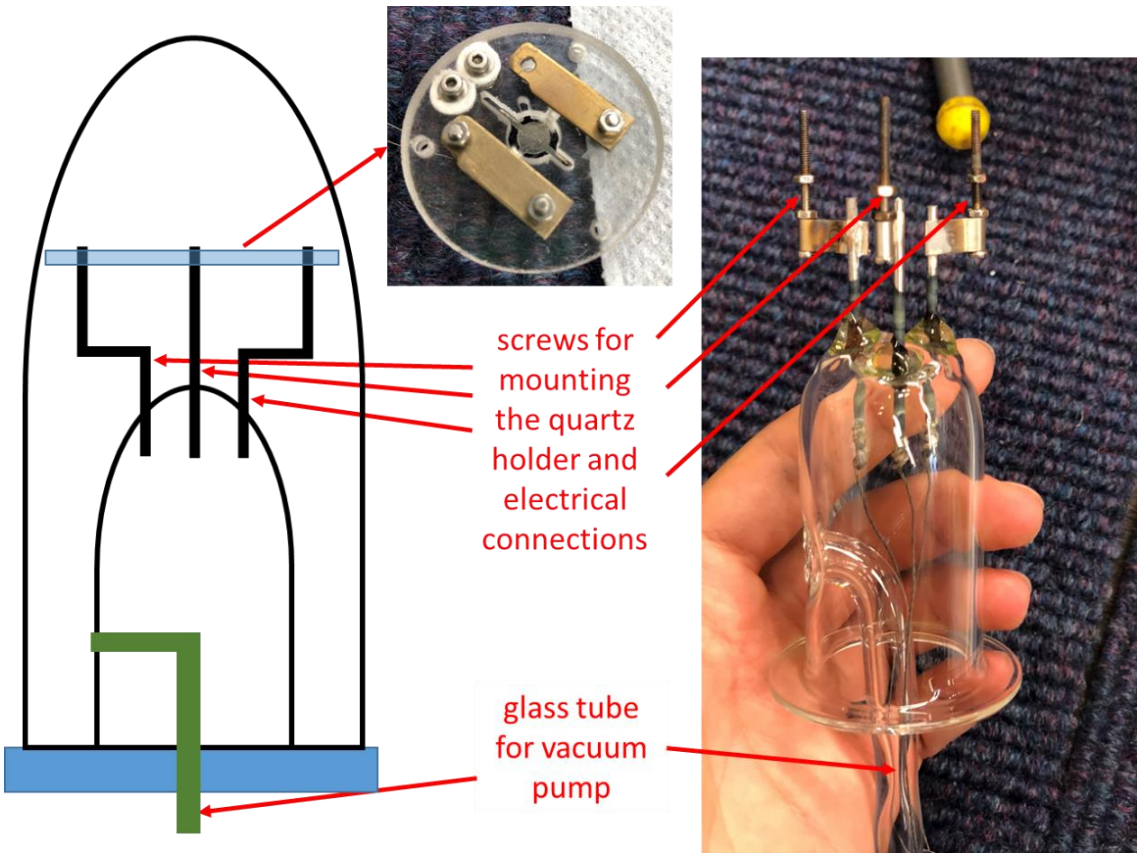

Figure 6.7 Integrated thermionic convertor

6.3. Chapter Conclusion

We have investigated the COMSOL Multiphysics thermal modelling of the molybdenum sample on the quartz holder in this chapter. It has been demonstrated that many factors can heavily impact the temperature of the molybdenum. Minimising the thermal contact between the sample and the quartz holder became a priority in our later thermionic convertor design. We have presented the thermionic convertor design with a thin molybdenum emitter with four arms and a thicker molybdenum collector. The mounting mechanism ensured a 0.5mm gap between the two electrodes and can be used for both temperature and electrical measurements. We have also demonstrated an integrated thermionic convertor ready for assembly and solar heating experiments.

7. Conclusion and Future Works

7.1. Conclusion

This thesis has presented the measured optical absorptivity and emissivity of micro-patterned molybdenum produced by laser etching. We have shown that this technique dramatically increases the absorptivity of molybdenum across 500-900 nm which is ideal for solar thermal applications. Temperature results have been shown for the structures with different hole sizes and different periods in air. We have designed a vacuum device and measured the temperatures achieved by patterned and unpatterned molybdenum samples in air and in vacuum. It shows that more than 400℃ can be achieved with low solar concentration. In addition, our results provide evidence for the importance of minimising the emissivity of the patterned surface at longer wavelength. Detailed COMSOL simulation has been used to predict the maximum temperature achievable in vacuum. A thermionic emission convertor prototype has been developed for future experiments.

Chapter 1 introduced the motivation for research into solar energy technologies and presented different types of operations. We have shown that solar thermionic energy converters are a much more direct and potentially more efficient way of generating electricity from solar energy.

Chapter 2 provided a general introduction to the theories in heat transfer, which are essential to analyse and understand the thermal behaviour in solar thermionic energy convertors. Different types of selective absorbers have been presented, with an emphasis on the potential of surface micropatterning.

Chapter 3 details the computational techniques used throughout this work. COMSOL Multiphysics has been used for analysing and predicting the heat transfer between the sample and its holder. Lumerical FDTD was used for characterising the optical behaviour of the microstructures.

Chapter 4 introduced the low-cost laser etching technique to fabricate the micropatterned molybdenum samples. Optical absorptivity and emissivity have been measured using an integrating sphere and an IR microscope.

Chapter 5 showed various heating measurements on the molybdenum samples in air and in vacuum. In air measurements showed good agreement with the absorptivity measurements in different samples. In vacuum measurements showed that >400°C can be achieved with flux density of ~192 suns with direct sunlight and flux density of ~44

with a solar simulator.

Chapter 6 further investigated the conduction and convection heat loss in the vacuum device. A new sample and quartz holder were developed to minimise the thermal loss. The design also integrated the molybdenum sample as an emitter and a thicker molybdenum as a collector with a 0.5 mm gap. The thermionic convertor prototype has been shown with the potential of being a fully sealed commercial grade vacuum device.

7.2. Future Works

There are several future works that can be explored in this area of research. Here are some suggestions:

More detailed optical simulations can be done on the microstructures of the molybdenum samples. A structure with optimised period and etch depth could increase its temperature performance. Other samples with different material and structure fabricated using different techniques can be easily tested in the vacuum devices.

The limitation of the machining on the sample and quartz could introduce large errors in the temperature measurements. The vacuum level inside the vacuum device also could affect the measurement results. Although we have tried to tackle these issues by improving the designs, further investigations can be done with more tests and new designs.

In order to achieve higher temperature (>500℃) for thermionic energy convertors, a better solar concentrator with higher concentration ratio can be used. We currently have a dual axis solar tracker and a parabola solar cooker. The vacuum chamber or vacuum sealed thermionic convertor prototype can be tested on these devices in the future.

Finally, the proposed thermionic convertor is ready for assembling and electrical testing. It is also possible to adapt the flat plates design to a thermionic tube which can be used on parabolic trough reflectors.

8. References

[1] BP, "BP Statistical Review of World Energy," 2019. [Online]. Available: https://www.bp.com/content/dam/bp/businesssites/en/global/corporate/pdfs/energy-economics/statistical-review/bp-stats-review-2019-full-report.pdf

[2] M. Dunn, *Exploring your world: The adventure of geography*. National Geographic Society, 1989.

[3] V. Smil, *Energy: a beginner's guide*. Oneworld Publications, 2017.

[4] R. Petela, *Engineering thermodynamics of thermal radiation for solar power utilization*. McGraw Hill, 2010.

[5] CRISP. "Optical Remote Sensing." http://www.crisp.nus.edu.sg/~research/tutorial/optical.htm (accessed Jan 2020).

[6] G. Boyle, "Renewable energy," *Renewable Energy, by Edited by Godfrey Boyle, pp. 456. Oxford University Press, May 2004. ISBN-10: 0199261784. ISBN-13: 9780199261789,* p. 456, 2004.

[7] C. Frohlich, "Construction of a Composite Total Solar Irradiance (TSI) Time Series from 1978 to present," *Physikalisch-Meteorologisches Observatorium Davos,* 2006.

[8] G. Kopp, G. Lawrence, and G. Rottman, "The total irradiance monitor (TIM): science results," in *The Solar Radiation and Climate Experiment (SORCE)*: Springer, 2005, pp. 129-139.

[9] A. V. D. Rosa, "Fundamentals of Renewable Energy Processes (Third)," ed: Elsevier Academic Press, 2012.

[10] R. Williams, "Becquerel photovoltaic effect in binary compounds," *The journal of Chemical physics,* vol. 32, no. 5, pp. 1505-1514, 1960.

[11] A. Chodos, "Bell labs demonstrates the first practical silicon solar cell," *APS Physics,* 2009.

[12] D. M. Chapin, C. S. Fuller, and G. L. Pearson, "A new silicon p-n junction photocell for converting solar radiation into electrical power," *Journal of Applied Physics,* vol. 25, no. 5, pp. 676-677, 1954.

[13] I. S. instruments, "Photovoltaic Cells – Generating electricity," ed, 2009.

[14] P. Matyba, K. Maturova, M. Kemerink, N. D. Robinson, and L. Edman, "The dynamic organic p–n junction," *Nature materials,* vol. 8, no. 8, pp. 672-676, 2009.

[15] L. A. Kosyachenko, *Solar Cells: New Approaches and Reviews*. BoD–Books on Demand, 2015.

[16] S. A. Kalogirou, "Solar thermal collectors and applications," *Progress in Energy and Combustion Science,* vol. 30, no. 3, pp. 231-295, 2004/01/01/ 2004, doi: https://doi.org/10.1016/j.pecs.2004.02.001.

[17] V. Dallakyan and R. Vardanyan, "Mirror Refelcting Cost Effective PV Solar Energy Concentrating System," 2005, pp. 141-143.

[18] Y. Chu and P. Meisen, "Review and comparison of different solar energy technologies," *Global Energy Network Institute (GENI), San Diego, CA,* 2011.

[19] A. Sharma, "A comprehensive study of solar power in India and World," *Renewable and Sustainable Energy Reviews,* vol. 15, no. 4, pp. 1767-1776, 2011.

[20] M. T. Islam, N. Huda, A. B. Abdullah, and R. Saidur, "A comprehensive review of state-of-the-art concentrating solar power (CSP) technologies: Current status and research trends," *Renewable and Sustainable Energy Reviews,* vol. 91, pp. 987-1018, 2018.

[21] T. M. Pavlović, I. S. Radonjić, D. D. Milosavljević, and L. S. Pantić, "A review of concentrating solar power plants in the world and their potential use in Serbia," *Renewable and Sustainable Energy Reviews,* vol. 16, no. 6, pp. 3891-

3902, 2012.

[22] A. Ummadisingu and M. S. Soni, "Concentrating solar power–technology, potential and policy in India," *Renewable and sustainable energy reviews,* vol. 15, no. 9, pp. 5169-5175, 2011.

[23] W. Thomson, "4. on a mechanical theory of thermo-electric currents," *Proceedings of the Royal society of Edinburgh,* vol. 3, pp. 91-98, 1857.

[24] L. D. Hicks, T. C. Harman, X. Sun, and M. S. Dresselhaus, "Experimental study of the effect of quantum-well structures on the thermoelectric figure of merit," *Physical Review B,* vol. 53, no. 16, p. R10493, 1996.

[25] E. Velmre, "Thomas Johann Seebeck (1770-1831)," *Estonian Journal of Engineering,* vol. 13, no. 4, 2007.

[26] R. W. Miles, K. M. Hynes, and I. Forbes, "Photovoltaic solar cells: An overview of state-of-the-art cell development and environmental issues," *Progress in crystal growth and characterization of materials,* vol. 51, no. 1-3, pp. 1-42, 2005.

[27] S. Volz, *Thermal nanosystems and nanomaterials*. Springer Science & Business Media, 2009.

[28] G. Hatsopoulos, "Thermionic Energy Conversion," 1966, p. 2318.

[29] S.-J. Liang and L. K. Ang, "Electron thermionic emission from graphene and a thermionic energy converter," *Physical Review Applied,* vol. 3, no. 1, p. 014002, 2015.

[30] T. A. EDISON, "Electrical indicator," 1883.

[31] N. S. Rasor, "Thermionic energy conversion plasmas," *IEEE Transactions on Plasma Science,* vol. 19, no. 6, pp. 1191-1208, 1991.

[32] M. Shimizu *et al.*, "JSUS solar thermal thruster and its integration with thermionic power converter," 1998, vol. 420: American Institute of Physics, 1 ed., pp. 364-369.

[33] J. W. Schwede *et al.*, "Photon-enhanced thermionic emission for solar concentrator systems," *Nature materials,* vol. 9, no. 9, pp. 762-767, 2010.

[34] A. Shakouri, "Thermoelectric, thermionic and thermophotovoltaic energy

conversion," 2005: IEEE, pp. 507-512.

[35] P. W. May, J. C. Stone, M. N. R. Ashfold, K. R. Hallam, W. N. Wang, and N. A. Fox, "The effect of diamond surface termination species upon field emission properties," *Diamond and related materials,* vol. 7, no. 2-5, pp. 671-676, 1998.

[36] A. Croot, G. Wan, A. Rowan, H. D. Andrade, J. A. Smith, and N. A. Fox, "Beta Radiation Enhanced Thermionic Emission from Diamond Thin Films," *Frontiers in Mechanical Engineering,* vol. 3, p. 17, 2017.

[37] H. Cen, S. Nunez-Sanchez, A. Sarua, I. Bickerton, N. A. Fox, and M. J. Cryan, "Solar thermal characterization of micropatterned high temperature selective surfaces," *Journal of Photonics for Energy,* vol. 10, no. 2, p. 024503, 2020.

[38] H. A. Buchdahl, "The concepts of classical thermodynamics," *cct,* 2009.

[39] R.-G. Cai and S. P. Kim, "First law of thermodynamics and Friedmann equations of Friedmann-Robertson-Walker universe," *Journal of High Energy Physics,* vol. 2005, no. 02, p. 050, 2005.

[40] C. Rudolf, "On the Motive Power of Heat, and on the Laws which can be deduced from it for the Theory of Heat. Poggendorff's Annalen der Physik, LXXIX," ed: Dover Reprint, 1850.

[41] J. Wilks, *The third law of thermodynamics*. Clarendon Press, 1961.

[42] M. Blanco and L. R. Santigosa, *Advances in concentrating solar thermal research and technology*. Woodhead Publishing, 2016.

[43] J. P. Holman, *Heat transfer*. McGraw-hill, 2010.

[44] J. Fourier, "The Analytical Theory of Heat, translated with notes by A," ed: Freeman, 1955.

[45] L. S. Fletcher, "Recent developments in contact conductance heat transfer," *Journal of Heat Transfer,* vol. 110, no. 4b, pp. 1059-1070, 1988.

[46] M. Williamson and A. Majumdar, "Effect of surface deformations on contact conductance," *Journal of heat transfer,* vol. 114, no. 4, pp. 802-810, 1992.

[47] Y. Gan, F. Hernandez, D. Hanaor, R. Annabattula, M. Kamlah, and P. Pereslavtsev, "Thermal discrete element analysis of EU solid breeder blanket subjected to neutron irradiation," *Fusion Science and Technology,* vol. 66, no.

1, pp. 83-90, 2014.

[48] C. T. O'Sullivan, "Newton's law of cooling—A critical assessment," *American Journal of Physics,* vol. 58, no. 10, pp. 956-960, 1990.

[49] S. W. Churchill and H. H. S. Chu, "Correlating equations for laminar and turbulent free convection from a vertical plate," *International journal of heat and mass transfer,* vol. 18, no. 11, pp. 1323-1329, 1975.

[50] W. H. McAdams, "Heat Transmission,(1954)," *McGraw Hills,* 2012.

[51] R. M. Goody and Y. L. Young, "Atmospheric Radiation: theoretical basis, California Institute of technology," ed: copyright Oxford University Press,(1961-1989).

[52] G. Kirchhoff, "I. On the relation between the radiating and absorbing powers of different bodies for light and heat," *The London, Edinburgh, and Dublin Philosophical Magazine and Journal of Science,* vol. 20, no. 130, pp. 1-21, 1860.

[53] R. Van Zee and J. P. Looney, *Cavity-enhanced spectroscopies*. Elsevier, 2003.

[54] M. Planck, *The theory of heat radiation*. Courier Corporation, 2013.

[55] C. S. Goldenstein, V. A. Miller, R. M. Spearrin, and C. L. Strand, "SpectraPlot. com: Integrated spectroscopic modeling of atomic and molecular gases," *Journal of Quantitative Spectroscopy and Radiative Transfer,* vol. 200, pp. 249-257, 2017.

[56] G. H. Wannier, "The statistical problem in cooperative phenomena," *Reviews of Modern Physics,* vol. 17, no. 1, p. 50, 1945.

[57] J. A. Duffie and W. A. Beckman, *Solar engineering of thermal processes*. John Wiley & Sons, 2013.

[58] H. Tabor, "Solar energy research: Program in the new desert research institute in Beersheba," *Solar Energy,* vol. 2, no. 1, pp. 3-6, 1958.

[59] P. Bermel, J. Lee, J. D. Joannopoulos, I. Celanovic, and M. Soljačić, "Selective solar absorbers," *Annual Review of Heat Transfer,* vol. 15, 2012.

[60] P. K. Nair and M. T. S. Nair, "Chemically deposited SnS-CuxS thin films with high solar absorptance: new approach to all-glass tubular solar collectors," *Journal of Physics D: Applied Physics,* vol. 24, no. 1, p. 83, 1991.

[61] R. Bayón, G. San Vicente, C. Maffiotte, and Á. Morales, "Preparation of selective absorbers based on CuMn spinels by dip-coating method," *Renewable Energy,* vol. 33, no. 2, pp. 348-353, 2008.

[62] S. Pal, D. Diso, S. Franza, A. Licciulli, and L. Rizzo, "Spectrally selective absorber coating from transition metal complex for efficient photothermal conversion," *Journal of materials science,* vol. 48, no. 23, pp. 8268-8276, 2013.

[63] Y. Yin, L. Hang, S. Zhang, and X. L. Bui, "Thermal oxidation properties of titanium nitride and titanium–aluminum nitride materials—A perspective for high temperature air-stable solar selective absorber applications," *Thin Solid Films,* vol. 515, no. 5, pp. 2829-2832, 2007.

[64] D. Zhu, F. Mao, and S. Zhao, "The influence of oxygen in TiAlOxNy on the optical properties of colored solar-absorbing coatings," *Solar energy materials and solar cells,* vol. 98, pp. 179-184, 2012.

[65] Y. Liu, C. Wang, and Y. Xue, "The spectral properties and thermal stability of NbTiON solar selective absorbing coating," *Solar energy materials and solar cells,* vol. 96, pp. 131-136, 2012.

[66] N. Selvakumar, N. T. Manikandanath, A. Biswas, and H. C. Barshilia, "Design and fabrication of highly thermally stable HfMoN/HfON/Al2O3 tandem absorber for solar thermal power generation applications," *Solar energy materials and solar cells,* vol. 102, pp. 86-92, 2012.

[67] E. Randich and D. D. Allred, "Chemically vapor-deposited ZrB2 as a selective solar absorber," *Thin Solid Films,* vol. 83, no. 4, pp. 393-398, 1981.

[68] C. M. Lampert, "Coatings for enhanced photothermal energy collection I. Selective absorbers," *Solar Energy Materials,* vol. 1, no. 5-6, pp. 319-341, 1979.

[69] M. Okuyama, K. Saji, T. Adachi, H. Okamoto, and Y. Hamakawa, "Selective absorber using glow-discharge amorphous silicon for solar photothermal conversion," *Solar Energy Materials,* vol. 3, no. 3, pp. 405-413, 1980.

[70] S. Chatterjee and U. Pal, "Low-cost solar selective absorbers from Indian galena," *Optical Engineering,* vol. 32, no. 11, pp. 2923-2930, 1993.

[71] P. Bermel *et al.*, "Design and global optimization of high-efficiency thermophotovoltaic systems," *Optics express,* vol. 18, no. 103, pp. A314-A334, 2010.

[72] N. P. Sergeant, O. Pincon, M. Agrawal, and P. Peumans, "Design of wide-angle solar-selective absorbers using aperiodic metal-dielectric stacks," *Optics express,* vol. 17, no. 25, pp. 22800-22812, 2009.

[73] M.-H. Liu *et al.*, "High efficiency of photon-to-heat conversion with a 6-layered metal/dielectric film structure in the 250-1200 nm wavelength region," *Optics express,* vol. 22, no. 107, pp. A1843-A1852, 2014.

[74] H. C. Barshilia, N. Selvakumar, G. Vignesh, K. S. Rajam, and A. Biswas, "Optical properties and thermal stability of pulsed-sputter-deposited AlxOy/Al/AlxOy multilayer absorber coatings," *Solar Energy Materials and Solar Cells,* vol. 93, no. 3, pp. 315-323, 2009.

[75] N. Selvakumar, H. C. Barshilia, K. S. Rajam, and A. Biswas, "Structure, optical properties and thermal stability of pulsed sputter deposited high temperature HfOx/Mo/HfO2 solar selective absorbers," *Solar Energy Materials and Solar Cells,* vol. 94, no. 8, pp. 1412-1420, 2010.

[76] F. Cao, K. McEnaney, G. Chen, and Z. Ren, "A review of cermet-based spectrally selective solar absorbers," *Energy & Environmental Science,* vol. 7, no. 5, pp. 1615-1627, 2014.

[77] C. E. Kennedy, "Review of mid-to high-temperature solar selective absorber materials," National Renewable Energy Lab., Golden, CO.(US), 2002.

[78] N. Selvakumar and H. C. Barshilia, "Review of physical vapor deposited (PVD) spectrally selective coatings for mid-and high-temperature solar thermal applications," *Solar energy materials and solar cells,* vol. 98, pp. 1-23, 2012.

[79] L. Gaouyat *et al.*, "Revealing the innermost nanostructure of sputtered NiCrOx solar absorber cermets," *Solar energy materials and solar cells,* vol. 122, pp. 303-308, 2014.

[80] F. Cao, D. Kraemer, T. Sun, Y. Lan, G. Chen, and Z. Ren, "Enhanced Thermal Stability of W-Ni-Al2O3 Cermet-Based Spectrally Selective Solar Absorbers with Tungsten Infrared Reflectors," *Advanced Energy Materials,* vol. 5, no. 2, p. 1401042, 2015.

[81] Q.-C. Zhang, Y. Yin, and D. R. Mills, "High efficiency Mo Al2O3 cermet selective surfaces for high-temperature application," *Solar Energy materials and solar cells,* vol. 40, no. 1, pp. 43-53, 1996.

[82] D. Chester, P. Bermel, J. D. Joannopoulos, M. Soljacic, and I. Celanovic,

"Design and global optimization of high-efficiency solar thermal systems with tungsten cermets," *Optics express,* vol. 19, no. 103, pp. A245-A257, 2011.

[83] E. Rephaeli and S. Fan, "Absorber and emitter for solar thermo-photovoltaic systems to achieve efficiency exceeding the Shockley-Queisser limit," *Optics express,* vol. 17, no. 17, pp. 15145-15159, 2009.

[84] M. Hasumi and H. Yugami, "Development of solar selective absorbers and sky radiators based on two-dimensional diffractive grating surfaces," 2006, vol. 6197: International Society for Optics and Photonics, p. 61970V.

[85] A. Lasagni, F. Mücklich, M. R. Nejati, and R. Clasen, "Periodical surface structuring of metals by laser interference metallurgy as a new fabrication method of textured solar selective absorbers," *Advanced engineering materials,* vol. 8, no. 6, pp. 580-584, 2006.

[86] N. P. Sergeant, M. Agrawal, and P. Peumans, "High performance solar-selective absorbers using coated sub-wavelength gratings," *Optics express,* vol. 18, no. 6, pp. 5525-5540, 2010.

[87] X. Xiao *et al.*, "A facile process to prepare copper oxide thin films as solar selective absorbers," *Applied Surface Science,* vol. 257, no. 24, pp. 10729-10736, 2011.

[88] A. Chaudhary and H. C. Barshilia, "Nanometric multiscale rough CuO/Cu (OH) 2 superhydrophobic surfaces prepared by a facile one-step solution-immersion process: transition to superhydrophilicity with oxygen plasma treatment," *The Journal of Physical Chemistry C,* vol. 115, no. 37, pp. 18213-18220, 2011.

[89] H. Wang and L. Wang, "Perfect selective metamaterial solar absorbers," *Optics express,* vol. 21, no. 106, pp. A1078-A1093, 2013.

[90] W.-Q. Wu, H.-S. Rao, H.-L. Feng, H.-Y. Chen, D.-B. Kuang, and C.-Y. Su, "A family of vertically aligned nanowires with smooth, hierarchical and hyperbranched architectures for efficient energy conversion," *Nano Energy,* vol. 9, pp. 15-24, 2014.

[91] H. Sai and Y. Kanamori, "Spectrally selective thermal radiators and absorbers with periodic microstructured surface for high-temperature applications," *Microscale Thermophysical Engineering,* vol. 7, no. 2, pp. 101-115, 2003.

[92] H. Sai, H. Yugami, Y. Kanamori, and K. Hane, "Solar selective absorbers based on two-dimensional W surface gratings with submicron periods for high-

temperature photothermal conversion," *Solar energy materials and solar cells,* vol. 79, no. 1, pp. 35-49, 2003.

[93] M. H. Huang *et al.*, "Room-temperature ultraviolet nanowire nanolasers," *science,* vol. 292, no. 5523, pp. 1897-1899, 2001.

[94] J. Zhu *et al.*, "Optical absorption enhancement in amorphous silicon nanowire and nanocone arrays," *Nano letters,* vol. 9, no. 1, pp. 279-282, 2009.

[95] J. J. Cuomo, J. F. Ziegler, and J. M. Woodall, "A new concept for solar energy thermal conversion," *Applied Physics Letters,* vol. 26, no. 10, pp. 557-559, 1975.

[96] M. Kussmaul, M. J. Mirtich, and A. Curren, "Ion beam treatment of potential space materials at the NASA Lewis Research Center," *Surface and Coatings Technology,* vol. 51, no. 1-3, pp. 299-306, 1992.

[97] C. Multiphysics, "Introduction to COMSOL Multiphysics®," *COMSOL Multiphysics, Burlington, MA, accessed Feb,* vol. 9, p. 2018, 1998.

[98] T. J. R. Hughes, *The finite element method: linear static and dynamic finite element analysis*. Courier Corporation, 2012.

[99] O. C. Zienkiewicz, R. L. Taylor, P. Nithiarasu, and J. Z. Zhu, *The finite element method*. McGraw-hill London, 1977.

[100] A. Hrennikoff, "Solution of problems of elasticity by the framework method," *J. appl. Mech.,* 1941.

[101] R. Courant, *Variational methods for the solution of problems of equilibrium and vibrations*. Verlag nicht ermittelbar, 1943.

[102] E. Hinton and B. Irons, "Least squares smoothing of experimental data using finite elements," *Strain,* vol. 4, no. 3, pp. 24-27, 1968.

[103] A. Quarteroni and A. Valli, *Numerical approximation of partial differential equations*. Springer Science & Business Media, 2008.

[104] C. Multiphysics. "The Finite Element Method (FEM)." https://uk.comsol.com/multiphysics/finite-element-method (accessed Jan, 2020).

[105] E. ToolBox. "*Convective Heat Transfer*." https://www.engineeringtoolbox.com/convective-heat-transfer-d_430.html (accessed Jan, 2020).

[106] J. Ekin, *Experimental techniques for low-temperature measurements: cryostat design, material properties and superconductor critical-current testing*. Oxford university press, 2006.

[107] F. Lumerical, "Solutions," ed, 2016.

[108] A. Taflove and S. C. Hagness, *Computational electrodynamics: the finite-difference time-domain method*. Artech house, 2005.

[109] K. Yee, "Numerical solution of initial boundary value problems involving Maxwell's equations in isotropic media," *IEEE Transactions on antennas and propagation,* vol. 14, no. 3, pp. 302-307, 1966.

[110] J.-P. Berenger, "A perfectly matched layer for the absorption of electromagnetic waves," *Journal of computational physics,* vol. 114, no. 2, pp. 185-200, 1994.

[111] luxpop. http://luxpop.com/RefractiveIndexList.html (accessed Jan 2020).

[112] I. Utke, S. Moshkalev, and P. Russell, *Nanofabrication using focused ion and electron beams: principles and applications*. Oxford University Press, 2012.

[113] J. R. Pugh, "Enhancing the performance of mid-infrared lasers using nanophotonic techniques," 2010.

[114] S. Y. Chou, P. R. Krauss, and P. J. Renstrom, "Imprint of sub-25 nm vias and trenches in polymers," *Applied physics letters,* vol. 67, no. 21, pp. 3114-3116, 1995.

[115] N. Kooy, K. Mohamed, L. T. Pin, and O. S. Guan, "A review of roll-to-roll nanoimprint lithography," *Nanoscale research letters,* vol. 9, no. 1, p. 320, 2014.

[116] H. H. Solak, C. Dais, and F. Clube, "Displacement Talbot lithography: a new method for high-resolution patterning of large areas," *Optics express,* vol. 19, no. 11, pp. 10686-10691, 2011.

[117] T. H. Maiman, "Stimulated optical radiation in ruby," *nature,* vol. 187, no. 4736, pp. 493-494, 1960.

[118] W. M. Steen and J. Mazumder, *Laser material processing*. springer science & business media, 2010.

[119] U. Klotzbach, A. F. Lasagni, M. Panzner, and V. Franke, "Laser micromachining," in *Fabrication and Characterization in the Micro-Nano*

Range: Springer, 2011, pp. 29-46.

[120] M. R. Lalakiya, "Micromachining process–current situation and challenges," 2015, vol. 34: EDP Sciences, p. 02006.

[121] B. Keiper, H. Exner, U. Loschner, and T. Kuntze, "Drilling of glass by excimer laser mask projection technique," *Journal of laser applications,* vol. 12, no. 5, pp. 189-193, 2000.

[122] J. M. Palmer and B. G. Grant, "The art of radiometry," 2009: SPIE.

[123] H. Dominguez-Andrade, A. Croot, G. Wan, J. A. Smith, and N. A. Fox, "Characterisation of thermionic emission current with a laser-heated system," *Review of Scientific Instruments,* vol. 90, no. 4, p. 045110, 2019.

[124] R. W. Powell, C. Y. Ho, and P. E. Liley, *Thermal conductivity of selected materials*. US Department of Commerce, National Bureau of Standards Washington, DC, 1966.

[125] P. Blanc *et al.*, "Direct normal irradiance related definitions and applications: The circumsolar issue," *Solar Energy,* vol. 110, pp. 561-577, 2014.

[126] S. I. Data and C. O. Power, "ORIEL PRODUCT TRAINING."

[127] J.-H. Lee, I. Bargatin, N. A. Melosh, and R. T. Howe, "Optimal emitter-collector gap for thermionic energy converters," *Applied Physics Letters,* vol. 100, no. 17, p. 173904, 2012.

[128] K. A. Littau *et al.*, "Microbead-separated thermionic energy converter with enhanced emission current," *Physical Chemistry Chemical Physics,* vol. 15, no. 34, pp. 14442-14446, 2013.

9. Appendix

9.1. Power output of the solar simulator

The solar simulator we have been using are Newport 67005 Light Source operating the model 6255 150W xenon lamp. To find out the output at certain wavelength range from the solar simulator, we use the spectral irradiance of Newport 6255 Arc lamp as shown in Figure 9.1.

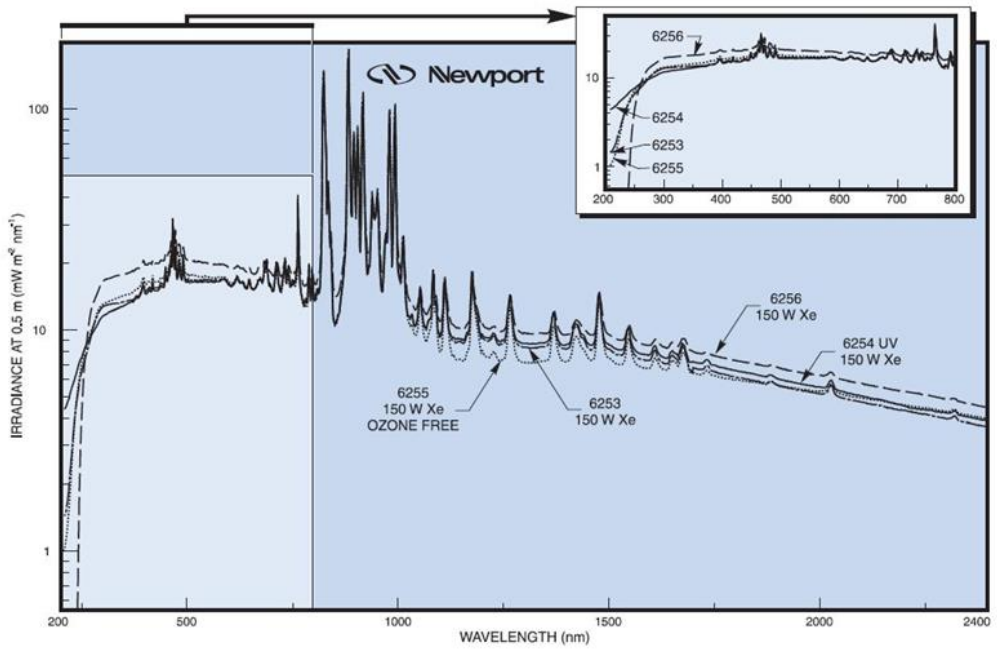

Figure 9.1 Spectral irradiance of Newport 6255 Arc Lamp

Due to the higher absorptivity of the molybdenum samples in the 500-900 nm range, we divided the power output into 3 wavelength ranges: 200-500 nm, 500-900 nm, 900-

2400 nm. Here is an example of how to calculate the output from 200-500 nm:

1. From the curve of lamp 6255 in Figure 9.1, the irradiance over 200-500 nm is approximately 15 $mW \cdot m^{-2} \cdot nm^{-1}$. The range is 300 nm, so the total irradiance is 300 $\times 15 = 4500\ mW \cdot m^{-2}$.

2. The conversion factor for the efficient Aspherab is 0.11 for the 67005 light source, therefore the total output over 200-500 nm is $4500 \times 0.11 = 495$ mW.

3. The lamp housing includes a rear reflector which increase the output by 60%, so the final output is $495 \times 1.6 = 792$ mW.

9.2. Calculating natural convection coefficient

In chapter 2.4, we introduced the correlations to estimate the convective heat transfer coefficient in different cases. Here is an example of estimating the convective heat transfer coefficient for a vertical plane in air. The equations are:

$$Nu = \frac{hL}{k}$$

$$Ra = Gr\ Pr$$

$$Gr = \frac{\rho L^3 g\beta(T_o - T_f)}{\mu^2}$$

$$Pr = \frac{c_p \mu}{k}$$

$$Nu = 0.68 + \frac{0.67Ra^{1/6}}{\left(1+(0.492/\mathrm{Pr})^{9/16}\right)^{4/9}}$$

The sample is an 1cm × 1cm square and it was placed vertically. If the sample temperature is T_o=150℃=423.15 K and the air temperature is T_o=20℃=293.15 K So, we have its characteristic length L=0.01 m, the density of air ρ=1.1 kg/m^3, the gravitational acceleration g =9.81, the thermal expansion coefficient $\beta = \frac{1}{\frac{T_o+T_f}{2}}$ =0.0028 K^{-1}, the fluid viscosity of air μ=1.87×10^{-5} N·s/m^2, the specific heat of air c_p = 1 J/g·K, the thermal conductivity of air k=0.027 W/(m·K). Then we can have Gr=7843, Pr=0.7, Ra=5438, Nu=5.08. Finally, we have the convective heat transfer coefficient for the vertical plane h=15.5 W/(m^2·K).